

Novel Probe Structures for High-Speed Atomic Force Microscopy

A Thesis
Presented to
The Academic Faculty

by

Rameen Hadizadeh

In Partial Fulfillment
of the Requirements for the Degree
Master of Science Mechanical Engineering in the
School of Mechanical Engineering

Georgia Institute of Technology
August 2009

NOVEL PROBE STRUCTURES FOR HIGH-SPEED ATOMIC FORCE
MICROSCOPY

Approved by:

Dr. Levent Degertekin, Advisor
School of Mechanical Engineering
Georgia Institute of Technology

Dr. Michael Leamy
School of Mechanical Engineering
Georgia Institute of Technology

Dr. Todd Sulchek
School of Mechanical Engineering
Georgia Institute of Technology

Date Approved: August 19th, 2009

For Mom, Dad, Sara and Ziggy

ACKNOWLEDGEMENTS

I would like to acknowledge the relentless effort put forth by the many individuals who contributed to this work. First and foremost I would like to thank my advisor Dr. Levent Degertekin for providing me with this invaluable experience. I would also like to thank the research group for their selfless assistance in my progression. In particular I would like to acknowledge Guclu Onaran, Zehra Parlak and Dr. Kianoush Naeli for their stimulating training and advice, Hamdi Torun and Baris Bicen for their assistance with various technical aspects, Jaime Zahorian, Dr. Krishna Sarangapani, and Michael Hochman for their advice in microfabrication and Yalcin Yamaner for his ANSYS expertise. I also wish to thank Dr. Aldo Ferri and Dr. Michael Leamy for their guidance.

TABLE OF CONTENTS

	Page
ACKNOWLEDGEMENTS.....	iv
LIST OF TABLES.....	viii
LIST OF FIGURES.....	ix
LIST OF SYMBOLS.....	xiv
LIST OF ABBREVIATIONS.....	xvii
SUMMARY.....	xix
 CHAPTER 1: BACKGROUND AND INTRODUCTION	
1 High-Speed AFM Imaging.....	1
1.1 Mechanics.....	2
1.2 Imaging Modes.....	4
1.3 Imaging Speed.....	5
1.4 Actuation Mechanisms.....	6
1.4.1 Piezoelectric Thin-Films.....	7
1.4.2 Photothermal.....	9
1.4.3 Magnetic.....	11
1.5 Current FIRAT Devices for Fast-Imaging.....	13
 CHAPTER 2: DESIGN REQUIREMENTS FOR THE IMPROVED FIRAT DEVICE	
2.1 Dual Cantilever Device.....	20
2.2 Seesaw Lever Device.....	23
2.3 Sensor Structures.....	26
2.4 Metrics.....	27
 CHAPTER 3: THEORETICAL AND COMPUTATIONAL MODELING	

3.1	Preliminary Design.....	35
3.2	ANSYS Finite Element Analysis.....	41
3.2.1	Background and Motivation.....	41
3.2.2	Force / Static Analysis.....	42
3.2.3	Modal Analysis.....	53
3.2.4	Viscous Damping Analysis.....	57
3.2.5	Transfer Function.....	67
3.2.6	Thermal-Mechanical Noise.....	74
3.2.7	Electrostatic Analysis.....	76
3.3	Cantilever Pull-In Voltage Analysis.....	82
3.3.1	Theory.....	82
3.3.2	Lumped Parameter Model.....	84
3.3.3	Linearized Uniform Approximate Model.....	86

CHAPTER 4: COUPLED SYSTEM ANALYSES

4.1	ANSYS Harmonic Analysis.....	89
4.1.1	Cantilever-on-Cantilever.....	89
4.1.2	Cantilever-on-Seesaw Lever.....	94
4.1.3	Bridge-on-Cantilever.....	98
4.2	Component Mode Synthesis.....	103
4.2.1	Euler-Bernoulli Analysis.....	105
4.2.2	Rigid Body and Constraint Modes.....	107
4.2.3	Assemblage of Modes.....	108
4.2.4	Energy Contributions.....	109
4.2.5	Component Mode Synthesis.....	110
4.2.6	Elimination of Redundant Modal Coordinates.....	111

4.2.7	The Eigenvalue Problem.....	112
4.2.8	Mode Shapes.....	113
4.2.9	Validation.....	115
4.2.10	Discussion.....	120
CHAPTER 5: DEVICE FABRICATION		
5	Process Flow.....	124
5.1	Isolation Layer on Silicon Substrate.....	129
5.2	Lift-Off Patterning of First electrode.....	130
5.3	First Sacrificial Layer.....	131
5.4	Second Electrode / Diffraction Grating.....	133
5.5	Silicon Nitride Actuator.....	136
5.6	Second Sacrificial Layer.....	138
5.7	Silicon Nitride Sensor and Third Electrode Patterning.....	141
5.8	KOH Backside Etching.....	145
5.9	Release of Device.....	147
CHAPTER 6: CONCLUSIONS AND FUTURE WORK		150
APPENDIX A: FABRICATION RECIPES		152
APPENDIX B: ANSYS AND MATLAB CODES		155
REFERENCES		182

LIST OF TABLES

	Page
Table 2.1: Desired System Characteristics.....	33
Table 3.1: Actuator Cantilever Dimensions.....	38
Table 3.2: Sensor Cantilever Dimensions.....	40
Table 3.3: Effective Spring Constants of End-Loaded Cantilever Beams.....	45
Table 3.4: Effective Spring Constants of Uniformly-Loaded Cantilever Beams.....	48
Table 3.5: Bridge Sensor Stiffness Characteristics.....	50
Table 3.6: Seesaw Lever Actuators and Respective Spring Constants.....	53
Table 3.7: Fundamental Resonance Frequencies (ANSYS).....	54
Table 3.8: Undamped Characteristics of Fixed-Free Cantilever Beams.....	55
Table 3.9: Undamped Fundamental Resonance Frequencies of Bridge Sensors.....	56
Table 3.10: Fundamental Resonance Frequencies of the Seesaw Lever Actuators.....	57
Table 3.11: Effective Physical Characteristics.....	60
Table 3.12: Cantilever Air-Damped Frequency Response Characteristics.....	70
Table 3.13: Bridge Air-Damped Frequency Response Characteristics.....	72
Table 3.14: Seesaw Lever Frequency Response Characteristics.....	73
Table 3.15: Effective Spring Constant for Electrostatic Loading.....	78
Table 3.16: Electrostatic Deflection from 200 Volts, DC (Closed-Form).....	78
Table 3.17: ANSYS Free-End Electrostatic Displacement from 200 V.....	81
Table 3.18: Electrostatic Deflection of Seesaw Lever Actuators from 100V, DC.....	82
Table 4.1: CMS Modal frequencies.....	113
Table 4.2: ANSYS Modal Frequencies.....	117
Table 4.3: CMS, ANSYS Modal Frequency Convergence.....	118
Table 4.4: Summary of Cantilevers.....	121
Table 4.5: ANSYS vs. CMS for Actual Devices.....	122

LIST OF FIGURES

	Page
Figure 1.1: Schematic of Conventional AFM.....	2
Figure 1.2: Tip-Sample Interaction Schematic.....	3
Figure 1.3: Oscillation Amplitude Variation in Tapping Mode.....	6
Figure 1.4: Micro-Cantilever Deflection Controlled by ZnO Thin-Film [4].....	8
Figure 1.5: Frequency Response of Thin-Film ZnO [8].....	9
Figure 1.6: Photothermal Actuation of Micro-Cantilever.....	10
Figure 1.7: Illustration of the Lorentz Force [16].....	12
Figure 1.8: Magnetically Actuated AFM Probe (Asylum Research).....	12
Figure 1.9: Schematic of the FIRAT AFM Probe [11].....	14
Figure 1.10: Intensity Fluctuations in HeNe Laser Diffracted Orders.....	15
Figure 1.11: SEM Image of a First-Generation FIRAT Membrane [11].....	16
Figure 1.12: SEM Image of Second-Generation FIRAT Bridge [18].....	16
Figure 1.13: Frequency Response of a First-Generation FIRAT Membrane.....	17
Figure 1.14: Frequency Response of Second-Generation FIRAT Devices.....	18
Figure 2.1: Schematic of the Dual Cantilever AFM Probe.....	20
Figure 2.2: Schematic of Electrostatic Actuation.....	21
Figure 2.3: Illustration of Silicon Nitride Dual Cantilever (sans tip).....	22
Figure 2.4: Backside Release of a Dual Cantilever Device.....	23
Figure 2.5: The Seesaw Lever Device.....	24
Figure 2.6: Backside Release of a Seesaw Lever Device.....	25
Figure 2.7: Variations of the Seesaw Lever Structure.....	25
Figure 2.8: Two Types of Sensor Structures.....	26
Figure 2.9: Frequency Response of Accelerometer [19].....	27
Figure 2.10: Top – FIRAT Fast Electrostatic Actuation. Bottom – Commercial z-Piezo.....	29
Figure 2.11: Bowed Bi-Layer Cantilever Structures [22].....	32
Figure 2.12: Box Schematic Representation of Coupled System.....	33

Figure 3.1: Cantilever Width and Thickness Versus Length for $f_0 = 550$ kHz, $k = 150$ N/m.....	37
Figure 3.2: Cantilever Width and Thickness Versus Length for $f_0 = 400$ kHz, $k = 130$ N/m.....	38
Figure 3.3: Cantilever width and Thickness Versus Length for $f_0 = 750$ kHz, $k = 30$ N/m.....	40
Figure 3.4: Cantilever Beam Subject to Different Loading Schemes [26].....	43
Figure 3.5: Nodal Displacement Contour Plot for an End-Loaded Beam.....	44
Figure 3.6: Comparison of Effective Spring Constant Calculation Methods.....	45
Figure 3.7: Method Comparison Using Closed-Form Solution.....	46
Figure 3.8: Nodal Displacement Contour Plot for Uniformly-Loaded Beam.....	47
Figure 3.9: Method Comparison Using Closed-Form Solution.....	49
Figure 3.10: Bridge Sensor Contour Plot of Displacement.....	50
Figure 3.11: FEM of Seesaw Lever Subject to Static Point Load.....	51
Figure 3.12: Seesaw Lever Displacement Contour Plot.....	52
Figure 3.13: Schematic of Electrodes and Air Gap.....	58
Figure 3.14: Spring-Mass-Damper Equivalent Circuit.....	58
Figure 3.15: Collapsed Equivalent Circuit.....	59
Figure 3.16: Pressure Contour Plot for Cantilever at 12 kHz Oscillation.....	62
Figure 3.17: Pressure Contour Plot for Bridge Structure at One Megahertz.....	64
Figure 3.18: FEA Pressure Contour of the Original Seesaw Lever Design.....	65
Figure 3.19: FEA Pressure Contour for Seesaw Lever Variation 1.....	66
Figure 3.20: FEA Pressure Contour for Seesaw Lever Variation 2.....	66
Figure 3.21: Transfer Function (Magnitude and Phase) of a Sensor Cantilever.....	67
Figure 3.22: Transfer Function (Magnitude and Phase) of an Actuator Cantilever.....	68
Figure 3.23: Transfer Function (Magnitude and Phase) of a Bridge Sensor.....	71
Figure 3.24: Seesaw Lever Transfer Function.....	73
Figure 3.25: Thermal Mechanical Noise: Force (top) and Displacement (bottom).....	75
Figure 3.26: Impinging HeNe Laser Schematic.....	77
Figure 3.27: ANSYS Electrostatic Displacement.....	80
Figure 3.28: Lumped Pull-In Model [33].....	83
Figure 3.29: Pull-In Voltage for Lumped Parameter Model.....	85

Figure 3.30: (a) Micro-Cantilever at Rest and (b) Collapsed Micro-Cantilever.....	86
Figure 3.31: Comparison of Pull-In Voltage Estimation Methods.....	87
Figure 4.1: Cantilever-on-Cantilever FEA Model.....	90
Figure 4.2: Actuator and Sensor Node Paths.....	91
Figure 4.3: Frequency Response along Cantilever Sensor Node Path.....	92
Figure 4.4: Frequency Response along Cantilever Actuator Node Path.....	92
Figure 4.5: Relative Displacement of Sensor and Actuator.....	93
Figure 4.6: Modal Displacements, Left) 372 kHz and Right) 682 kHz.....	94
Figure 4.7: Cantilever-on-Seesaw Lever FEA Model.....	95
Figure 4.8: Frequency Response along Seesaw Lever Actuator Node Path.....	96
Figure 4.9: Frequency Response along Cantilever Sensor Node Path.....	96
Figure 4.10: Relative Displacement of Sensor and Actuator At System Resonance Modes.....	97
Figure 4.11: Modal Displacements, Top Left) ~ 220 kHz, Top Right) ~ 390 kHz, and Bottom) ~750 kHz.....	98
Figure 4.12: Bridge-on-Cantilever FEA Model.....	99
Figure 4.13: Sensor and Actuator Node Paths.....	100
Figure 4.14: Frequency Response along Bridge Sensor Node Path.....	101
Figure 4.15: Frequency Response along Cantilever Actuator Node Path.....	101
Figure 4.16: Bridge-on-Cantilever Relative Displacement.....	102
Figure 4.17: Modal Displacements, Left) ~405 kHz and Right) ~ 1.17 MHz.....	103
Figure 4.18: Dual Cantilever Schematic.....	104
Figure 4.19: Schematic of Fixed-Free Cantilever.....	105
Figure 4.20: CMS System Schematic.....	111
Figure 4.21: First Five System Mode Shapes; the Red Curve Indicates the Smaller Cantilever.....	115
Figure 4.22: FEM of a Dual Cantilever System.....	116
Figure 4.23: Percent Error in CMS Convergence.....	118
Figure 4.24: ANSYS Mode Convergence.....	119
Figure 4.25: CMS Mode Convergence.....	120
Figure 4.26: Percent Error Plot of CMS Relative to ANSYS Results.....	123
Figure 5.1: Thermally Oxidized Wafer.....	124

Figure 5.2: First Electrode.....	125
Figure 5.3: First Sacrificial Layer.....	125
Figure 5.4: Second Electrode / Diffraction Grating.....	125
Figure 5.5: First Cantilever.....	126
Figure 5.6: Second Sacrificial Layer.....	126
Figure 5.7: Third Electrode Deposition.....	126
Figure 5.8: Second Cantilever.....	127
Figure 5.9: Third Electrode Patterning	127
Figure 5.10: Backside Etch Mask	127
Figure 5.11: KOH Backside Etch.....	128
Figure 5.12: BOE Etch of Remaining Oxide.....	128
Figure 5.13: Released Dual Cantilever Device.....	128
Figure 5.14: Schematic of First Electrode.....	130
Figure 5.15: Successful Lift-Off Patterning of First Electrode.....	130
Figure 5.16: Schematic of First Sacrificial Layer.....	131
Figure 5.17: Top left) Al Sacrificial Layer, Etched with Al Type-A Etchant at 50°C. Top Right) Al Sacrificial Layer, Etched with Al Type-A Etchant at Room Temperature. Bottom Left) SiO ₂ Sacrificial Layer Etched by Reactive Ion Etch (RIE). Bottom Right) Amorphous Silicon Sacrificial Layer Etched with Inductively Coupled Plasma (ICP) Using the Bosch Process [40].....	132
Figure 5.18: Schematic of Second Electrode / Diffraction Grating.....	133
Figure 5.19: Deep Undercut of Cr Diffraction Grating.....	134
Figure 5.20: Intact Wet-Etched Cr Diffraction Grating.....	134
Figure 5.21: Scanning Electron Micrograph of HF-Damaged Nitride Cantilever-on-Seesaw Lever Device.....	135
Figure 5.22: Schematic of First Silicon Nitride Cantilever.....	136
Figure 5.23: First SiN _x Cantilever.....	137
Figure 5.24: Undercut of Nitride Cantilever Actuator.....	137
Figure 5.25: Schematic of Second Sacrificial Layer.....	138
Figure 5.26: Al Second Sacrificial Layer.....	139
Figure 5.27: Amorphous Silicon Second Sacrificial Layer.....	140
Figure 5.28: Schematic of Second Nitride Cantilever and Third Electrode.....	141

Figure 5.29: Bridge Sensor atop Seesaw Lever Actuator.....	141
Figure 5.30: SEM Image of Damaged Bridge Sensor.....	142
Figure 5.31: Bridge Sensor Etched with Al Masking Layer.....	143
Figure 5.32: Patterned Third Electrode.....	144
Figure 5.33: Ideal Electrode Step Coverage.....	145
Figure 5.34: KOH Backside-Etched Bridge-on-Cantilever Device.....	146
Figure 5.35: Scanning Electron Micrographs of Bridge-on-Cantilever Devices, Pre-Sacrificial Layer Release.....	148
Figure 5.36: Optical Micrograph of Released Bridge-on-Cantilever Device.....	149

LIST OF SYMBOLS

B		Magnetic Field Vector
I		Electrical Current Vector
ω_0		Fundamental Resonance Frequency (rad)
k		Spring Constant
k_{eff}		Effective Spring Constant
m		Mass
m_{eff}		Effective Mass
E		Elastic Modulus
W, b		Beam Width
H		Beam Thickness
L, l		Beam Length
ρ		Density
f_0		Fundamental Resonance Frequency (Hz)
α		Mass Correction Factor
j		Imaginary
ω		Angular Frequency (rad)
Z		Impedance
F		Force
K_n		Knudsen Number
λ		Mean Free Path
P		Pressure
d_0, g		Air Gap
v		Velocity
ϕ		Phase Angle
$H(\omega j)$		Transfer Function
τ_c		Time Constant
k_b		Boltzmann Constant

T	Temperature (K)
b	Damping
S_n	Thermal-Mechanical Noise
ϵ	Permittivity of Free Space
A	Surface Area
V	Voltage (DC)
x_{static}	Static Displacement
β	Normalized Maximum Deflection
\hat{E}	Adjusted Elastic Modulus
λ_r	% of Beam Subject to Electrostatic Loading

COMPONENT MODE SYNTHESIS

x	Axis of Transverse Displacement
t	Time
$w(x,t)$	Transverse Displacement
$I(x)$	Area Moment of Inertia
m	Mass per Unit Length
l	Beam Length
α_n	Eigenvalue
ω_n	Eigenfrequency
$\varphi_n(x)$	Eigenfunction (Mode)
Φ_1^T	Transpose Matrix of Modes
\mathbf{M}_c	Component Mass Matrix
\mathbf{K}_c	Component Stiffness Matrix
T_c	Component Kinetic Energy
V_c	Component Potential Energy
ξ	Matrix of Modal Coordinates
\mathbf{Z}_c	Forcing Matrix

I	Identity Matrix
q	Truncated Matrix of Modal Coordinates
ω_p	Modal Frequency

LIST OF ABBREVIATIONS

AFM	Atomic Force Microscope
FIRAT	Force-sensing Integrated Readout and Active Tip
SEM	Scanning Electron Microscope
PZT	Lead-Zirconate-Titanate
ZnO	Zinc Oxide
HeNe	Helium-Neon
Q	Quality
SNR	Signal-to-Noise Ration
Ti	Titanium
Cr	Chromium
Au	Gold
Al	Aluminum
Mo	Molybdenum
Si	Silicon
SiN _x	Silicon Nitride
SiO ₂	Silicon Oxide
dB	Decibel
FEA	Finite Element Analysis
FEM	Finite Element Model
PECVD	Plasma-Enhanced Chemical Vapor Deposition
RTP	Rapid Thermal Annealing
CMS	Component Mode Synthesis
T-M	Thermal-Mechanical
CMOS	Complimentary Metal Oxide Semiconductor
KOH	Potassium Hydroxide
ICP	Inductively Coupled Plasma
RIE	Reactive Ion Etch
HF	Hydrofluoric Acid

SF ₆ /O ₂	Sulfur Hexafluoride / Oxygen
PR	Photoresist
aSi	Amorphous Silicon
Cl	Chlorine
LPCVD	Low-Pressure Chemical Vapor Deposition
BOE	Buffered Oxide Etch
IPA	Isopropyl Alcohol

SUMMARY

Atomic Force Microscopy (AFM) has become an indispensable metrology tool for nanoscale surface characterization. Today, research and industry demand faster and more accurate metrology and these demands must be met expediently. Traditional AFM cantilevers and associated actuators (i.e. piezoelectric) are limited in regards to actuation speed and resonance frequency presenting the user with an undesired trade-off of speed versus resolution. Based on a pre-existing technology known as the FIRAT (Force Sensing Integrated Readout and Active Tip) AFM probe, this work aims to remedy actuation and response issues by implementing a cantilever-on-cantilever probe as well as a novel seesaw probe [1]. Electrostatic actuation is present in both cases, eliminating the need for piezoelectrics while demonstrating large - micron scale - actuation and sensitive displacement detection. These new probe designs can potentially demonstrate a wide bandwidth frequency response (e.g. 100 kHz) ideal for high-speed video-rate imaging. Unlike traditional AFM cantilevers, this is realized by mechanically coupling two physically separate structures to provide a soft resonator sensor atop a stiff actuator structure. Common surface-micromachining techniques are utilized to solve the logistical challenge of fabricating these stacked structures. By manipulating the viscous damping and mechanical mode coupling it becomes feasible to attain the aforementioned desired dynamic characteristics.

CHAPTER 1:

BACKGROUND AND INTRODUCTION

1 High-Speed AFM Imaging

Exciting progress and advancement has swept the field of atomic force microscopy (AFM) during its two-decade adolescence. First conceived in 1986 by Dr. Gerd Binnig and Dr. Calvin Quate [1], the AFM has proven to be an invaluable metrology tool for a broad range of sciences and engineering. Perhaps the most sought-after improvement of current AFM systems lies in the speed and resolution at which images can be acquired. The inception of various actuation methods and fast-feedback circuitry has allowed researchers to push the limitations of AFM to the point where biological processes can now be observed in real time with minimal damage to the molecules [2]. Advancements have enabled the capture of an image series on the order of milliseconds while retaining the same force resolution as an image series that may have taken 15 minutes to acquire with a traditional AFM system [3]. AFM has accrued a substantial foundation on which the technology can swiftly progress and compete with leading scanning-probe metrology such as the scanning electron microscope (SEM) and various other contact / non-contact profilometry. With Angstrom-scale lateral resolution and piconewton-scale force resolution the AFM has become the inevitable first choice for academia and industry, and continues to rapidly improve [4].

1.1 Mechanics

At the heart of a conventional AFM system is the micro-cantilever which is used as a direct liaison to the sample via the sharp tip mounted at its free end. The most common deflection detection scheme is known as the beam-bounce method in which a laser spot is reflected from the backside of the cantilever and directed towards a stationary bi-cell photodiode. Figure 1.1 is a schematic of the fundamental components found in an AFM [5].

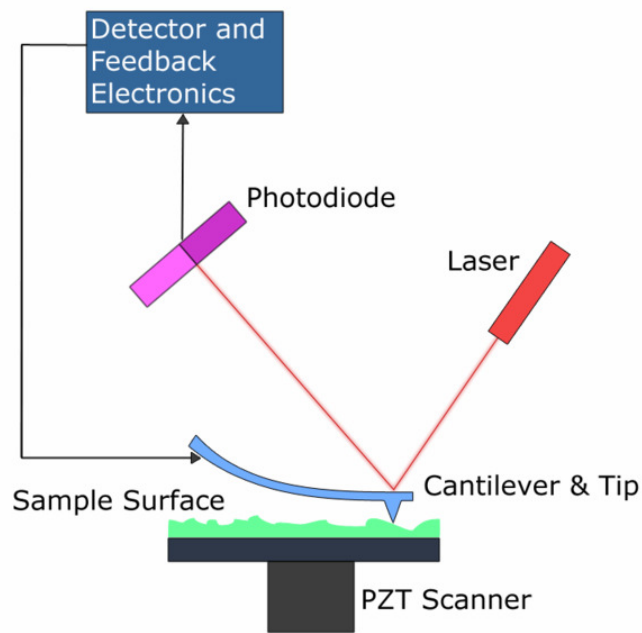


Figure 1.1: Schematic of Conventional AFM

Also shown in Figure 1.1 is a PZT scanner (short for Lead-Zirconate-Titanate), or a piezo-electric scanner. The function of the PZT scanner is to move the sample in the x, y, and z coordinate directions such that the micro-cantilever can contact the entire surface. The scanner does so by means of the piezo-electric effect, a phenomenon that causes

materials to strain when subject to an electric field. Since the strain occurs in a specified direction (relative to the direction of the electric field), it is possible to situate the PZT (or several PZT elements in series) beneath the sample such that the strain translates the sample stage. An alternative to mounting the piezo scanner beneath the sample is to mount a piezo “stack” directly on the substrate which holds the micro-cantilever. One method has very little advantage over the other (since all motion is considered relative) and is usually the preference of the manufacturer. Figure 1.2 depicts in greater detail the tip-sample interaction; the term “atomic force” originates from the concept that single atoms interact at the tip-sample interface [6].

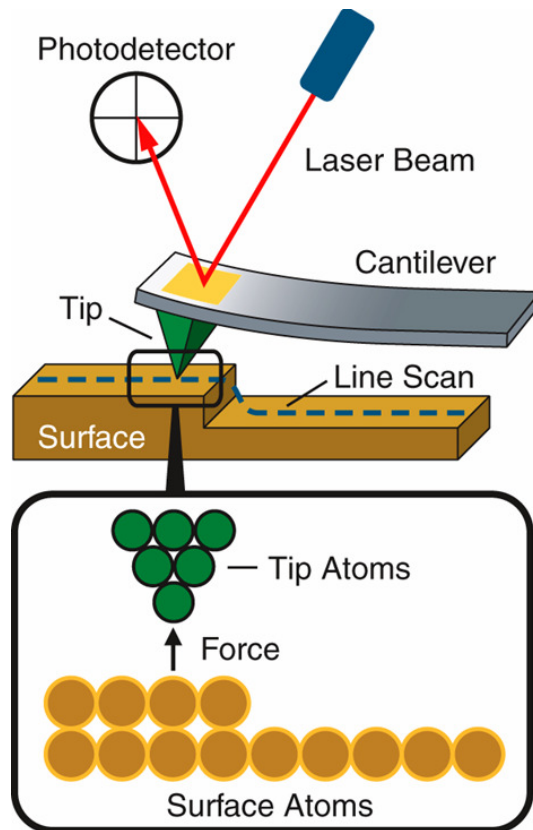


Figure 1.2: Tip-sample Interaction Schematic

As an aside, Figure 1.2 stresses the importance of having an AFM probe with a tip-sharpness on the order of nanometers.

1.2 Imaging modes

There are mainly two types of contact AFM imaging modes: constant-contact mode and intermittent (tapping) mode. The imaging mode is generally chosen at the operator's discretion; however each mode has its advantages in certain situations. Constant contact mode (hereafter referred to as contact mode) operates based on a force set-point thus the cantilever drags along the surface while the feedback circuitry attempts to keep the tip-sample interaction force at a constant value. The resulting deflection of the laser onto the photodiode produces the topographical information from the scan. Intermittent mode (hereafter referred to as tapping mode) operates on an amplitude set-point method in which the amplitude of oscillation of the cantilever is kept at a constant value during imaging. In the latter case the micro-cantilever is actively oscillating at or near its resonance frequency whereas contact mode utilizes a passive micro-cantilever. As the cantilever taps the surface, each tap contributes to a pixel in the final image. Intuitively it should take longer to acquire topographical information in tapping mode since the micro-cantilever is not always in contact with the sample. Imaging time is where contact mode thrives, however it is not conducive to high force-resolution [7]. Contact mode also creates a significant lateral force on the sharp-tip, causing damage to both the probe and a soft sample over time. Tapping mode introduces a significant amount of complications in analysis due to the contribution of attractive and repulsive forces (i.e. capillary forces, van der Waals forces); however these complications can

unlock interesting information regarding sample material properties. Ultimately, as previously mentioned, it is at the operator's discretion to decide which mode to use based on the characteristics of the sample and the desired imaging resolution.

1.3 Imaging Speed

Since micro-cantilevers can potentially exhibit broadband frequency responses (tens of kilohertz) and high resonance frequencies (hundreds of kilohertz), it is desired to employ tapping mode when pursuing a fast-imaging setup. High speed imaging can be conducted using contact mode AFM, but this contributes to substantial tip and sample wear. Micro-cantilever bandwidth and resonance frequency are a minor consideration when imaging in contact-mode, therefore the dynamics of the device does not usually contribute to a faster setup. Unfortunately, even if the micro-cantilever is flawless in every respect, it is the peripherals of the AFM system (i.e. the piezo scanner and feedback circuitry) that limit the speed at which a user can scan a sample. A micro-cantilever can tap at very high frequencies but this advantage is lost when the line scan rate is limited to 10 or 20 Hz due to the bandwidth of commercial piezo actuators [8]. Line scan rate refers to the time it takes the micro-cantilever to scan from one end of the sample to the other and then back to its origin (on the same axis, see Figure 1.2); thus a line scan rate of 10 Hz suggests the micro-cantilever can go forth and back 10 times in one second. The direction in which the line scan is executed is known as the 'fast-scan' axis. The 'slow-scan' axis refers to the axis perpendicular to the fast-scan axis; the sample stage is translated slowly in the slow-scan axis in order to produce a two-dimensional image.

Figure 1.3 illustrates the concept of tapping mode in regards to vertical-step topography [8].

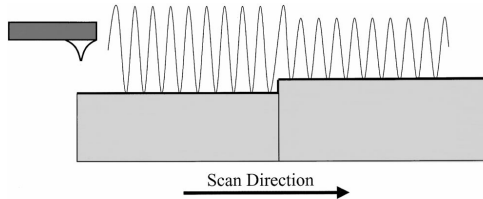


Figure 1.3: Oscillation Amplitude Variation in Tapping Mode

As the cantilever approaches and passes over the vertical step, it is the responsibility of the z-scan piezo to regulate the oscillation amplitude such that it remains at the set-point. At slow line scans (i.e. 1 or 2 Hz) a vertical step presents virtually no problems in imaging. However, when the line scan is increased, the limited bandwidth of the z-scan piezo causes the amplitude to vary uncontrollably until it is once again stabilized at the set-point; this instability in set-point regulation can be seen as an artifact in the final image. The scan rate is thus limited to the single-Hertz range and conventional AFM imaging becomes very time-consuming.

1.4 Actuation Mechanisms

Numerous research groups have managed to expedite atomic force microscopy using novel z-actuation methods. Various energy means have been exploited including photothermal [9], magnetic [10], and electrostatic actuation [11]. In each case the z-actuation piezo is non-existent (replaced by the new energy means), alleviating the burden of a slow component in the feedback loop; the average commercial z-actuation

piezo has a bandwidth of one to two kilohertz [8]. However, fast-imaging methods have been presented that exploit thin-film piezoelectrics for on-cantilever control during imaging [4]. Generally the substantial increase in imaging speed accompanies complicated feedback circuitry and signal processing and often times an entirely custom bench-top AFM system must be constructed. Some AFM vendors (Asylum Research) offer system upgrades that utilize alternative actuation means, but they are intended for use in special environments (i.e. fluids) and are not meant for fast-imaging.

1.4.1 Piezoelectric Thin-Films

Although the fast-imaging community tends to steer clear of piezoelectrics due to their limited bandwidth, the idea of scaling down the piezoelectric to the size of the micro-cantilever means a higher resonance frequency and ultimately a greater imaging bandwidth. S. R. Manalis, et al. have presented a method in which a Zinc-Oxide (ZnO) piezoelectric thin-film is deposited at the base of the tapping-mode cantilever [4]. With the ZnO z-actuator integrated to the cantilever it is possible to rapidly correct for the bending in the cantilever caused by stepping over sample topography (Figure 1.4).

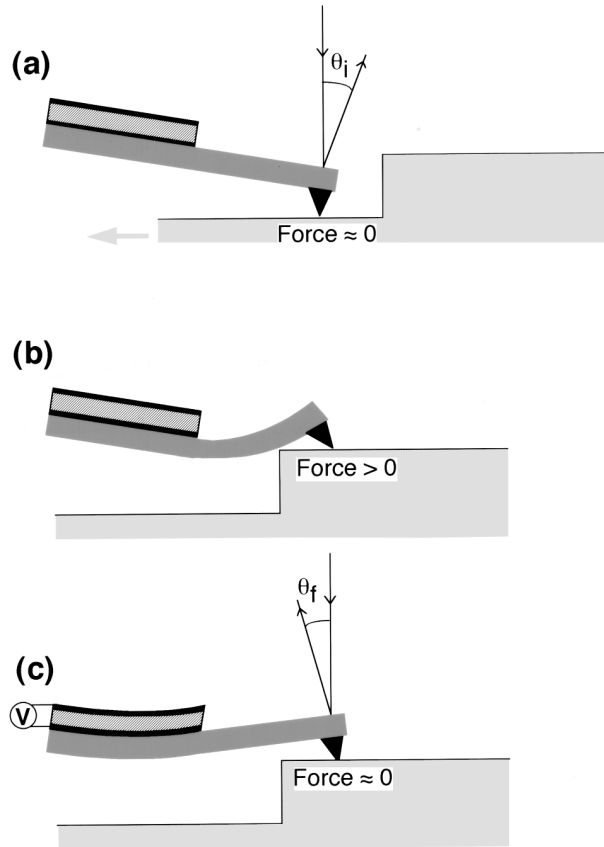


Figure 1.4: Micro-Cantilever Deflection Controlled by ZnO Thin-Film [4]

Not only does this method optimize the bandwidth of the actuator, it provides several microns of z-axis displacement such that large topographies can be scanned with minimal limitation on speed. However, when the sample topography exceeds one micron the laser spot deflects out of the bounds of the photodiode array. The significant gain from [4] is better illustrated when considering the frequency response of thin-film piezoelectrics as compared with commercial PZT actuators (Figure 1.5).

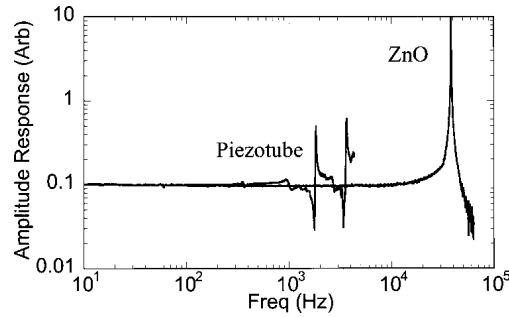


Figure 1.5: Frequency Response of Thin-Film ZnO [8]

As previously mentioned, the bandwidth of a commercial Piezotube is limited to the few kilohertz range while thin-film ZnO exhibits a flat response up to the tens of kilohertz range (bandwidth is detailed in a later section). It should also be noted that imaging in fluids (for biological applications) is not possible with thin-film ZnO unless an isolation layer is considered, which introduces significant complications. The bending moment caused by ZnO thin-films is most efficient when their thickness is at a minimum, but thin ZnO accompanies a very low breakdown voltage. For thicker ZnO films, the breakdown voltage is increased but this accompanies a loss in bending moment. Longer cantilevers can be used to increase both bending moment and breakdown voltage, but this in turn creates a slower probe. However with this method 512 scan lines were captured in less than 15 seconds for a scan size of 100 by 100 microns, which would take several minutes with a commercial AFM [4]. Successful parallel AFM operation has been demonstrated using ZnO thin-films [12].

1.4.2 Photothermal

A particularly clever yet complex approach to fast-imaging involves the photothermal actuation of the AFM micro-cantilever. Yamashita, et al. have succeeded

in manipulating the bending stress in a micro-cantilever using an intensity-modulated infrared laser [9]. The photothermal effect relies on the ability of a metal-coated (usually gold) cantilever to expand when exposed to the intensity of a laser spot; displacement is dictated according to laser light intensity modulation. The heat transmission to the cantilever is relatively slow, disabling the prospect of a fast-actuation scheme; however, an inverse transfer function compensation method has enabled a frequency response of the micro-cantilever with bandwidth up to 700 kHz [9]. Figure 1.6 illustrates the complex optics involved with the setup used in [9].

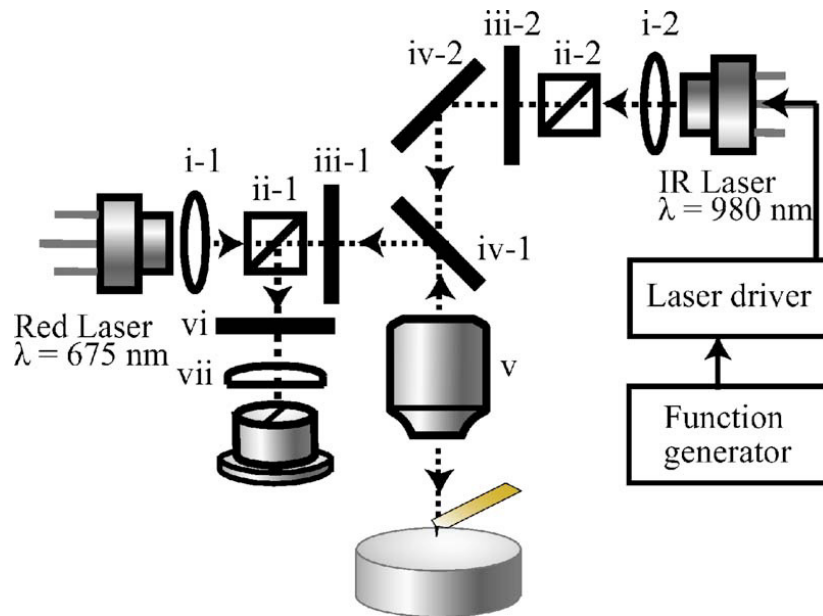


Figure 1.6: Photothermal Actuation of a Micro-Cantilever

Included in the complexity is the mathematics behind the feedback signal. Since inverse-transfer function compensation is only realized with an exact unity feedback gain, the delays in the electronic components become a difficult obstacle. By controlling the signal through multiple delay loop circuits the team was able to achieve an actuation

bandwidth equivalent to five times that of the original non-compensated photothermal excitation [9]. Several groups have succeeded in boosting imaging bandwidth simply by manipulating the mathematics and feedback circuitry in conventional AFM setups [13]. Nonetheless, photothermal actuation presents an impasse when considering in-fluid imaging as well as parallel operation because of the overly-complex optical setup.

1.4.3 Magnetic

Thus far a trend is noticeable in fast-imaging setups, namely the fact that the AFM cantilever is potentially the fastest component in the system. In the reviewed literature the goal has been to shrink the actuation scheme to the scale of the micro-cantilever such that speed and bandwidth can be substantially increased; various size-reduction techniques have proven successful ([14], Olympus). The theory of magnetism has long been used to actuate various sensors [15] and even Asylum Research produces an AFM probe that is magnetically actuated for the sake of in-fluid imaging. However, magnetic actuation is promising in regards to fast-imaging since it lacks the drawbacks of photothermal (slow heat transfer) and piezoelectric (limited bandwidth) actuation schemes. Actuation in a magnetic sense relies on a magnetic field (\mathbf{B} -field) as well as a directed electrical current; the two components couple to produce what is known as the Lorentz force. Figure 1.7 is a schematic of the Lorentz force as a cross-product of magnetic field, \mathbf{B} , and current, \mathbf{I} . The schematic also illustrates the right-hand rule, which is used to predict the direction of one of the three components if two are known.

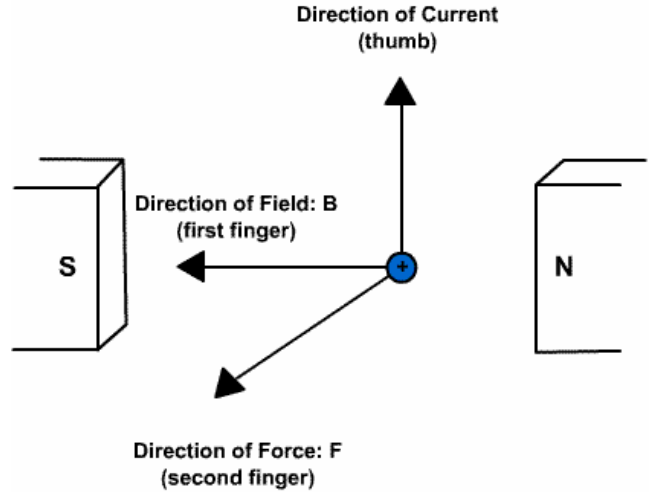


Figure 1.7: Illustration of the Lorentz Force [16]

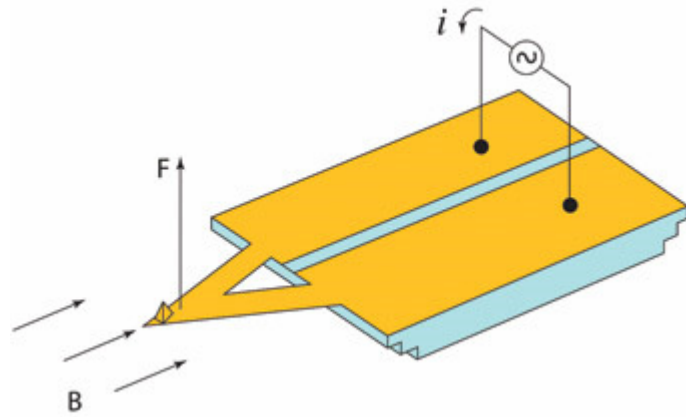


Figure 1.8: Magnetically Actuated AFM Probe (Asylum Research)

According to Figure 1.7 the micro-cantilever AFM probe can dually function as its own z-actuator; the only additional requirement is that there be current lines on the micro-cantilever and an existing B-field (Figure 1.8). In [10] a solenoid coil was used to generate a magnetic field while the micro-cantilever was modified with current lines; the cantilever was therefore manipulated by applying either a DC (large deflection) or AC (tapping frequency) current. Intuitively, the solenoid coil is the main restriction on

frequency response since the system exhibits low-pass filter characteristics where the inductance of the coil dictates the bandwidth [10]. This is however an advantage since the first-order characteristics of a solenoid are superior to that of the second-order response of a commercial z-piezo. Disadvantages for magnetic actuation include complex feedback circuitry and mathematics, but fortunately this method makes more efficient use of the micro-cantilever dynamics. Parallel operation may be a challenge with magnetic actuation since the devices can engage in significant cross-talk.

1.5 Current FIRAT Devices for Fast-Imaging

Presented in 2006, the force sensing integrated readout and active tip (FIRAT) probe functions by means of electrostatic actuation with an integrated interferometric displacement detection scheme [11]. The FIRAT probe primarily operates in tapping mode in order to reduce shear forces and can detect tapping forces on the order of piconewtons [11]. A schematic of the FIRAT probe is shown in Figure 1.9. The diffraction grating (which is stationary, attached to the transparent substrate) functions as one electrode while the micro-machined aluminum membrane functions as the second electrode; this architecture mimics a simple capacitor and thus the membrane can be deflected by applying a DC and / or AC voltage.

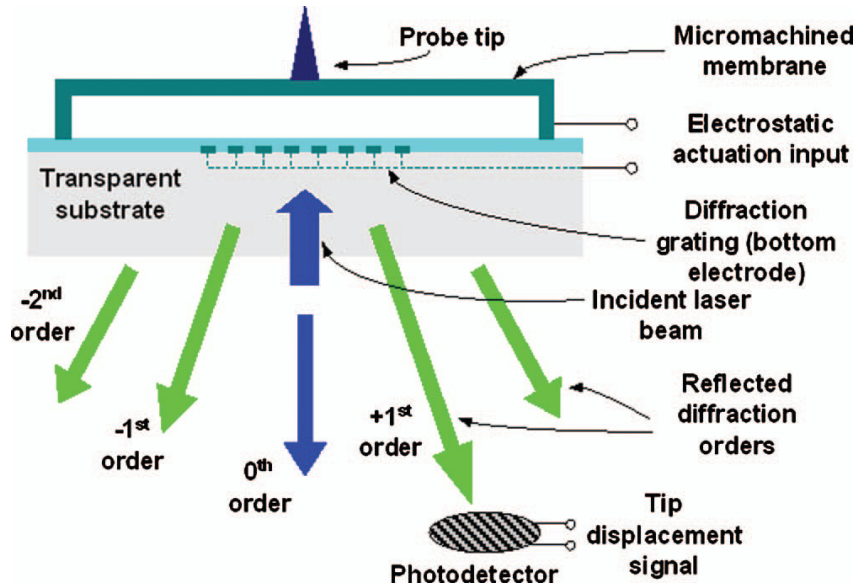


Figure 1.9: Schematic of the FIRAT AFM Probe [11]

Whereas the position of the deflected laser (onto the photodiode) is relevant to changing topography in traditional AFM, it is the modulation in intensity of the diffracted orders that is relevant when scanning topography with the FIRAT probe. Once again, z-piezo actuation has been replaced and thus a bandwidth burden has been alleviated. The FIRAT membranes presented in [11] have evolved into clamped-clamped beam structures [17], but the functionality of each structure is nearly identical. A Helium-Neon (HeNe) laser is used as the incident laser beam (pictured in Figure 1.9) and has a wavelength of approximately 633 nm, thus the air gap between the two electrodes has been optimized such that the intensity of the diffracted orders are at a maximum. However due to uncertainties in micro-fabrication, the air gap is adjustable using a large DC bias voltage in order to move the membrane to an optimal sensitivity point. According to Figure 1.10 the sensitivity of the detection scheme is linear (which is desired) only within certain bounds of the curve.

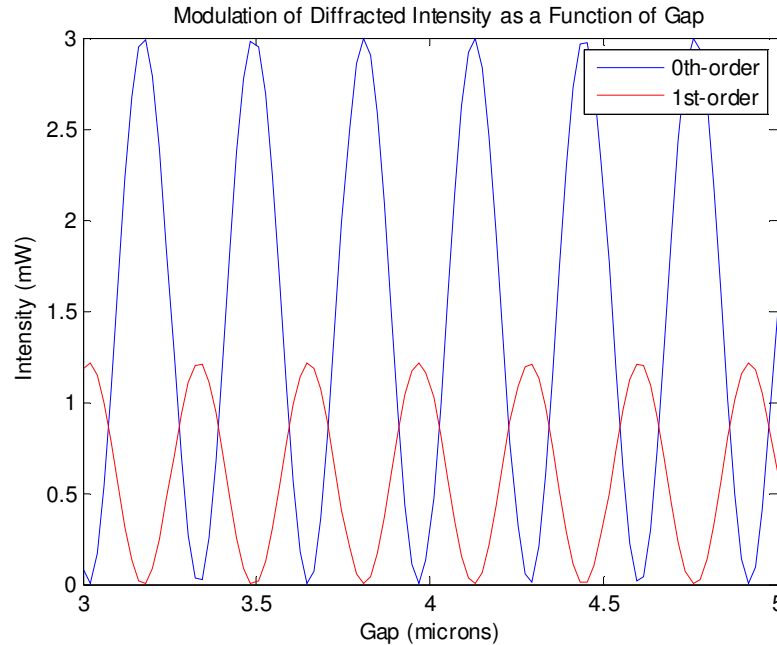


Figure 1.10: Intensity Fluctuations in HeNe Laser Diffracted Orders

For instance, if the photodiode is configured to capture the 1st diffraction order and the device has an air gap of 3.5 microns, the intensity seen by the photodiode would be nearly zero milliwatts. However, with a DC voltage input to the electrodes, the membrane could be biased to a position where the air gap is 3.3 – 3.4 microns and the intensity seen by the photodiode would increase significantly; the device would also be operating in the linear range of the sinusoid. Ultimately, the z-range of the sensor is limited to a quarter-wavelength of the impinging light, or approximately 160 nanometers. Intuitively, this compensation method greatly hinders the z-actuation displacement. Whereas a PZT z-actuator is capable of displacing the probe on the order of microns, the FIRAT probe is limited to only hundreds of nanometers. Thus relatively smooth topography is ideal for the current generation of FIRAT probes. Figure 1.11 is a scanning electron micrograph of a first-generation FIRAT device (membrane style).

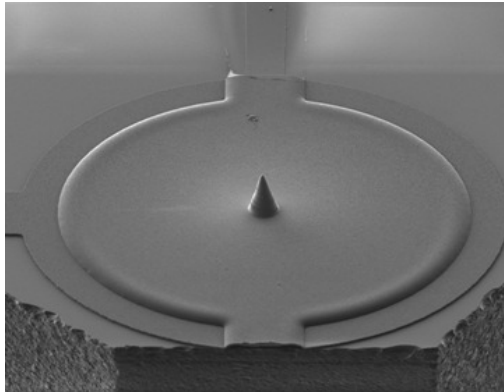


Figure 1.11: SEM Image of a First-Generation FIRAT Membrane [11]

In Figure 1.11 the diced substrate is visible; current FIRAT probes reside on quartz (fused silica) substrates which are transparent, allowing the incoming HeNe laser light to enter unobstructed. Although transparent, the quartz substrate does contribute to modulation loss since it is approximately 530 microns thick and light refraction inevitably occurs. It is not possible to remove the substrate from beneath the membrane since the diffraction grating requires that location. The second-generation FIRAT devices (clamped-clamped beam style) show improved dynamics due to the mitigation of viscous damping (Figure 1.12).

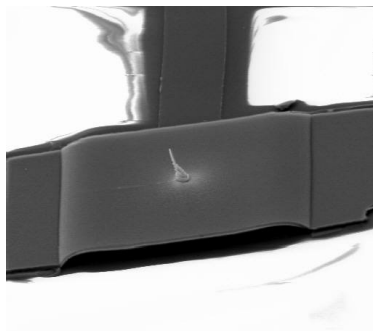


Figure 1.12: SEM Image of a Second-Generation FIRAT Bridge [18]

The large “vent-holes” to each side of the bridge allow more air to escape during high-frequency oscillation, reducing the stiffening and damping effects of trapped air. The frequency response of the first-generation FIRAT devices was quite limited, exhibiting a low-frequency cutoff in the single kilohertz range (Figure 1.13). The bandwidth seen in Figure 1.13 is comparable to that of a commercial PZT actuator, however this is mainly due to the geometry of the membrane and is not an impassable limitation.

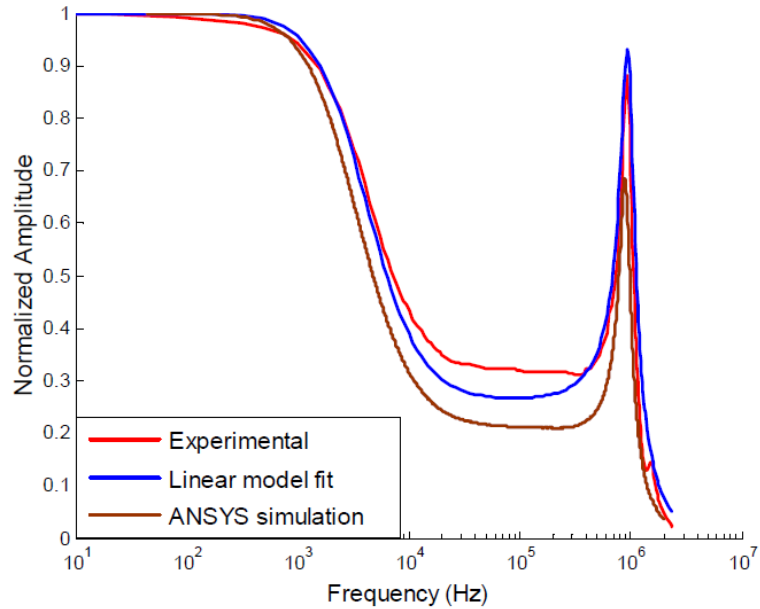


Figure 1.13: Frequency Response of a First-Generation FIRAT Membrane

The extreme attenuation is attributed to viscous damping, which also mitigates the quality factor of the device. In comparison, the frequency response of the second-generation bridge structures exhibits a wider bandwidth with high Q factor (Figure 1.14). According to the approximate 3 dB cutoff frequencies for Figures 1.13 and 1.14, the bandwidth for

the second-generation FIRAT devices is over 100 times that of the first-generation devices.

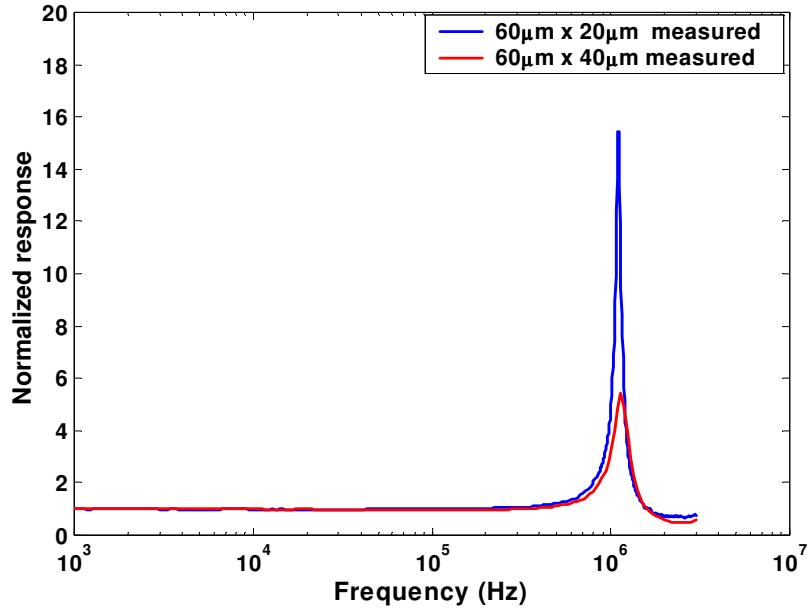


Figure 1.14: Frequency Response of Second-Generation FIRAT Devices

The FIRAT devices seen in Figure 1.14 demonstrate a flat response until device resonance which is ideal for a tapping-mode sensor. The particular bridges seen in Figure 1.14 have stiffness values between 50 and 100 N/m. Nonetheless, the detection range is highly restricted because of the device architecture which confines the use of these second generation devices to samples with less than 200 nm shifts in topography. The detection range has seen improvements in the form of phase sensitive diffraction gratings [17], but this method of improvement requires a complicated optical detection scheme.

In summary, the FIRAT probe exhibits qualities conducive to fast-imaging i.e. broadband response, low-noise integrated interferometric detection, and high force-resolution. Video-rate imaging has been demonstrated with the second-generation FIRAT probe; however the work remains to be published. The current generation of devices certainly has room for improvement; among these improvements is an extended actuation range (currently limited to less than 200 nanometers), a larger actuation bandwidth (currently limited to 50 or 60 kHz), and improved force resolution (piconewtons) with a high signal-to-noise ratio (SNR).

CHAPTER 2:

DESIGN REQUIREMENTS FOR THE IMPROVED FIRAT DEVICE

2.1 Dual Cantilever Device

There is an extensive design criterion that must be met in order to produce an AFM probe that will perform as well as its fast feedback circuitry. The major consideration lies in the area of high-bandwidth z-actuation; this is currently the most significant hindrance in high-speed AFM [9]. Similar to the aforementioned alternative z-actuation schemes, the dual cantilever device aims to rid the system of a slow piezoelectric z-actuator, thus increasing the overall imaging bandwidth. This novel device incorporates two cantilevers, mechanically coupled, each one serving as either an actuator or a tapping sensor. The tapping cantilever (hereafter referred to as the sensor) is relatively soft with a high resonance frequency and sits atop an actuation cantilever (hereafter referred to as the actuator) that is relatively stiff with a broadband frequency response. Figure 2.1 is a schematic of the proposed structure.

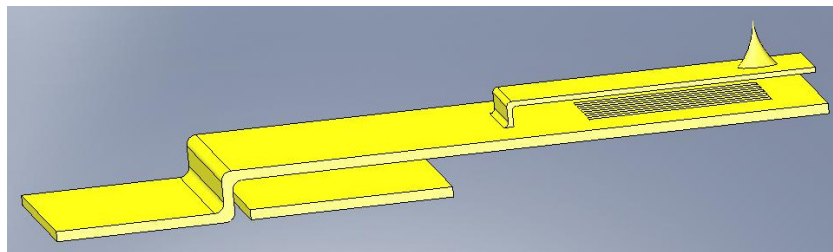


Figure 2.1: Schematic of the Dual Cantilever AFM Probe

Note from Figure 2.1 that a diffraction grating is integrated into the actuator cantilever such that interferometric detection is possible. The larger cantilever is electrostatically actuated via the fixed electrode on the substrate; applying a DC bias voltage between the fixed-free beam and the electrode will cause the free end of the beam to deflect in the z-axis, thus eliminating the need for a z-piezo. The advantage of using electrostatic actuation lies in the ability to utilize the full dynamics of the micro-cantilever actuator, as opposed to piezoelectrics which have a fixed low-frequency cutoff. Also, since the diffraction grating is mobile with the actuator (as opposed to fixed on the substrate like the current FIRAT probe), the hindrance of quarter-wavelength scanning range is no longer an issue. In fact, the actuator cantilever could potentially displace several microns, depending on the design of the device. Figure 2.2 is a schematic of the electrostatic actuation scheme in regards to an applied DC bias and signal input.

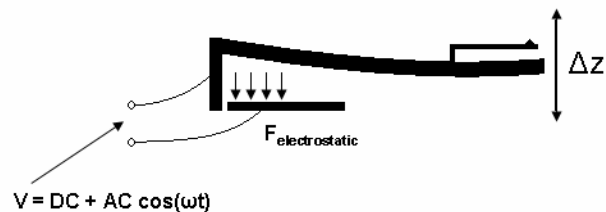


Figure 2.2: Schematic of Electrostatic Actuation

Both cantilever structures are to be composed of Silicon Nitride, a transparent material currently used for some commercial AFM micro-cantilevers. The actuator cantilever will possess an electrode and grating composed of some known adhesive metal (Ti, Cr, Au, etc.). The sensor cantilever will possess a layer of the same metal for the purpose of

reflecting the incoming light from the diffraction grating. Figure 2.3 illustrates the similarity between the dual cantilever probe and the current generation of FIRAT probes.

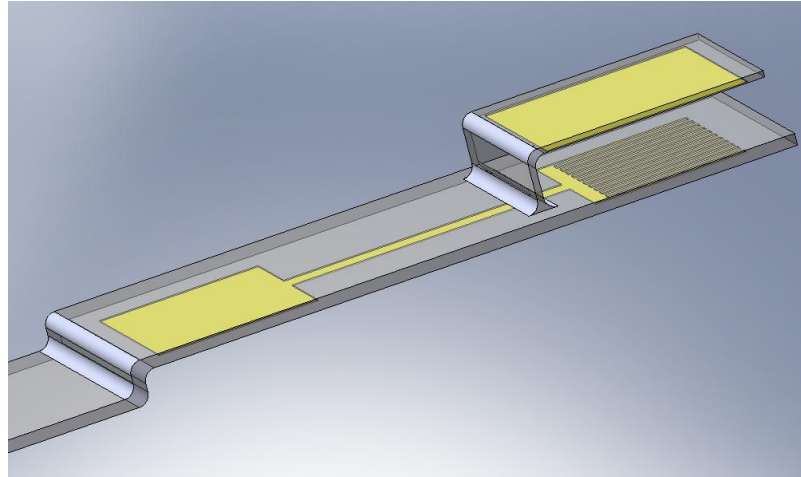


Figure 2.3: Illustration of Silicon Nitride Dual Cantilever (Sans Tip)

The gap between cantilevers will be tailored such that the sensor cantilever is fixed at the optimal distance from the diffraction grating; there will be little or no need for biasing the sensor cantilever to the optimal sensitivity point. Since the actuator and sensor are now physically separate entities (unlike the current FIRAT probe) the design space is greatly increased and the dynamics of each cantilever can be customized towards its specific function. As later discussed, each cantilever must possess unique stiffness and resonance mode characteristics. These devices will reside on a Silicon substrate enabling a backside cavity release (Figure 2.4); this amendment to the design allows for unobstructed HeNe laser light entry as well as a decrease in viscous damping.

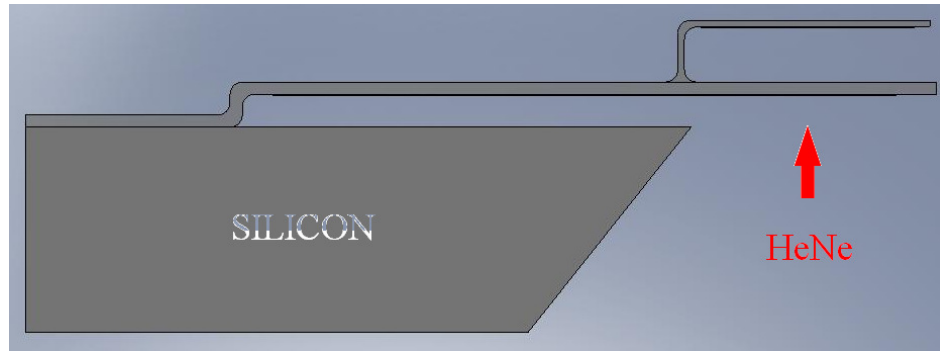


Figure 2.4: Backside Release of a Dual Cantilever Device

The device can be actuated in two ways: a DC bias with an embedded AC signal (to excite resonance in the sensor cantilever through mechanical mode coupling, Figure 2.2) or a DC bias with sensor resonance excited separately (i.e. separate set of AC bond pads). The latter method offers the ability to bias the sensor cantilever to the optimal sensitivity point if needed, since surface micro-machining will not produce the exact air gap size specified in the design. Both methods are equally as effective in providing large-range z-actuation as well as fast-tapping motion. This work will provide evidence of the improvements achievable by the dual cantilever device as well as a novel surface-micromachining fabrication process.

2.2 Seesaw Lever Device

Taking the improvements to an even greater extent is the seesaw lever device. As later detailed in this work, the cantilever actuator requires a substantial DC bias voltage in order to deflect its free end. This high voltage stipulation is inherent in the electrostatic actuation point of the device (Figure 2.2); since the electrodes are located adjacent to the fixed end of the cantilever, the electrostatic force is acting upon the stiffest

region of the structure. The seesaw device aims to remedy this problem by taking advantage of a fundamental lever design (Figure 2.5).

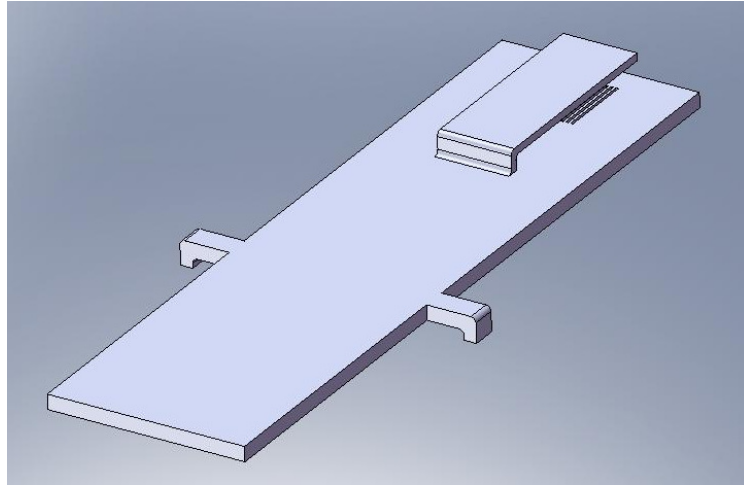


Figure 2.5: The Seesaw Lever Device

In this design, the backside of the lever is electrostatically forced downward, lifting the sensor-end of the seesaw. The mechanical resistance lies in the torsional stiffness of the arm-like supports extending from the midsection of the lever. The first mode shape of the lever device exhibits a seesaw motion which is ideal for large z-range actuation. Unlike the dual cantilever device, the seesaw lever architecture requires significantly less DC bias voltage for nearly 5 times the actuation range (see detailed analysis in later chapters). Also, since the real estate beneath the sensor-end of the lever is no longer occupied by an electrode, a larger backside release is possible thus further mitigating the effects of squeezed-film damping (Figure 2.6).

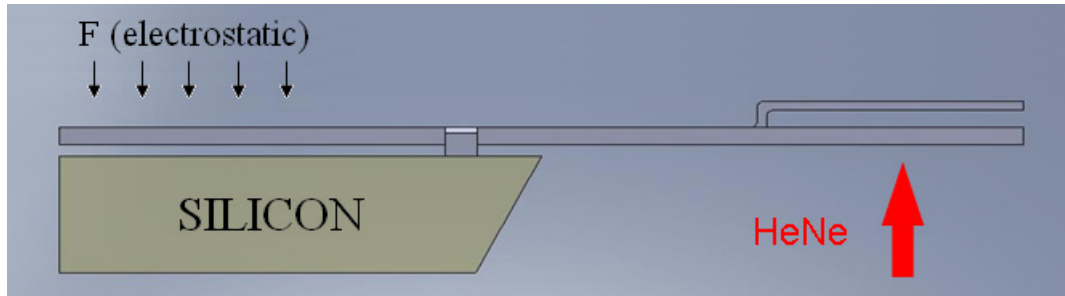


Figure 2.6: Backside Release of a Seesaw Lever Device

The static and dynamic analyses of the seesaw lever structure are essentially the same as for the dual cantilever structure. The mathematics is more complex since it is no longer based on beam bending theory; the structure's mobility mimics that of a pivot-plate resonator for which closed-form solutions are obtainable [15]. Again since the actuator is scaled down to the size of the sensor, a higher fundamental resonance frequency is observed and therefore we see the desirable broadband frequency response. Figure 2.7 shows the schematic illustrations of two variations on the seesaw lever design.

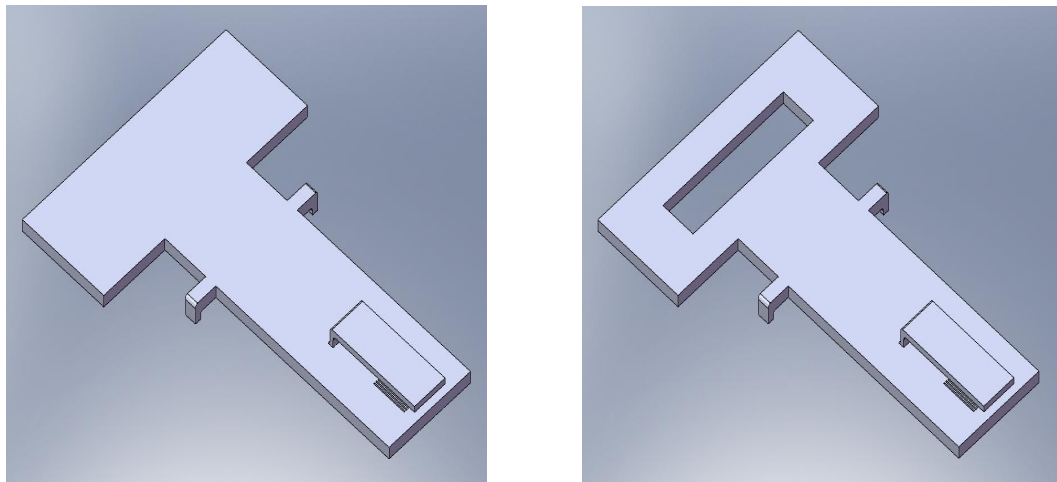


Figure 2.7: Variations of the Seesaw Lever Structure

The structure on the left (variation 1) in Figure 2.7 has a larger back-end surface area and thus aims to lower the electrostatic bias voltage. The structure on the right (variation 2) has a vent hole that will allow trapped air to flow with less restriction.

2.3 Sensor Structures

The figures thus far depict the sensor to be a micro-cantilever atop either another cantilever actuator or a seesaw lever. In this work, both cantilever and bridge sensors (similar to the second-generation FIRAT devices) will be considered; Figure 2.8 shows the two variations.

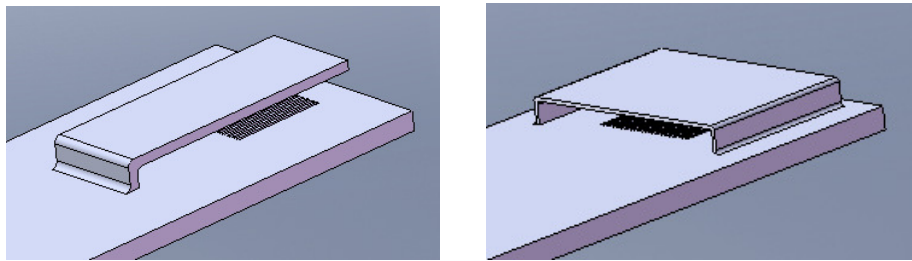


Figure 2.8: Two Types of Sensor Structures

The bridge structure on the right is essentially a second-generation FIRAT probe, just on a moving actuator cantilever or seesaw lever. The dynamics of the bridge structures are very well known since this architecture has previously performed AFM imaging experiments [11]. A side-by-side comparison of every possible combination (i.e. bridge-on-cantilever, cantilever-on-seesaw, etc.) will help illustrate the advantages and disadvantages to each design as predicted by finite element and analytical simulations.

2.4 Metrics

Since the dual cantilever and seesaw lever devices aim to incorporate a fast z-actuation component in the AFM probe itself, this eliminates the need for a relatively slow z-piezo actuator. The actuator must possess dynamics such that it can be electrostatically deflected at high frequencies without exhibiting irregularities such as extreme overshoot or phase shifting greater than 45 degrees. The extent to which the actuator can respond to a modulated signal without these irregularities is known as the bandwidth. Figure 2.9 illustrates the concept of bandwidth using the frequency response of an accelerometer [19].

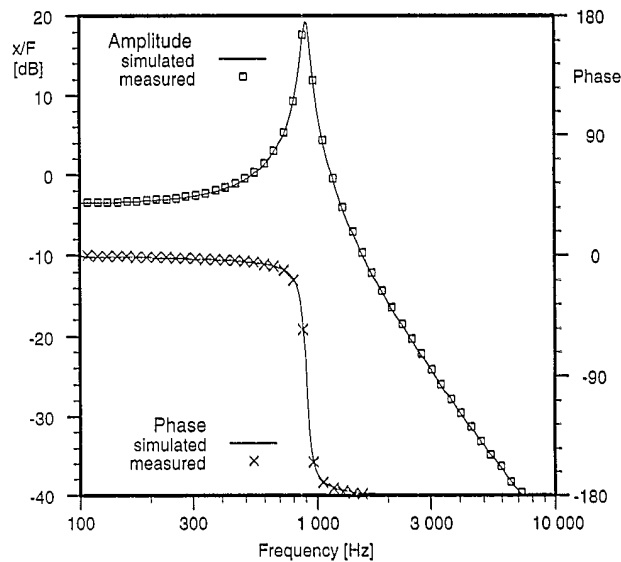
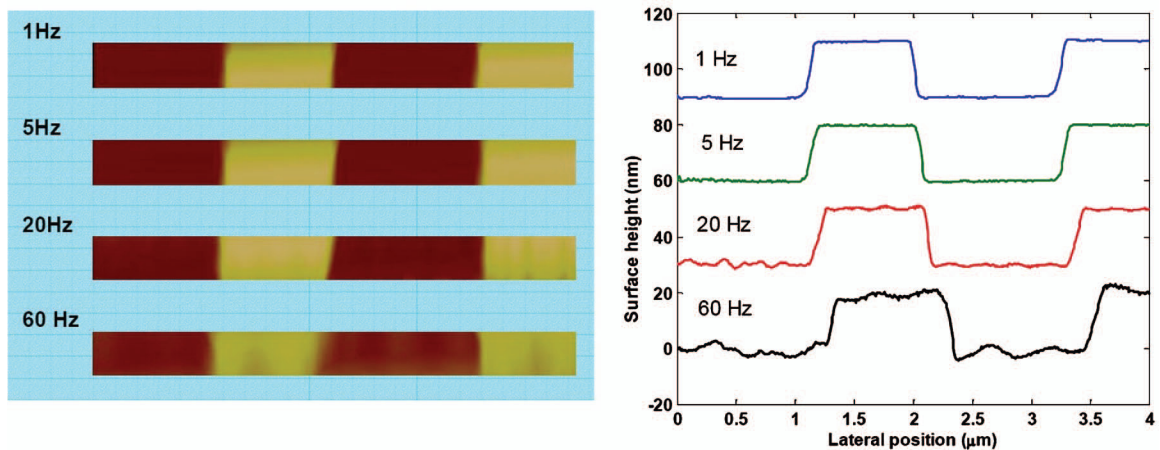


Figure 2.9: Frequency Response of an Accelerometer [19]

The fundamental resonance of the device becomes evident at approximately 1 kHz; this is also exactly when a phase shift occurs. An accepted means of determining bandwidth is the 3-decibel (3dB) approach. Starting at DC (or zero frequency), the 3dB point is where

the response deviates by plus or minus 3dB; in the case of Figure 2.9 this occurs at approximately 500 Hz. The bandwidth of the device can also be obtained by observing where the phase shift occurs, however this is not the case with Figure 2.9 since the 3dB cutoff frequency occurs first. Ultimately, the accelerometer outlined in [19] has a useable bandwidth of 500 Hz. Since commercial z-piezo actuators are limited to a bandwidth of approximately 2.5 kHz [8], it is essential that the bandwidth of the actuator in the dual cantilever or seesaw lever scheme be on the order of 20 to 100 kHz to display any significant improvement. The larger the bandwidth of the z-actuation scheme, the faster the AFM probe can track changes in surface topography. An excellent representation of improved z-actuation bandwidth can be seen in Figure 2.10 [11]; the FIRAT probe utilizes a high bandwidth electrostatic actuator as opposed to a commercial z-piezo signal (the two outputs are compared). A substantial burden is alleviated if this is realized and what remains to be improved are the components of the feedback circuitry.



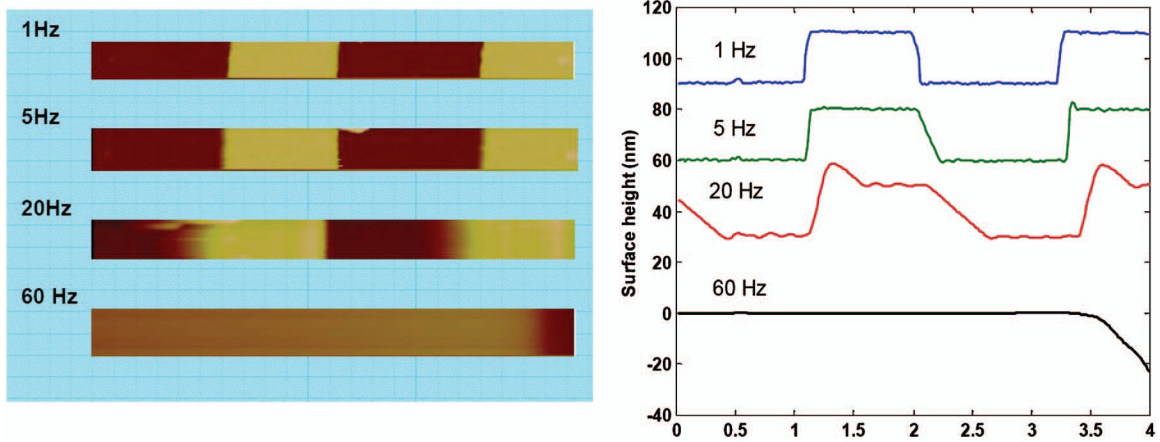


Figure 2.10: Top – FIRAT Fast Electrostatic Actuation. Bottom – Commercial z-Piezo

Although the bandwidth of the z-actuation scheme in Figure 2.10 (top) is quite high, the image begins to degrade when scanned at 60 Hz; it is still limited by the imaging bandwidth which is derived from other components in the overall system (such as IC components). Recall from Figure 2.9 that the 3dB cutoff frequency occurs shortly before the first resonance peak of the device. With this in mind, the resonance of the actuator must be targeted well above the 100 kHz mark. The dynamic behavior of a cantilever is well-known and can generally be described by the stiffness and mass of the physical structure; the behavior of the seesaw lever actuator is best estimated by finite element analysis (FEA). The devices will ultimately operate in ambient conditions which cause additional air-stiffness and air-damping, but this will be taken into account in a later chapter.

Another major design consideration is the stiffness of the AFM probe. Since these devices incorporate stacked structures, probe stiffness becomes even more critical. It is desired to have a soft AFM probe such that high force resolution and low force noise can be achieved (on the order of piconewtons [20]) but this consequently decreases the

resonance frequency which leads to slower tapping motion on a sample surface. Stiffer probes are faster but tend to damage soft samples (polymers, biological samples, etc.) and have high force noise in relation, therefore the stiffness goal for the sensor cantilever falls in the range between 5 and 20 N/m. Commercial AFM cantilevers are available with stiffness values between 2.8 and 200 N/m (Veeco Metrology Group) depending on the application and resonance frequency desired by the consumer. The mechanical stiffness of the sensor structure can be obtained from its physical characteristics such as elastic modulus, width, length, and thickness. The actuator must possess stiffness on the order of 2 or 3 times that of the sensor; this ensures a low noise floor while the sensor taps on a sample. If the stiffness of the actuator is equivalent to the sensor, they will both deflect with comparable amplitude during imaging and the signal-to-noise ratio (SNR) will be poor. Considering the aforementioned, the actuator stiffness must be in a range between 80 and 150 N/m; this would ensure an actuator-to-sensor stiffness ratio of 4 at worst and 30 at best.

The quality factor of the device is important when considering the force interaction between the tip and sample. Ambient operation of the device can drastically mitigate the quality factor, which consequently affects other parameters of operation. A high quality factor is required to maintain a minimal tapping force; however a low quality factor is desired to decrease the time constant of the system for fast-imaging purposes. Since the actuator and sensor structures are physically separate entities in this work, each structure can have a designated quality factor that reflects its purpose. The actuator must have a very low quality factor such that overshoot and ringing are not significant issues.

The sensor must have a moderate quality factor of three to ten in order to keep tapping force at a reasonable level.

Since these devices will utilize the same interferometric detection scheme as the FIRAT probe, it is important to consider the reflectance of the metal layers. Since both actuator and sensor structures are to be comprised of transparent Silicon Nitride, a thin metal film (i.e. Titanium, Aluminum, Chromium, etc.) must be deposited on the desired reflective region. Normally this metal deposition would cause a curvature in the structure due to mismatching residual stresses. Since the Silicon Nitride is deposited via low-stress Plasma-Enhanced Chemical Vapor Deposition (PECVD) and is assumed to be much thicker than the reflective layer, the residual bending stress should not be significant. A Helium-Neon (HeNe) laser is commonly used in laboratory AFM setups and exhibits a wavelength of 632.8 nm [21]. According to this wavelength the thickness of the reflective metal layers must be at least one-quarter of the laser light wavelength, or approximately 160 nm, in order to not transmit a significant percentage of the light intensity. Also in regards to the interferometric detection scheme, the laser spot size must illuminate an 8-micron radius surface area at the least. This suggests that the actuator must have a minimum width of 16 microns such that the laser spot has sufficient real estate and maximum light intensity modulation is achieved. This stipulation applies to the sensor as well.

Perhaps the most critical of the design considerations is the surface-micromachining fabrication flow. Logistically it is challenging to fabricate stacked structures and several obstacles arise due to the etch selectivity of the most common materials found in cleanrooms (i.e. Al, Ti, Cu, etc.). It is imperative that the micro-

machined structures are made from low-stress materials due to the risk of residual stresses causing unwanted curvature in the device. Since the devices rely on the interferometric detection scheme, they must remain as flat as possible such that nearly 100% of impinging laser light is reflected to the desired detection area. Metals exhibit poor residual stress characteristics, which can be seen in Figure 2.11 [22]. In this particular case, bi-layer cantilevers were fabricated in which a significant proportion of the thickness was Aluminum.

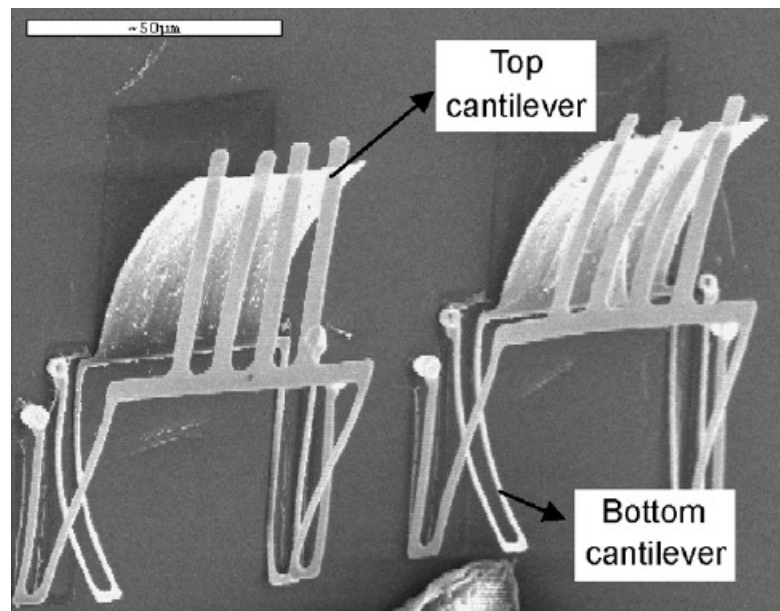


Figure 2.11: Bowed Bi-Layer Cantilever Structures [22]

The authors of [22] ultimately show that the curvature can be mitigated by a process known as rapid thermal annealing, however this does not fully reconcile the adverse effects of residual stresses. As previously mentioned, the structures will be comprised mainly of low-stress Silicon Nitride (measured stress of approximately 20 to 30 MPa in magnitude at 250°C to 300 °C deposition temperature [22]) which has been known to

remain relatively flat even with dimensions on the order of hundreds of microns. Silicon Nitride is also transparent, a very desirable characteristic when dealing with interferometric detection schemes.

The generalized system, schematically illustrated in Figure 2.12, should possess characteristics within the design parameters discussed in this chapter. Table 2.1 is a summary of the desired characteristics for both the actuator and sensor mechanisms.

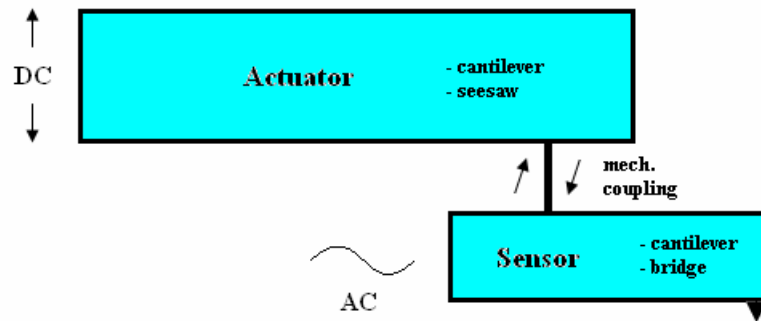


Figure 2.12: Box Schematic Representation of Coupled System

Table 2.1: Desired System Characteristics

	Resonance Frequency (kHz)	Low Frequency cut-off (kHz)	Stiffness (N/m)	Quality (Q) Factor	Electrostatic Displacement (um) / Actuation Voltage (V)	Oscillation Amplitude (nm)
Actuator	200 to 400	20 to 100	80 to 150	< 1	0.5 to 2 / 50 to 200	N/A
Sensor	750 to 1200	N/A	5 to 20	3 to 10	N/A	10 to 20

These parameters are not all-inclusive; however they will be analyzed in detail in the following chapters.

CHAPTER 3:

THEORETICAL AND COMPUTATIONAL MODELING

3.1 Preliminary Design

The static behavior of cantilever beams is very well known and documented. The preliminary dimensions of each cantilever will be strictly based on the design metrics discussed in the previous chapter. To begin, we can first consider the actuator cantilever, which will be used to electrostatically displace the entire system. In order to have a high bandwidth and low noise floor, the fundamental resonance frequency will be targeted at 550 kHz while the stiffness will be targeted at 150 N/m. Using MATLAB (all MATLAB m-files can be found in Appendix B), a chart can be generated to plot cantilever width and thickness versus length such that resonance frequency and stiffness are fixed. Consider equation 1.1 which is a frequency-stiffness-mass relationship [23].

$$\omega_0 = \sqrt{\frac{k_{eff}}{m_{eff}}} \quad (1.1)$$

The notation k_{eff} and m_{eff} refers to effective stiffness and mass, respectively; these parameters are dependent on the type of force loading experienced by the cantilever (i.e. point load, distributed load, etc.) and will be outlined in detail in a later section. Equation 1.2 is an expression for the effective stiffness of a cantilever under distributed loading. The effective mass for a cantilever subject to uniform loading is simply 63% of the actual mass.

$$k_{uniformly-loaded} = \frac{2EWH^3}{3L^3} \quad (1.2)$$

From equation 1.2 we can isolate the known parameters on the right hand side and the design parameters on the left hand side (Equation 1.3). Length, width, and thickness of the cantilever are denoted by L , W , and H , respectively. E represents the elastic modulus of the cantilever material (PECVD Silicon Nitride, ~ 110 GPa).

$$\frac{WH^3}{L^3} = \frac{3k_{\text{uniformly-loaded}}}{2E} \quad (1.3)$$

Using equation 1.2 and the knowledge of effective mass we can transform equation 1.1 into equation 1.4.

$$H = L^2 \left[\frac{(2\pi f_0)^2 3(0.63)\rho}{2E} \right]^{1/2} \quad (1.4)$$

The density of Silicon Nitride, 2200 kg/m^3 , is denoted by ρ . Substituting equation 1.4 into equation 1.3 results in a relationship between cantilever width and length (Equation 1.5).

$$W = L^{-3} \left[\frac{(2\pi f_0)^2 3(0.63)\rho}{2E} \right]^{-3/2} \frac{3k_{\text{uniformly-loaded}}}{2E} \quad (1.5)$$

Plotting Equation 1.5 for a range of cantilever lengths between 50 and 150 microns yields Figure 3.1. The thickness curve (green) can be superimposed onto the plot using Equation 1.4.

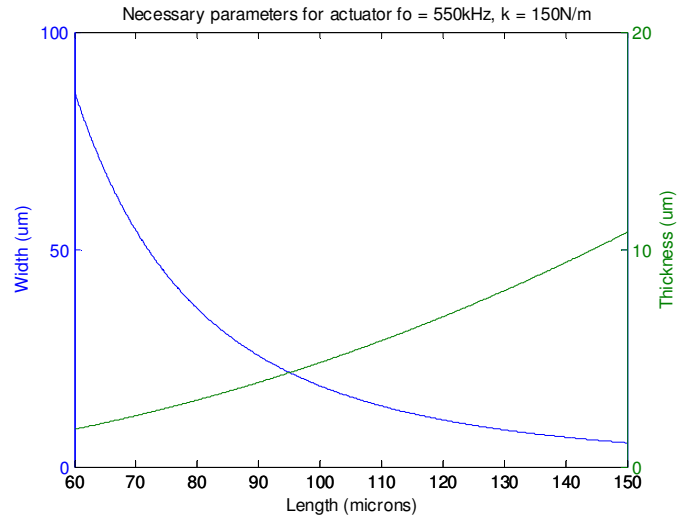


Figure 3.1: Cantilever Width and Thickness Versus Length for $f_0 = 550$ kHz, $k = 150$ N/m

For example, for a 100-mircon-long cantilever with a resonance of 550 kHz and stiffness of 150 N/m, the width and thickness must be approximately 18 microns and 5 microns, respectively. These cantilever dimensions are infeasible mainly due to the thickness; thick Silicon Nitride is difficult to deposit uniformly and is very time consuming. Changing the constant parameters to 400 kHz and 130 N/m produces Figure 3.2. According to the data tips the required width and thickness are 53.9 microns and 2.948 microns, respectively, for a 92-micron-long cantilever.

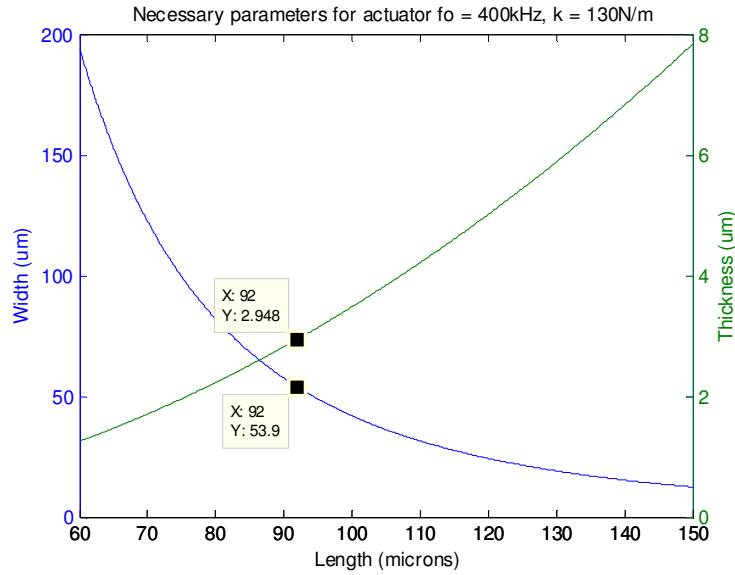


Figure 3.2: Cantilever Width and Thickness Versus Length for $f_0 = 400 \text{ kHz}$, $k = 130 \text{ N/m}$

These dimensions are much more workable for various reasons, primarily the thickness and secondly the width (since the laser spot size adds a width stipulation). Various fundamental resonance frequencies and stiffness values were input into the MATLAB code and later tested in ANSYS for viscous damping effects and electrostatic actuation voltages (see later sections). Table 1.1 lists the dimensions of actuator cantilevers with which this work proceeds.

Table 3.1: Actuator Cantilever Dimensions

f_0 (kHz)	k (N/m)	W (um)	L (um)	H (um)
400	130	53.9	92	2.948
400	180	74.63	92	2.948
400	70	29.02	92	2.948

The dimensions chosen for this work enable a broad range of testing and versatility.

Next we can consider the sensor cantilever. The preliminary design process is similar; Equations 1.2 through 1.5 will differ in constant coefficients since the force-loading changes from uniformly distributed to point-loaded. Equations 1.6 through 1.9 are the undamped governing equations for the sensor cantilever.

$$k_{point-loaded} = \frac{EWH^3}{4L^3} \quad (1.6)$$

$$\frac{WH^3}{L^3} = \frac{4k_{point-loaded}}{E} \quad (1.7)$$

$$H = L^2 \left[\frac{(2\pi f_0)^2 4(0.24)\rho}{E} \right]^{1/2} \quad (1.8)$$

$$W = L^{-3} \left[\frac{(2\pi f_0)^2 4(0.24)\rho}{E} \right]^{-3/2} \frac{4k_{point-loaded}}{E} \quad (1.9)$$

In the case of the point-loaded cantilever, the effective mass becomes 24% of the actual mass. According to the design metrics, the stiffness of the sensor cantilever must be between the range of 5 and 20 N/m. Since the probe will be operated in tapping mode, a high resonance frequency is desired. More information in a short time period is accrued when the tapping motion occurs at a very high frequency (i.e. 700 or 800 kHz). Commercial tapping mode cantilevers possess resonance frequencies on a broad range; Veeco Metrology Group offers tapping mode cantilevers from 20 kHz to 525 kHz. This work aims to raise the tapping mode cantilever resonance as it is required by the fast z-actuation scheme. Figure 3.3 is another design plot that compares cantilever width and thickness with length for a chosen resonance frequency and stiffness.

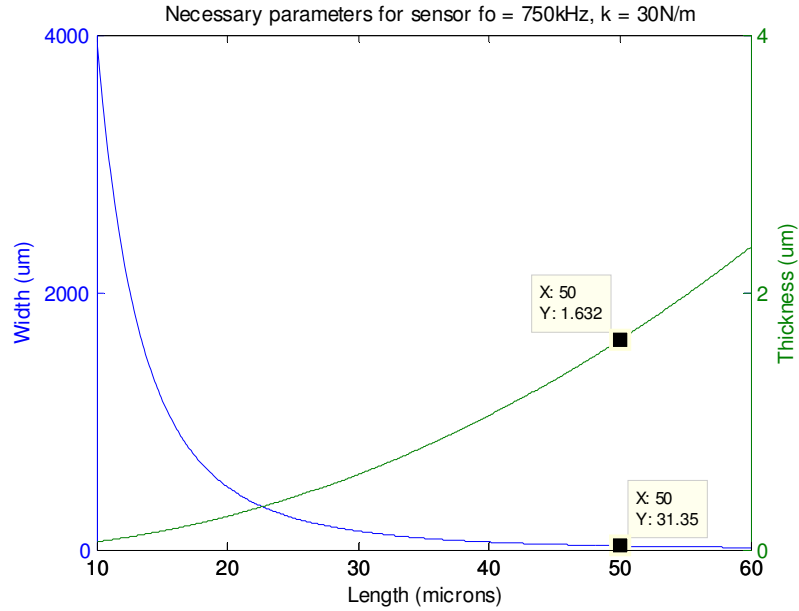


Figure 3.3: Cantilever Width and Thickness Versus Length for $f_0 = 750$ kHz, $k = 30$ N/m

After several iterations, taking viscous damping and electrostatic actuation into account, a set of dimensions were finalized for the sensor cantilevers (Table 3.2). Once again, this set of dimensions provides a versatile platform for testing.

Table 3.2: Sensor Cantilever Dimensions

f_0 (kHz)	k (N/m)	W (um)	L (um)	H (um)
750	15	15.67	50	1.632
750	30	31.35	50	1.632
750	20	20.9	50	1.632

The detailed analysis (viscous damping, actuation voltage, etc.) of the cantilevers from Table 3.1 and Table 3.2 will be presented in later chapters. It should be noted that ambient conditions drastically affect the operation of AFM cantilevers and while the static characteristics of the device are helpful in a preliminary manner, they should be

regarded as a starting point. Numerous simulations were executed in order to fine-tune the response of these devices and the dimensions in Table 3.1 and Table 3.2 are based upon those simulations. It should be noted that previous design specifications exist for the second generation FIRAT probes and thus the bridge sensors in this work will be based upon those specifications.

The dimensions have also been chosen to facilitate fabrication; the actuators are all equivalent in thickness and therefore several device combinations can be fabricated on one wafer. Due to the limitations of thin film deposition methods, the entire wafer must have a uniform thickness of Nitride after deposition and all patterned cantilevers will thus be the same thickness. This same concept holds for the sensors since they are all equivalent in thickness, as well.

Since simple closed-form approximations for torsional resonators do not readily exist, the preliminary design specifications for the seesaw lever devices will be based on the shortcomings of the cantilever structures (i.e. high electrostatic actuation voltages, viscous damping, etc.). The same resonance and stiffness requirements apply for these structures; however they must be modeled in ANSYS in order to achieve an accurate estimate of their behavior. Detailed seesaw lever and bridge analyses will be outlined and discussed in the following chapters.

3.2 ANSYS Finite Element Modeling

3.2.1 Background and Motivation

Finite element modeling (FEM) is very beneficial in regards to analyzing complex three-dimensional structures in an engineering sense. This method of modeling complex

structures was conceived in the 1940's approximately a decade before the idea of Component Mode Synthesis (CMS, also utilized in this work as an analytical method) [24, 25]. Often it is not possible to obtain closed-form solutions of complex systems; the dual cantilever system is a prime example of such a situation. Since this work relies heavily on the analysis of simple cantilever beam, bridge, and seesaw lever structures, FEM is an optimal method of system characterization. Each structure in the system (a total of two) is thus meshed with Euler-Bernoulli beam elements with the intention of estimating the behavior of the global system. The following sections will detail these analyses:

- Force / Static
- Modal
- Viscous Damping
- Electrostatic

The order of these analyses is intuitive in that first the static behavior of the structures must be well known before any dynamic properties (viscous damping, harmonic excitation, transient response, etc.) can be considered in the design.

3.2.2 Force / Static Analysis

In the case of the cantilever beam, the maximum deflection occurs at the free end while in the case of the fixed-fixed beam, the maximum deflection occurs at the center. As expected the spring constant effectively changes according to the loading scheme. Figure 3.4 illustrates some possible loading situations for cantilever beams. The spring constant pertaining to each loading event is therefore referred to as the effective spring

constant and is commonly used in determining the fundamental resonance frequency of the structure.

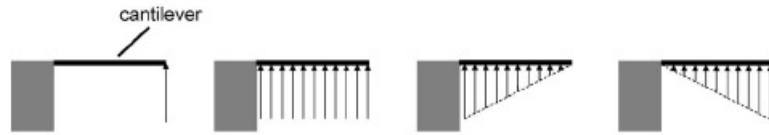


Figure 3.4: Cantilever Beam Subject to Different Loading Schemes [26]

This information is critical considering the forces applied to each cantilever in the dual cantilever system. The larger base cantilever will experience a distributed load due to electrostatic force while the smaller cantilever will experience a point load from striking a sample surface with a sharp tip. Since the latter case is both simple and well-known, we will consider it first. In ANSYS, a three-dimensional model was constructed using SHELL43 elements. These elements are well suited to model linear, warped, moderately-thick shell structures [27]. The element has six degrees of freedom at each node: translations in the nodal x, y, and z directions and rotations about the nodal x, y, and z axes [27]. The model has clamped boundary conditions at the fixed end. By applying a single point load of one Newton at the free end, the ratio of Newtons per meter can be obtained from the resulting maximum beam deflection. Figure 3.5 illustrates the deflection resulting from a point load. All ANSYS batch codes can be found in Appendix B.

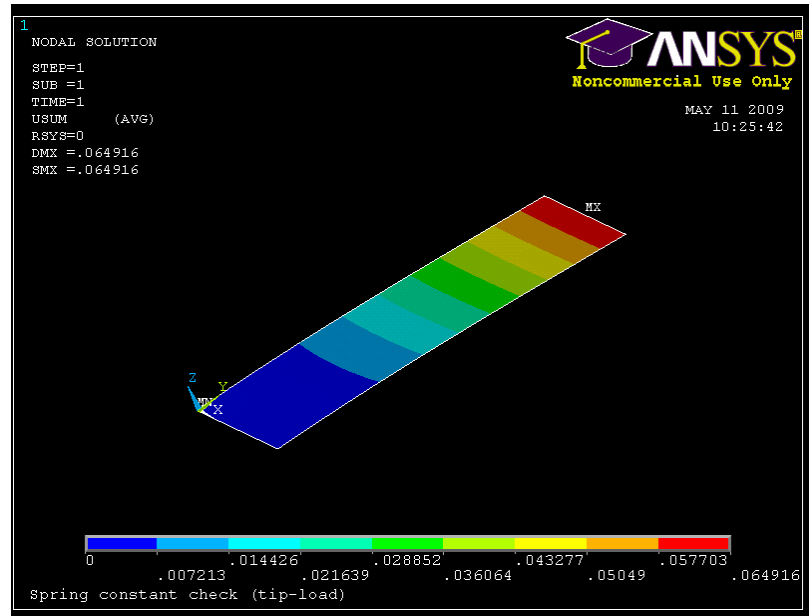


Figure 3.5: Nodal Displacement Contour Plot for an End-Loaded Beam

In this specific case, the maximum free-end deflection is 0.064196 meters (ANSYS does not produce units; they must be user-specified in the routine). Therefore the effective spring constant for this specific loading configuration is 0.064196^{-1} or 15.577 N/m. The beam used in this example has a width, length and thickness of 15.67 microns, 50 microns and 1.632 microns, respectively. The material properties are assumed to be that of Silicon Nitride (Elastic modulus of 110 GPa and density of 2200 Kg/m³). Table 3.3 summarizes the effective spring constants of the end-loaded sensor cantilevers considered in this work. The effective spring constant is denoted by k while the width, length and thickness are denoted by W, L and H, respectively.

Table 3.3: Effective Spring Constants of End-Loaded Cantilever Beams

k (N/m)	W (um)	L (um)	H (um)
15.577	15.67	50	1.632
31.037	31.35	50	1.632
20.650	20.9	50	1.632

Equation 3.10 is the closed-form solution for the effective spring constant of end-loaded rectangular cantilever beams [26]. As expected, the expression has a linear dependence on beam width.

$$k_{end-loaded} = \frac{EWH^3}{4L^3} \quad (3.10)$$

Figure 3.6 is a comparison between the finite element method and this particular closed-form solution (Equation 3.10). Notice as the width-to-length ratio approaches unity the methods start to disagree in accuracy.

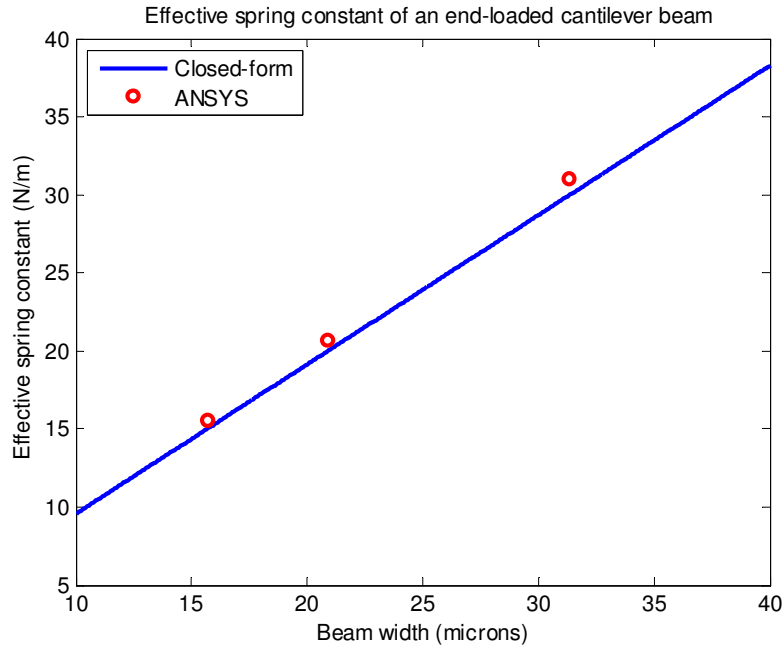


Figure 3.6: Comparison of Effective Spring Constant Calculation Methods

The discrepancy in methods can be attributed mainly to the inaccuracy of Equation 3.10. For example, it has been shown that for end-loaded rectangular cantilever beams the effective spring constant is not described by Equation 3.10 but rather by Equation 3.11 [28]. They differ only slightly, but this constant factor is integral in design considerations.

$$k_{end-loaded} = \frac{EWH^3}{3.8828L^3} \quad (3.11)$$

Using Equation 3.11 instead of Equation 3.10 for the closed-form comparison with ANSYS produces a much better linear fit to the three data points (Figure 3.7).

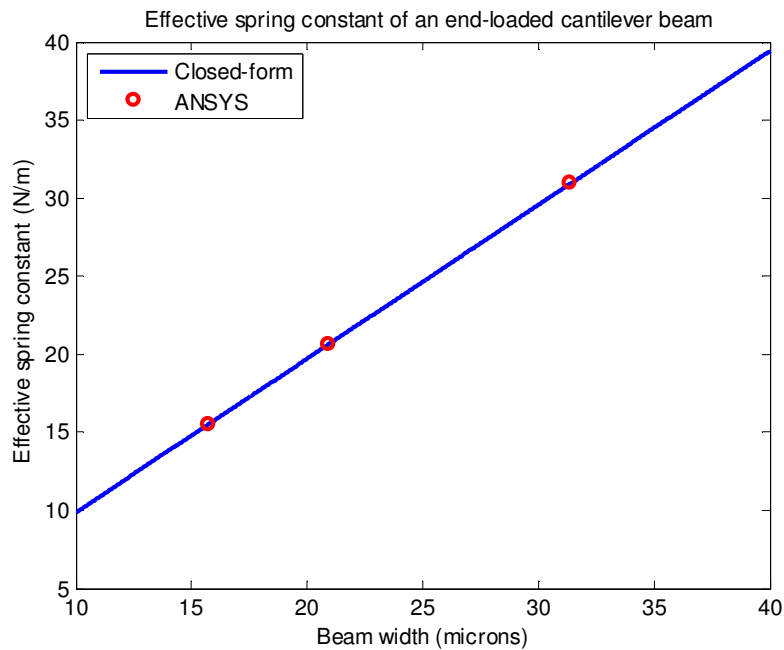


Figure 3.7: Method Comparison Using a Closed-Form Solution

Best results are obtained by finite element analysis [26] since this method can compensate for irregularities in aspect ratio such as anticlastic curvature. If the exact geometry of the beam is known, as well as its material properties, the most accurate design tool is finite element analysis (in absence of a purely analytical solution, which is often unobtainable).

Cantilevers under distributed loading are a bit more complex to analyze. Using the same beam and boundary conditions as seen in Figure 3.5 we can estimate the effective spring constant of this loading scheme. To begin, we can assume uniform pressure acting on the entirety of the cantilever surface area (Figure 3.9). This assumption is in fact not the case for the actual device; however it is a means of verification since closed-form solutions readily exist for such a loading scheme [26]. Figure 3.8 is a displacement contour plot for the uniformly loaded beam.

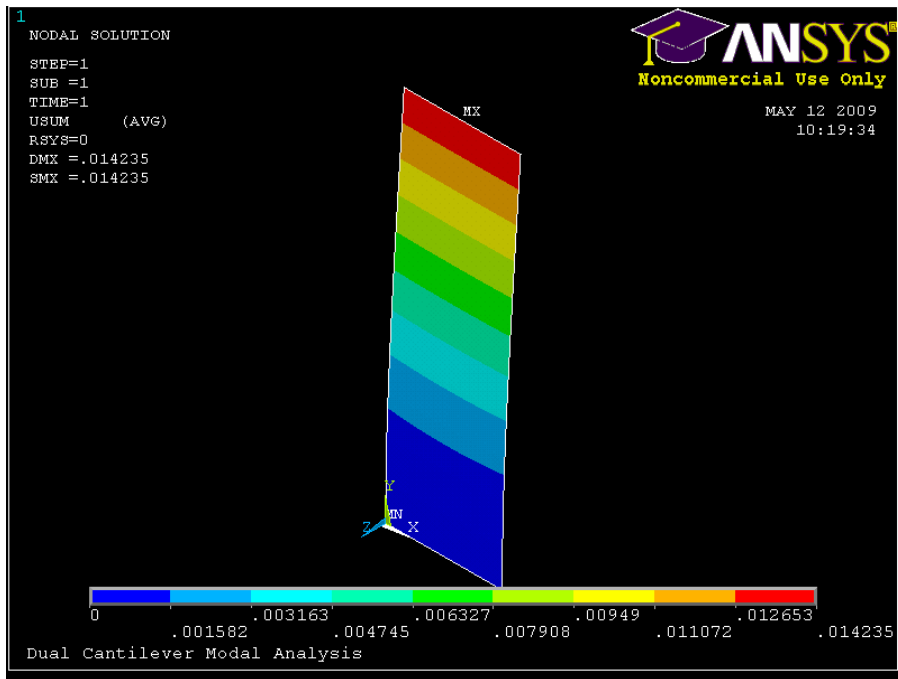


Figure 3.8: Nodal Displacement Contour Plot for Uniformly-Loaded Beam

Again the effective spring constant is the reciprocal of the free-end displacement (0.014235^{-1} N/m) or 70.249 N/m. Just as an aside, if this beam were analyzed using the end-loading method, the effective spring constant would be approximately 28 N/m; an error of 60%. Table 3.4 is a listing of the effective spring constants for the large cantilever beams used in this work.

Table 3.4: Effective Spring Constants of Uniformly-Loaded Cantilever Beams

k (N/m)	W (um)	L (um)	H (um)
132.890	53.9	92	2.948
185.701	74.63	92	2.948
70.249	29.02	92	2.948

Using Equation 3.12 we can form a comparison between the closed-form solution [26] for a uniformly-loaded cantilever beam and the finite element model presented above (see Figure 3.9).

$$k_{\text{uniformly-loaded}} = \frac{2EWH^3}{3L^3} \quad (3.12)$$

It is worthy to note that Equations 3.10, 3.11 and 3.12 differ only by a constant multiplier; the constants can be determined by different mathematical approaches [26, 28].

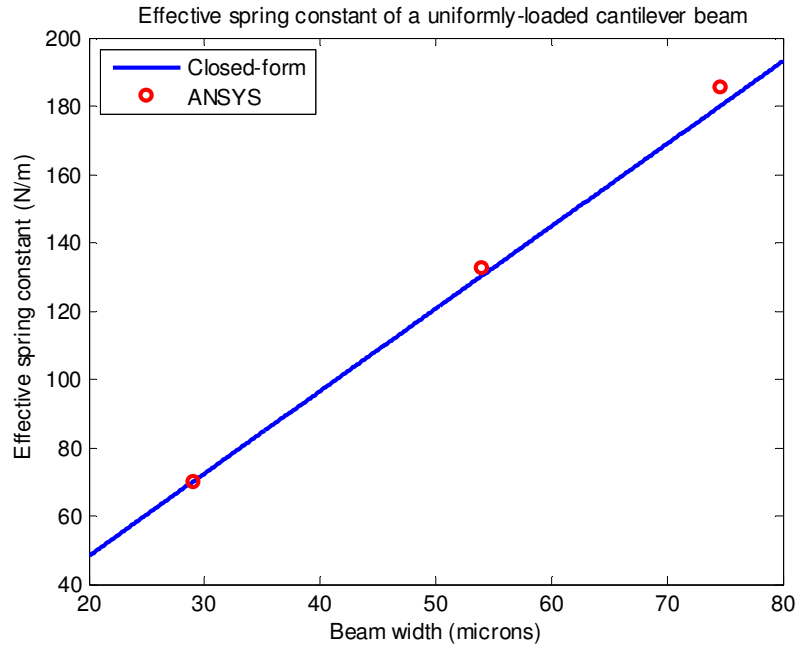


Figure 3.9: Method Comparison using Closed-Form Solution

Again there is a discrepancy between the two methods which becomes evident as the width-to-length ratio approaches unity; once again this can be attributed to the closed-form solution. Since the stiffness characteristics for the two types of loading schemes have been determined, it is now possible to estimate the fundamental resonance frequencies of the various beams in Table 3.3 and 3.4 using both ANSYS and closed-form solutions.

In order to form a comparison between the second generation FIRAT probes and the novel devices in this work, several bridge structures were included in the design phase. The bridge structures under consideration very closely resemble those previously characterized in the literature; however it is essential to estimate their behavior in the same manner as the cantilever and seesaw lever structures. Using ANSYS, the spring constant of each bridge structure in this work was estimated (Table 3.5). Figure 3.10

depicts the displacement contour plot of a bridge sensor with a length, width, and thickness of 50 microns, 20 microns, and 0.4 microns, respectively.

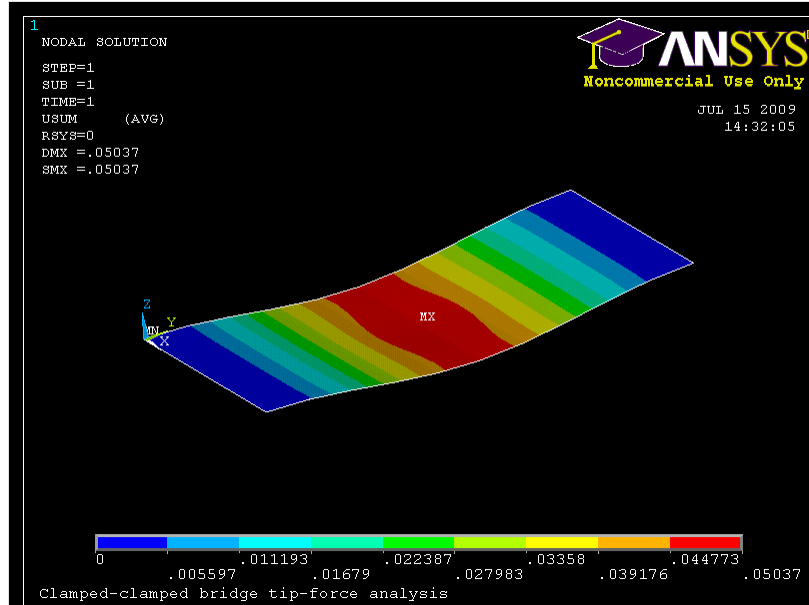


Figure 3.10: Bridge Sensor Contour Plot of Displacement

Table 3.5: Bridge Sensor Stiffness Characteristics

Bridge Sensors			
k (N/m)	W (um)	L (um)	H (um)
27.77315	30	50	0.4
19.85309	20	50	0.4

The bridge structures listed in Table 3.5 are soft in comparison to the second generation FIRAT probes. In order to maintain a high fundamental resonance and good quality factor (outlined later), the mass has been reduced by thinning the structures to 0.4 microns in thickness.

As previously mentioned in the background section of the seesaw lever device, the static and dynamic analyses are very similar to that of a cantilever structure. In order to estimate the stiffness of the seesaw lever, the same exact approach was used in ANSYS; the only difference is the geometry under consideration (Figure 3.11) and the mechanism for which movement occurs (torsion).

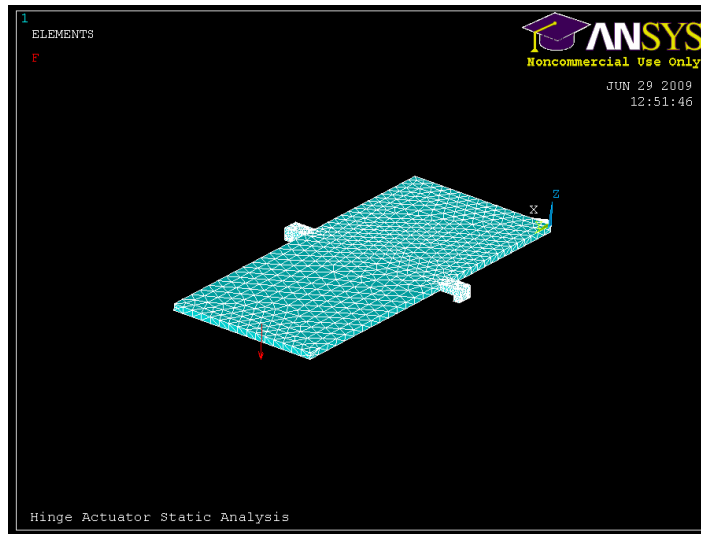


Figure 3.11: FEM of a Seesaw Lever Subject to Static Point Load

From this model, an estimate of the spring constant for each seesaw variation was obtained. Figure 3.12 is a contour plot of the displacement resulting from the one Newton point-load.

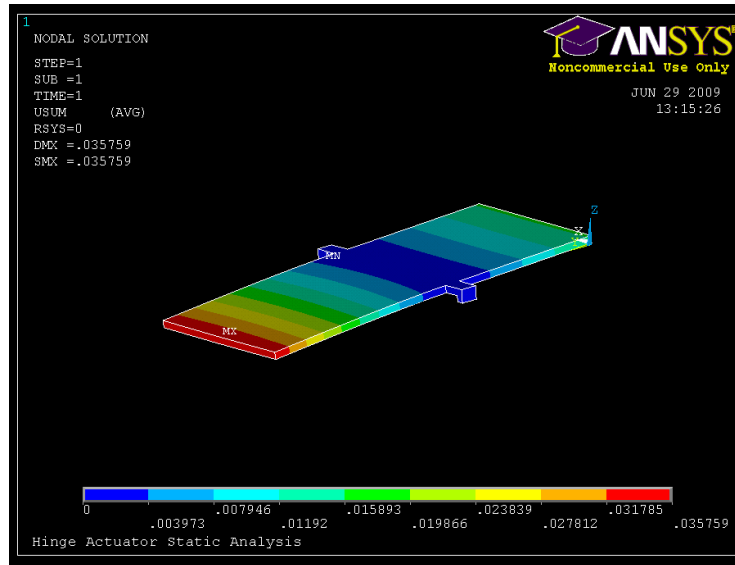


Figure 3.12: Seesaw Lever Displacement Contour Plot

From Figure 3.12 the spring constant for this specific geometry is determined to be 0.035759^{-1} N/m or ~ 28 N/m. The static analysis for each of the seesaw lever variations is identical to that seen in Figure 3.12; while the platform geometry may change drastically, the torsional support arm dimensions more or less stay the same. Table 2.4 is a list of the seesaw lever actuators used in this work, along with their estimated point-loaded spring constants. Note that variations 1 and 2 have extra dimensions that are not listed in Table 3.6 i.e. extension width and length, or vent-hole width and length. These extra dimensions either increase or decrease the mass of the structure, but they do not significantly influence the stiffness.

Table 3.6: Seesaw Lever Actuators and Respective Spring Constants

Hinge Length (um)	Hinge width (um)	Width (um)	Length (um)	Thickness (um)	Hinge offset (um) from center	Stiffness due to 1N point-load at free end (N/m)
Original Seesaw						
10	7	60	150	3	centered	44
10	7	40	150	3	centered	38
10	7	70	160	3	10	28
Seesaw Variation 1						
10	8	40	140	2.5	10	23
Seesaw Variation 2						
10	8	40	140	2.5	10	23

The seesaw lever actuators are substantially softer than the cantilever actuators; this is attributed to the means in which the structure mechanically resists the point-load, as mentioned before. Since the mechanical stiffness has decreased, the mass of the structures has been purposely decreased such that the fundamental resonance frequency does not drop below the hundreds-of-kilohertz range.

3.2.3 Modal Analysis

As previously mentioned, FEM is the most reliable analysis method in absence of a purely analytical solution. The behavior of fixed-free cantilever beams is very well understood and therefore the fundamental resonance frequency can be estimated with great precision using a first-order approximation method [23]. In general, the undamped fundamental resonance frequency (known as the first mode) can be approximated by Equation 3.13.

$$\omega_0 = \sqrt{\frac{k_{eff}}{m_{eff}}} \quad (3.13)$$

Previously we determined that k_{eff} is the effective spring constant of the cantilever according to the loading scheme. The notation m_{eff} refers to the effective mass (also based on loading scheme) and is effectively expressed as αm_{act} where α is the correction factor and m_{act} is the actual mass of the structure. Luckily, the fundamental frequency of a structure does not depend on the loading scheme (only the physical properties of the structure); therefore if the effective spring constant, the fundamental resonance frequency, and the actual mass of the system are known then the correction factor can be estimated. Since we are dealing with simple cantilever structures, the first mode of the system can be deduced from various mathematical methods (energy methods, finite element analysis, etc.). Table 3.7 lists the first modal frequencies and actual masses of the aforementioned cantilever beams as determined by ANSYS.

Table 3.7: Fundamental Resonance Frequencies (ANSYS)

Loading Scheme	fo (kHz)	keff (N/m)	W (um)	L (um)	H (um)	mact (kg)
end-loaded	756.205	15.577	15.67	50	1.632	2.81308E-12
	764.139	31.037	31.35	50	1.632	5.62795E-12
	759.34	20.65	20.9	50	1.632	3.75197E-12
uniformly loaded	407.371	132.89	53.9	92	2.948	3.21608E-11
	409.275	185.701	74.63	92	2.948	4.45299E-11
	403.537	70.249	29.02	92	2.948	1.73155E-11

We can simply multiply our resonance frequencies by a factor of 2π to convert to radians. Solving for the correction factor gives us Equation 3.14 and all necessary information for the calculation can be found in Table 3.7.

$$\alpha = \frac{k_{eff}}{(2\pi f_0)^2 m_{act}} \quad (3.14)$$

Finally, Table 3.8 illustrates the undamped static characteristics of each cantilever beam. From the results we see that the correction factor for end-loaded beams and uniformly-loaded beams is approximately 0.24 and 0.63, respectively (if only two significant figures are considered). There are certainly other means of analytically determining the mass correction factor and ultimately the fundamental resonance frequency of a cantilever beam (Cleveland method, Sader method) [29]; however the method presented here is simply for quick estimate.

Table 3.8: Undamped Characteristics of Fixed-Free Cantilever Beams

Loading Scheme	fo (kHz)	keff (N/m)	mact (kg)	α
end-loaded	756.205	15.577	2.813E-12	0.245281
	764.139	31.037	5.628E-12	0.239235
	759.34	20.65	3.752E-12	0.241785
uniformly loaded	407.371	132.89	3.216E-11	0.630704
	409.275	185.701	4.453E-11	0.630627
	403.537	70.249	1.732E-11	0.631071

Inserting the necessary closed-form solutions into Equation 3.13 allows us to derive an analytical expression for the undamped fundamental resonance frequency of end-loaded cantilever beams (Equation 3.15) as well as uniformly-loaded cantilever beams (Equation 3.16).

$$f_{0,end-loaded} = \frac{1}{2\pi} \sqrt{\frac{25EH^2}{24L^4\rho}} \quad (3.15)$$

$$f_{0,uniformly-loaded} = \frac{1}{2\pi} \sqrt{\frac{200EH^2}{198L^4\rho}} \quad (3.16)$$

These zero-order closed-form solutions are useful for a quick estimate; however they do display some error similar to the previous closed-form expressions presented in this chapter. Air-damping of the cantilever beams can add a significant amount of stiffness and therefore the fundamental resonance frequency will increase according to Equation 3.13. This phenomenon creates a critical design restriction and will be further detailed in a following analysis section.

The undamped fundamental resonance frequencies of the bridge structures were estimated in ANSYS using modal analysis. As with other structures, the bridge device will experience adverse effects due to ambient air operation; these effects will be considered in a following chapter. Table 3.9 lists the fundamental resonance frequencies of the bridge sensor structures considered in this work.

Table 3.9: Undamped Fundamental Resonance Frequencies of Bridge Sensors

Bridge Sensors			
fo (kHz)	W (um)	L (um)	H (um)
1230	30	50	0.4
1220	20	50	0.4

The fundamental resonances of the bridge structures are significantly higher than those of the cantilever sensors; this is essentially attributed to the low mass of the beams.

A modal analysis was completed for each seesaw lever design considered in this work (see Table 3.10). The same approach from the previous sections (cantilever and bridge) was used with only a variation in model geometry. The fundamental resonance

frequency however was not estimated using closed form solutions since the FEA method is proven to produce the most accurate results.

Table 3.10: Fundamental Resonance Frequencies of the Seesaw Lever Actuators

Hinge Length (um)	Hinge width (um)	Width (um)	Length (um)	Thickness (um)	Hinge offset (um) from center	Resonance Frequency (kHz)
Original Seesaw						
10	7	60	150	3	centered	249.393
10	7	40	150	3	centered	300.472
10	7	70	160	3	10	200.06
Seesaw Variation 1						
10	8	40	140	2.5	10	224.658
Seesaw Variation 2						
10	8	40	140	2.5	10	244.084

These resonance frequencies, like the frequencies listed in Tables 3.8 and 3.9, are undamped values. Ambient conditions will be taken into consideration in a following analysis section.

3.2.4 Viscous Damping Analysis

Since the devices in this work rely on electrostatic actuation, small air gaps must exist between electrodes to create a capacitive force. In this case, the cantilever itself serves as an electrode while beneath it the fixed substrate serves as the other electrode (Figure 3.13). With air gaps on the order of three to five microns, the trapping of air during high frequency oscillation becomes an issue; this phenomenon is better known as squeezed-film damping (or viscous damping). During high frequency oscillations the trapped air behaves as a stiff spring in series with the mechanical stiffness of the cantilever beam. In many cases the air stiffness can supersede that of the cantilever and

drastically skew the frequency response. The viscous damping effect can be accurately modeled using various methods [19, 30]; in this work an adaptation from Senturia [23] is utilized.

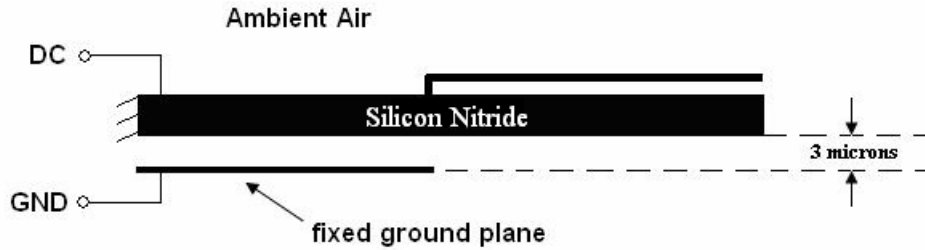


Figure 3.13: Schematic of Electrodes and Air Gap

If we assume an electrical equivalent circuit (Figure 3.14) to represent the mass-stiffness-damper system of the cantilever beam, it is possible to estimate the effect of viscous damping on the harmonic oscillation of the beam.

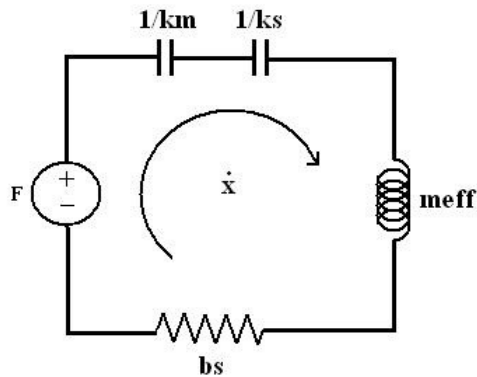


Figure 3.14: Spring-Mass-Damper Equivalent Circuit

In this specific representation, the voltage drop across any of the impeding components is analogous to a force. In the same manner, a capacitor represents a contribution to

stiffness, an inductor represents a contribution to mass, and a resistor represents a contribution to the damping of the system. Finally, the current in the circuit is analogous to the velocity of the oscillating cantilever. Further, k_m denotes the cantilever mechanical stiffness, k_s denotes the stiffness contribution from the air gap, m_{eff} denotes the effective mass, and b_s denotes the damping contribution from the air gap. This is a very useful means of analysis since the impedances of the components in the circuit are frequency-dependent. If we collapse the circuit into its simplest representation (voltage source and equivalent impedance) a relationship between the input (force) and the output (displacement) can be deduced; this relationship is also known as the transfer function of the system. Equation 3.17 expresses each component as impedance and Figure 3.15 depicts the collapsed circuit.

$$Z_{k_m} = \frac{k_m}{j\omega}; \quad Z_{k_s} = \frac{k_s}{j\omega}; \quad Z_{m_{\text{eff}}} = j\omega m_{\text{eff}}; \quad Z_{b_s} = b_s \quad (3.17)$$

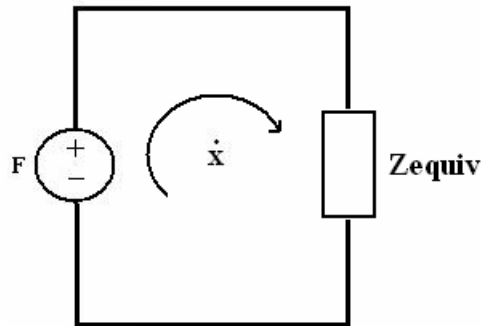


Figure 3.15: Collapsed Equivalent Circuit

The notation j and i are often used interchangeably for imaginary expressions however in this work it will remain as j . The frequency dependence, ω , appears in all impedance

expressions with the exception of the damping contribution. For the calculation this is acceptable but we will later see that the air damping is in fact frequency-dependent as well. Z_{equiv} in Figure 2.15 is expressed as Equation 3.18. Using Ohm's law ($V = iR$) we can form an analogous expression ($F = \dot{x}Z_{equiv}$) to describe the system (Equation 3.19).

$$Z_{equiv} = \frac{k_m}{j\omega} + \frac{k_s}{j\omega} + j\omega m_{eff} + b_s \quad (3.18)$$

$$H(j\omega) = \frac{x}{F} = [(k_m + k_s) - \omega^2 m_{eff} + j\omega b_s]^{-1} \quad (3.19)$$

The substitution $\dot{x} = (j\omega)x$ was made in order to achieve Equation 3.19. Table 2.6 can be condensed into Table 3.11 by combining the mass correction coefficients and the actual masses; therefore all physical static characteristics of the cantilevers are known. What remains to be determined are the stiffness and damping contributions from the air gap. Once again, for lack of a purely analytical, frequency-dependent viscous damping expression we can utilize ANSYS for this step.

Table 3.11: Effective Physical Characteristics

Loading Scheme	fo (kHz)	km (N/m)	m _{eff} (kg)
end-loaded	756.205	15.577	6.9E-13
	764.139	31.037	1.346E-12
	759.34	20.65	9.072E-13
uniformly loaded	407.371	132.89	2.028E-11
	409.275	185.701	2.808E-11
	403.537	70.249	1.093E-11

It is important to note that k_{eff} from table 3.8 is referred to as k_m in Table 3.11. To drastically simplify the model (and still retain accuracy) we can assume small-angle deflections of the beam. This allows us to only consider one-dimensional displacement in the model for viscous damping in ANSYS. The beam structure itself is not considered in the model, only its surface area dimensions (length and width) and the boundary conditions (fixed-free). The air film is compressed and rarified in the same manner regardless of the structure doing the displacing. In ANSYS, the air gap is comprised of three-dimensional squeeze film FLUID136 elements. These elements are used to model viscous fluid flow behavior in small gaps between fixed surfaces and structures moving perpendicular to the fixed surfaces [27]. FLUID136 can be used to determine the stiffening and damping effects that the fluid exerts on the moving structure [27]. The element behavior is based on the Reynolds squeeze film theory and the theory of rarefied gases [27]. There are three options for the FLUID136 element regarding the Knudsen number (Equation 3.20) [27]:

- $K_n < 0.01 \rightarrow$ valid continuum theory
- $K_n > 0.01 \rightarrow$ slip flow boundary
- $K_n > 0.01 \rightarrow$ slip flow boundary with accommodation factors

Since we are not concerned with the reflection of the gas molecules at the wall interface we can ignore the use of accommodation factors.

$$K_n = \frac{\lambda P_{ref}}{d_0 P_{amb}} \quad (3.20)$$

The mean free path of the molecules is described by λ and is approximately $68.9\text{e-}9$ meters for ambient air. P_{ref} and P_{amb} are the reference and ambient pressure, respectively.

Finally, d_0 is the original thickness of the air gap. Since the ambient and reference pressures are equivalent, the Knudsen number can be determined using Equation 3.21.

$$K_n = \frac{\lambda}{d_0} = \frac{68.9e-9}{d_0} \quad (3.21)$$

The air gap for the devices in this work varies from two to five microns, a range for which the Knudsen number always computes to a value greater than 0.01. This being said, the second option for the FLUID136 elements should be utilized as this will compensate for slip flow boundary conditions. Zero pressure is assumed at the fixed-end in order to simulate fixed-free boundary conditions. Since ANSYS uses an iterative approach for the harmonic analysis, the frequency range and step size are user-defined; in this case we are concerned with the behavior of the fluid in the range of zero Hertz to one megahertz. Figure 3.16 is a screenshot of the pressure gradient at 12 kHz oscillation.

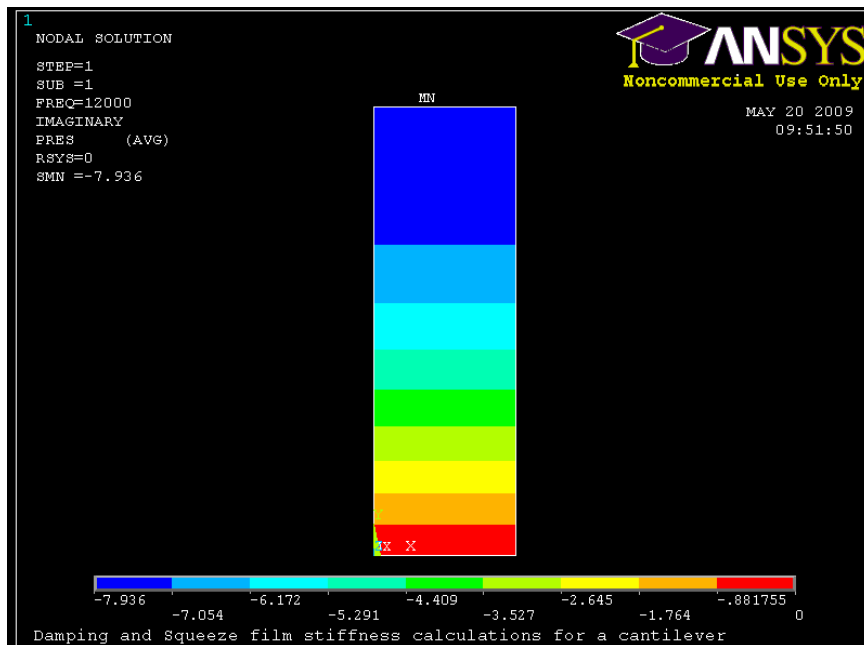


Figure 3.16: Resultant Pressure Gradient at 12 kHz Oscillation

After the frequency range is swept and all nodal information is accrued, some data processing is required to extract the equivalent air stiffness and damping (Equations 3.22 and 3.23).

$$k_s = \frac{F_{imag} \omega}{v} \quad (3.22)$$

$$b_s = \frac{F_{real}}{v} \quad (3.23)$$

The nodal solution from the analysis includes information regarding the velocity (v) of the fluid as well as the resultant forces on the nodes of the fluid elements (which is in the imaginary $a+bj$ form). At this point we have an air-stiffness and air-damping value for every frequency that was specified in the ANSYS iteration. Since the remaining calculations involve matrix mathematics, the data is imported into MATLAB to evaluate Equation 3.19. The magnitude and phase of the transfer function gives an estimate of the useable bandwidth of the cantilever as well as the behavior (quality factor, Q) at resonance.

The bridge viscous damping analysis is nearly identical to that of the cantilever; in this case both ends of the beam remain fixed at zero pressure. Figure 3.17 is a displacement contour plot of an oscillating bridge sensor at one megahertz.

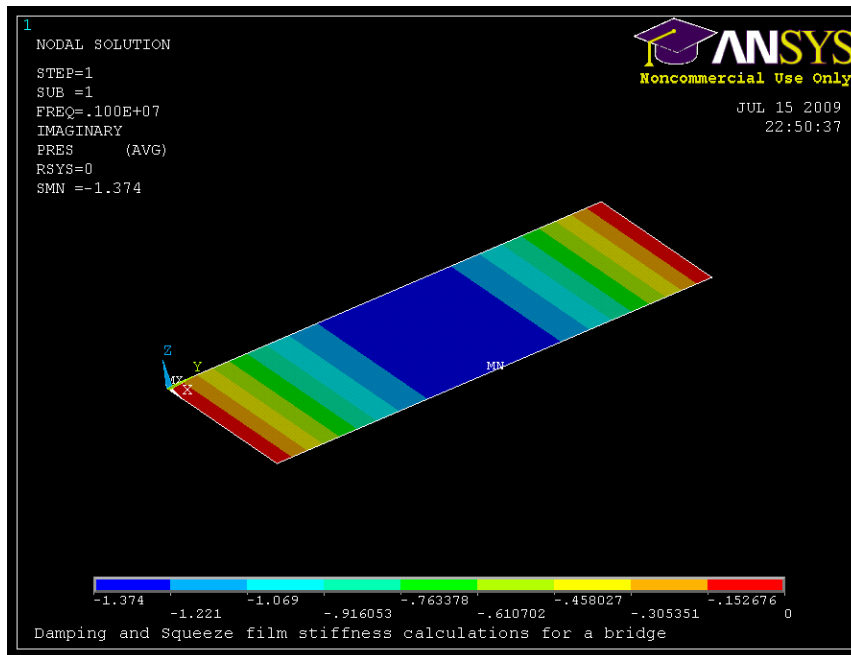


Figure 3.17: Pressure Contour Plot for Bridge Structure at One Megahertz

Again from Equations 3.22 and 3.23 we can compute the air damping and stiffness contributions as a function of frequency. The frequency range for this specific geometry was specified as zero to 1.5 MHz; this is due to the discovery that air damping and stiffness create a substantial shift in the fundamental resonance of these specific bridge structures.

The same fluid boundaries apply to the seesaw lever viscous damping analysis. However, since half of the device will be backside-released, a symmetry condition can be considered in the finite element model. Unlike the dual cantilever, the viscous damping effect does not come from beneath the sensor-end of the seesaw; rather it originates from the side of the seesaw where air gets trapped between the substrate and electrodes. With this in mind, it is possible to model the relevant half of the seesaw in order to capture the effects of viscous damping. Figure 3.18 is a pressure contour plot of a half-seesaw lever

at one megahertz oscillation. In the model, the midsection of the seesaw is confined to zero pressure; the rest of the structure is free to oscillate.

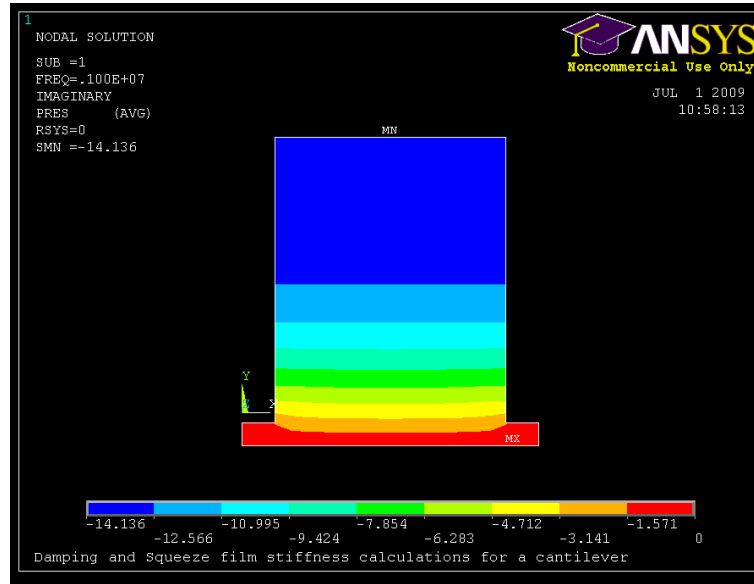


Figure 3.18: FEA Pressure Contour of the Original Seesaw Lever Design

From the modal analysis it is apparent that the center of the seesaw lever does not experience significant motion and thus the pressure is at or nearly zero in this region. Within the specified frequency range (0 – 1 MHz), the seesaw lever only experiences the first and second mode shapes in which no center movement (and no air-trapping under the center) is observed. Thus, the symmetry model is a valid means of FEA for the seesaw lever actuator. Figure 3.19 is a pressure contour plot for variation 1 of the seesaw lever while Figure 3.20 is a pressure contour for variation 2. Notice that in Figure 3.19 the pressure gradient is not quite as uniform as in the case of the original seesaw lever. The pressure distributions are similar for both seesaw lever variations. Both pressure contours are captured at one megahertz oscillation.

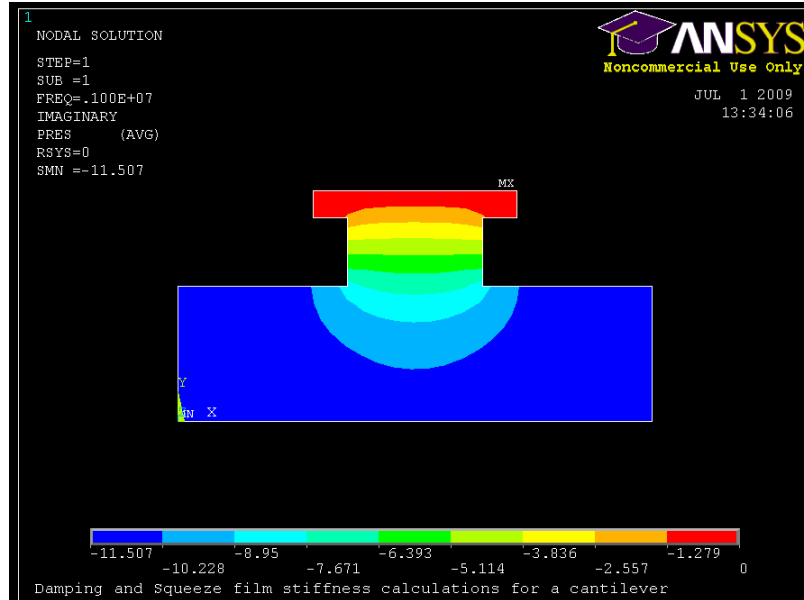


Figure 3.19: FEA Pressure Contour for Seesaw Lever Variation 1

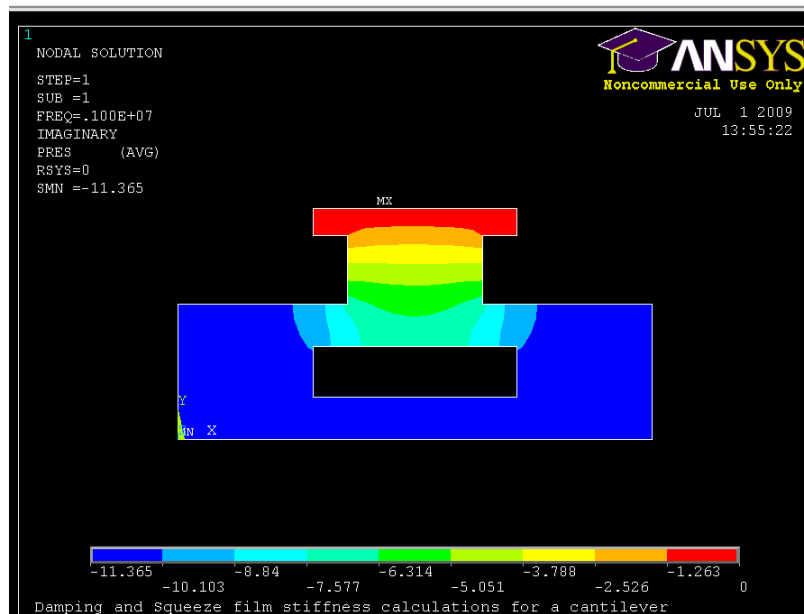


Figure 3.20: FEA Pressure Contour for Seesaw Lever Variation 2

Using the same MATLAB routine, the pressure information from the finite element analysis is converted into a frequency response using the transfer function approach.

3.2.5 Transfer Function

Using a routine written in MATLAB, the transfer function (Equation 3.19) for each cantilever in this work was evaluated for a frequency range of one megahertz. Each cantilever (sensor and actuator) was analyzed as an independent fixed-free beam; this analysis gives an estimate of the coupled system response. Figure 3.21 is the air-damped response of the first sensor cantilever in Table 3.11 and Figure 3.22 is the frequency response of the first actuator cantilever in Table 3.11. As expected, the resonance frequencies have increased due to air-stiffening. The viscous damping phenomenon also has an effect on the quality factor (Q-factor) at resonance.

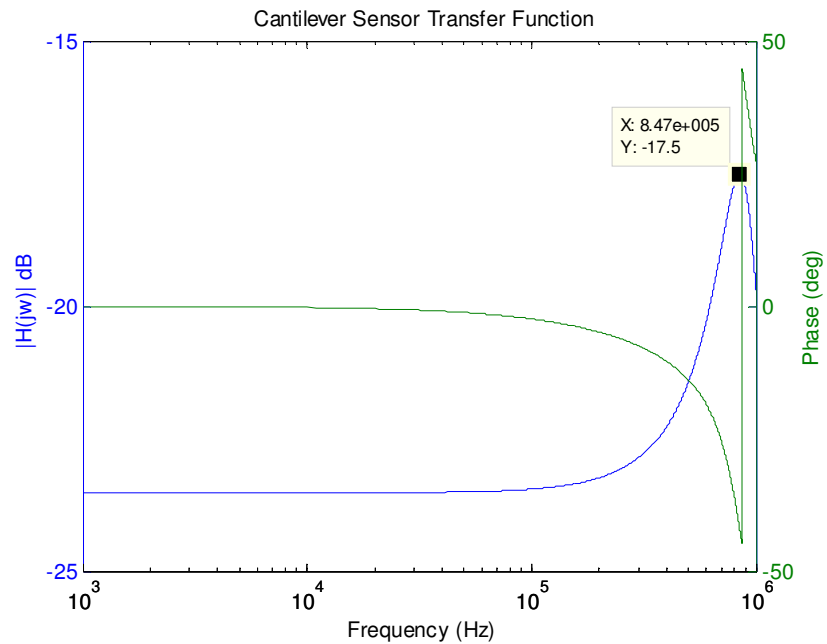


Figure 3.21: Transfer Function (Magnitude and Phase) of a Sensor Cantilever

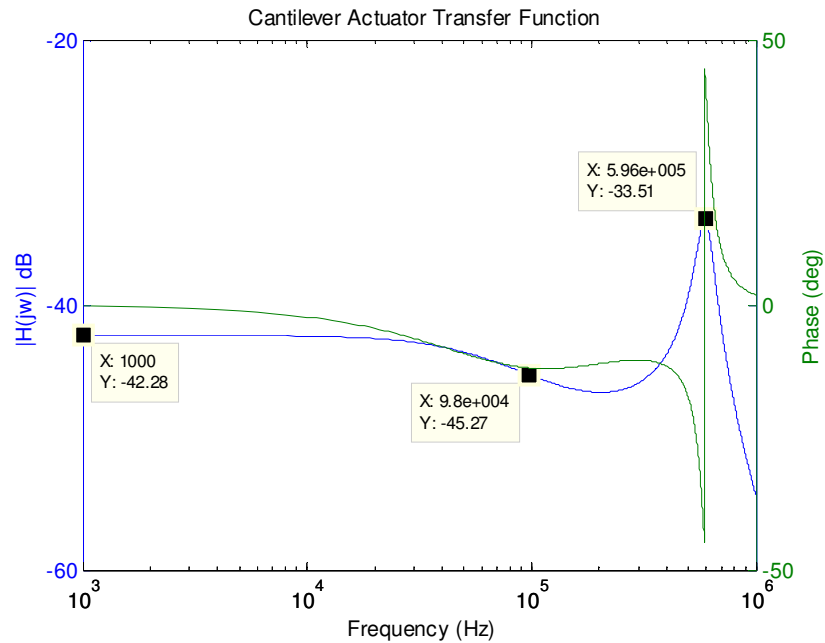


Figure 3.22: Transfer Function (Magnitude and Phase) of an Actuator Cantilever

Quite a bit of information can be gathered from Figures 3.21 and 3.22. In order to convert the transfer function output to decibels, Equation 3.24 was used.

$$dB = 20 \log_{10}(|H(\omega j)|) \quad (3.24)$$

Since the figures represent the transfer function on a decibel scale, the 3 dB bandwidth of the actuator and sensor can be determined. According to the plot the 3 dB cutoff frequency of the actuator is approximately 98 kHz; the cutoff frequency of the sensor cantilever is well above this value. In order to verify that these values are indeed the cutoff frequencies, the phase information of the transfer function must be analyzed. From the figures it is apparent that a 45-degree phase shift occurs at approximately 596 kHz for the actuator and 847 kHz for the sensor. Equation 3.25 is the expression used to extract the phase information from the transfer function.

$$\phi(rad) = \tan^{-1} \left[\frac{\text{Im}\{H(\omega j)\}}{\text{Re}\{H(\omega j)\}} \right] \quad (3.25)$$

The 3 dB cutoff frequency occurs prior to the 45-degree phase shift for both cantilevers, thus the 3 dB values are acceptable. It is important to note that the resonance frequency of the actuator cantilever in Figure 3.22 occurs well before the resonance of the sensor cantilever; this is ideal since it is imperative that minimal energy is coupled to the actuator during sensor tapping (which occurs at sensor resonance). The resonance peak of the actuator cantilever exhibits a moderate Q factor; this can easily be mitigated using low-pass filter circuitry which is capable of 10 dB (or greater) attenuation. The Q-factor can be estimated using the relationship in Equation 3.26 [8]. The Q-factor of the actuator cantilever is not critical (effects will be filtered regardless), however the Q-factor of the sensor cantilever is significant due to its relation to imaging speed and tapping force.

$$Q \cong \frac{f_0}{\text{bandwidth}(3dB)} \quad (3.26)$$

From Equation 3.26 it can be determined that the sensor cantilever in Figure 3.21 has a Q-factor of approximately 1.5. This is a very low Q-factor for a micro-cantilever and in some instances a high Q-factor is desired because of reduced tapping force on the sample [13]. However, the response time (τ_c) scales proportionally to Q and can be seen in Equation 3.27 [13].

$$\tau_c = \frac{Q_c}{\pi f_c} \quad (3.27)$$

For high-speed AFM it is desired to have a rapid response time and therefore either a very high resonance frequency or low Q-factor is necessary. For the sensor in Figure 3.21, the response time computes to approximately half a microsecond; this is potentially

1000 orders of magnitude faster than some micro-fabricated AFM cantilever probes [8]. It is also worthy to note that high-Q systems exhibit instabilities that are detrimental to fast-AFM [8]. Nonetheless, a middle ground between tapping force and response time must be achieved and therefore a moderate Q between one and ten is ideal for this work. Table 3.12 summarizes the important air-damped frequency response characteristics of the cantilevers from Table 3.8. Again note that the Q-factor of the actuator cantilever response is not critical. Also, the air gap for each cantilever is given since this drastically affects viscous damping.

Table 3.12: Cantilever Air-Damped Frequency Response Characteristics

ACTUATOR							
Damped fo (kHz)	Undamped fo (kHz)	k (N/m)	W (um)	L (um)	H (um)	Air gap (um)	3dB Bandwidth (kHz)
593	400	130	53.9	92	2.948	2.5	98
593	400	180	74.63	92	2.948	2.5	99
593	400	70	29.02	92	2.948	2.5	98
SENSOR							
Damped fo (kHz)	Undamped fo (kHz)	k (N/m)	W (um)	L (um)	H (um)	Air gap (um)	Quality
847	750	15	15.67	50	1.632	4	1.3
847	750	30	31.35	50	1.632	4	1.3
830	750	20	20.9	50	1.632	4	1.3

The mechanical stiffness of each cantilever can be observed from the transfer function at DC frequency (or very close to DC, where the response is nearly flat). Inverting Equation 3.24 gives Equation 3.28, which can be used to determine the mechanical stiffness (k_m).

$$k_m = 10^{\frac{dB}{20}} \quad (3.28)$$

Equation 3.28 can be used to find the cantilever mechanical stiffness at other frequency values as well. Using Equation 3.28 to compare the stiffness of each cantilever at the sensor resonance frequency (~ 847 kHz) produces an actuator-to-sensor stiffness ratio of 33 which contributes to a high SNR value (for the specific case in Figures 3.25 and 3.26).

The transfer function for the second bridge sensor listed in Table 3.9 was analyzed in order to gage the viscous damping effects on the fixed-fixed beam structures. The transfer function and phase information was determined using the same MATLAB routine from the previous section; the plot can be seen in Figure 3.23.

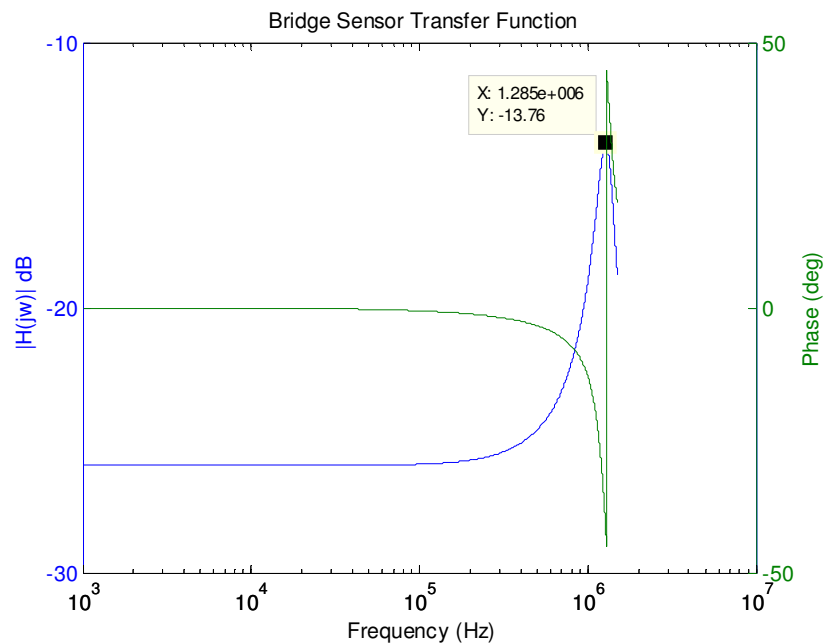


Figure 3.23: Transfer Function (Magnitude and Phase) of a Bridge Sensor

The damped fundamental frequency of the specific bridge sensor seen in Figure 3.23 is once again observed to be shifted to a higher value. In the case of the bridge sensor, the resonance frequency shift is approximately 65 kHz while the cantilever sensor

experienced a resonance frequency shift of approximately 90 kHz. However, the bridge sensor maintains a higher Q than the cantilever sensor (in this case Q is approximately 2). Table 3.13 summarizes the notable damped frequency response characteristics of the bridge sensors used in this work.

Table 3.13: Bridge Air-Damped Frequency Response Characteristics

Bridge Sensors						
Quality	k (N/m)	Damped fo (kHz)	Undamped fo (kHz)	W (um)	L (um)	H (um)
~2	28	1242	1230	30	50	0.4
~2	20	1285	1220	20	50	0.4

The MATLAB routine was altered such that it could compute the frequency response of the seesaw lever. The code basically remains the same; however the mechanical stiffness, effective mass, and ANSYS input are varied. The effective mass was again calculated using the ANSYS approach and is determined to be 24% of the actual mass for the original seesaw lever. The effective mass for variations 1 and 2 is approximately 17% of the actual mass. Figure 3.24 is the frequency response of the first original seesaw lever design seen in Table 3.10.

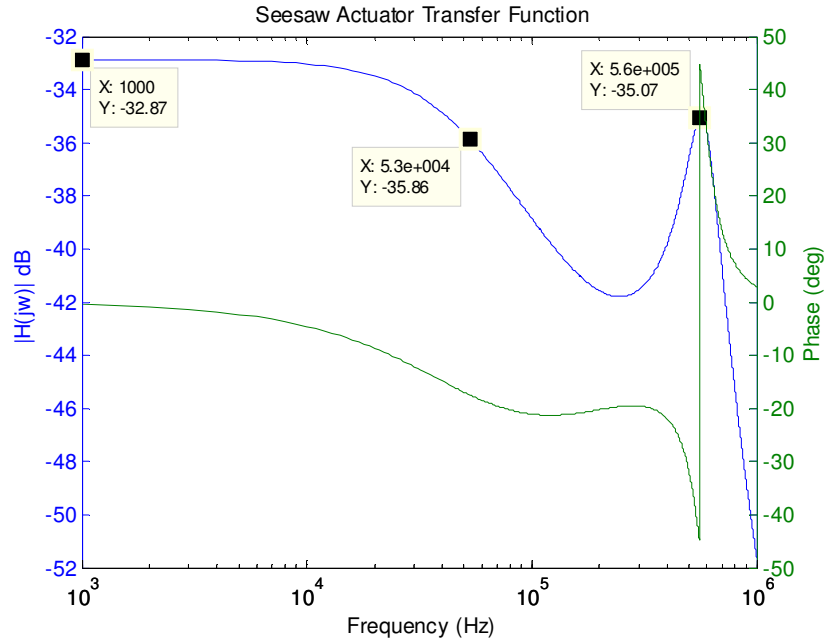


Figure 3.24: Seesaw Lever Transfer Function

From Figure 3.24 we see that even though the stiffness is much less than that of the cantilever actuator, the bandwidth still remains quite high at approximately 53 kHz. The same analysis was completed for the remaining seesaw lever designs; the specifications are outlined in Table 3.14.

Table 3.14: Seesaw Lever Frequency Response Characteristics

Hinge Length (um)	Hinge width (um)	Width (um)	Length (um)	Thickness (um)	Hinge offset (um) from center	damped resonance (mode1) (kHz)	3dB cutoff (kHz)
Original Seesaw							
10	7	60	150	3	centered	567	53
10	7	40	150	3	centered	579	67
10	7	70	160	3	10	572	18
Seesaw Variation 1							
10	8	40	140	2.5	10	780	12
Seesaw Variation 2							
10	8	40	140	2.5	10	746	12

3.2.6 Thermal-Mechanical Noise

Another metric regarding the coupled performance of an actuator and sensor cantilever is the thermal-mechanical (T-M) noise. The thermal noise provides a theoretical minimum at which the system can detect force and displacement at a given ambient temperature and frequency. When attempting to operate at the highest sensitivity point, T-M noise is a critical consideration and is by no means negligible when ambient conditions exist. According to the fluctuation-dissipation theory [31] if there is a mechanism for dissipation in a system, then there will also be a component of fluctuation in that system directly related to that dissipation [32]. This condition holds for a system in equilibrium thus providing the best-case scenario of a noise floor for the cantilever, bridge, and seesaw lever systems. In short, if damping of the cantilever occurs due to the ambient surroundings (therefore causing dissipation of energy), the ambient surroundings must cause a fluctuation in the cantilever due to the random thermal motion of molecules in the air. Equation 3.29 is an expression for the T-M force noise spectral density (also known as the Nyquist relation [31]) while Equation 3.30 is an expression for the T-M displacement noise spectral density. Note that Equation 3.30 is a function of Equation 3.29 and both expressions are frequency-dependent.

$$S_{n,f_m}(\omega) = 4k_b T b(\omega) \quad (3.29)$$

$$S_{n,x_m}(\omega) = S_{n,f_m}(\omega) |H(\omega j)|^2 \quad (3.30)$$

Recall that the impedance related to air-damping is not frequency dependent, however in Equation 3.29 the air-damping value (b) is the only term that can contribute to frequency-

dependence since Temperature (T , 288 K) and Boltzmann constant (k_b , $1.38\text{e-}23$ J/K) are fixed. The same sensor and actuator cantilevers from Figures 3.25 and 3.26 are analyzed with respect to thermal noise in Figure 3.25. Note the frequency dependence of thermal force noise. From the force-noise plot it can be seen that the sensor cantilever has a low force-noise of approximately 200 fN/ $\sqrt{\text{Hz}}$ at its resonance frequency. The SNR at this tapping frequency is therefore quite high in theory if piconewton tapping force resolution is considered; of course, there are several other factors that limit the SNR of the system. Another important observation from Figure 3.25 is the actuator-to-sensor displacement noise ratio.

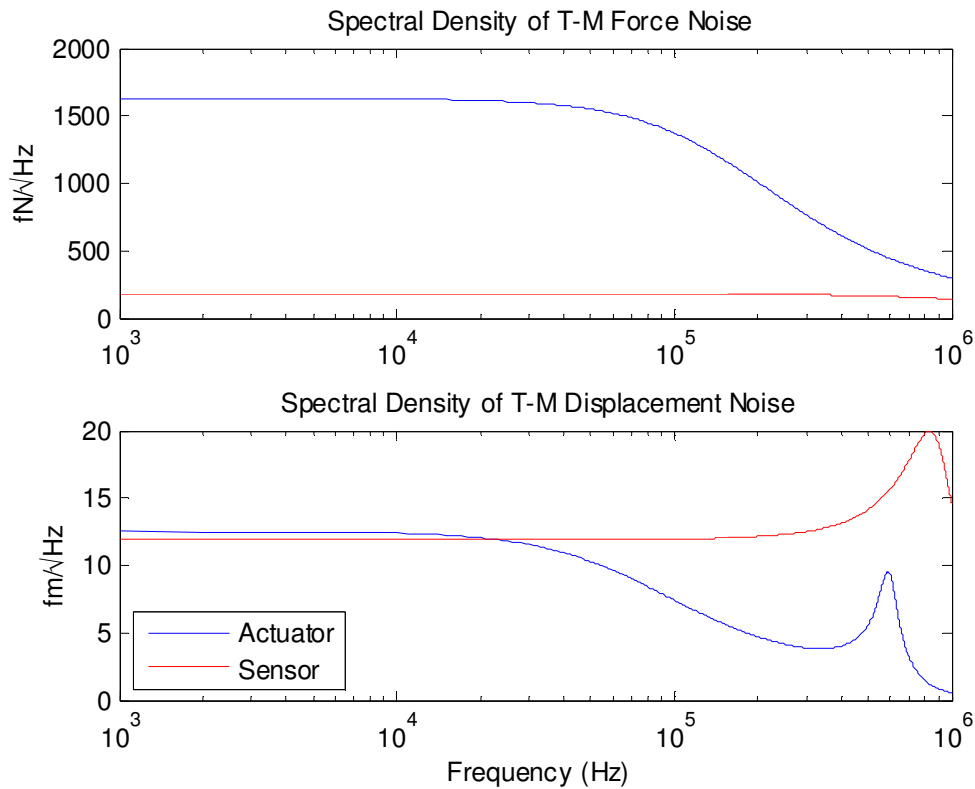


Figure 3.25: Thermal Mechanical Noise: Force (Top) and Displacement (Bottom)

At the sensor resonance frequency the actuator has a displacement noise value of approximately 2 fm/ $\sqrt{\text{Hz}}$ while the sensor has a displacement noise value of 20 fm/ $\sqrt{\text{Hz}}$. If a bandwidth of 100 kHz is considered for the tapping frequency, this results in a force noise of approximately 63 pN and a displacement noise of approximately 6 pm for the sensor cantilever. The remaining cantilevers and seesaw levers considered in this work exhibit very similar T-M force and displacement noise characteristics and hence the quality of their performance can be inferred from the aforementioned.

3.2.7 Electrostatic Analysis

Equally as critical as the previous analyses is the electrostatic analysis in which the actuation voltage is determined. Since an electrostatic actuation scheme is governed by the simple parallel-plate capacitor relationship (Equation 3.31 [23]) it is possible to identify the parameters that will affect actuation voltage.

$$F_{es} = \frac{\epsilon A V_{in}^2}{2g^2} \quad (3.31)$$

In Equation 3.31, g represents the original air gap between the cantilever and the substrate (conventionally referred to as the dielectric); A is the surface area of the electrode, V_{in} the applied DC voltage and ϵ the permittivity of free space ($8.854\text{e-}12 \text{ A}^2\text{s}^4\text{kg}^{-1}$ or $\text{C}^2\text{N}^{-1}\text{m}^{-2}$). F_{es} represents the electrostatic force that results from the input parameters. If we equate Equation 3.31 to Hooke's law ($F_{es} = k_{eff} x$) then it is possible to estimate the static deflection (x) due to an applied DC voltage. Electrostatic forcing is assumed to be uniform on the entirety of the actuator cantilever, therefore from the Force / Static Analysis section we know the effective spring constant for this loading case. However, also mentioned in the Force / Static Analysis section is that the realistic

uniform-loading case does not consider the entire cantilever surface area; Figure 3.26 illustrates why this is not the case.

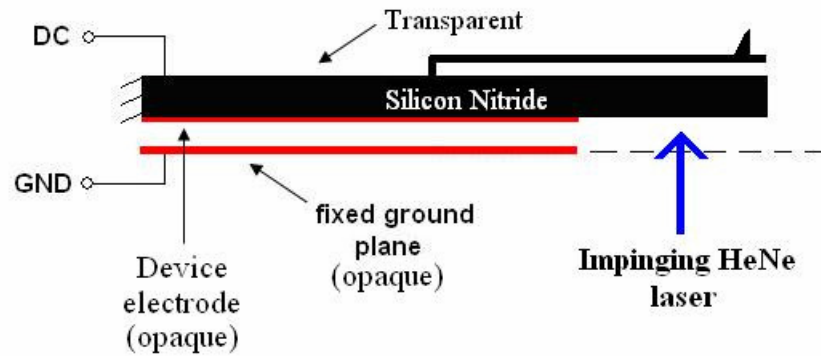


Figure 3.26: Impinging HeNe Laser Schematic

The device electrode (which is normally an opaque metal such as Ti or Cr) cannot span the entire length of the cantilever due to obstruction of the impinging HeNe laser light. According to Equation 3.31 this alteration will reduce the electrostatic force since the surface area of the electrode is decreased, thus increasing the required actuation voltage of the device.

The effective spring constant of this loading case can be determined using the same ANSYS routine used in the previous section (since we have validated its results with closed-form solutions). Table 3.15 lists the effective spring constants for the actuator cantilevers with regards to the partial electrostatic loading scheme.

Table 3.15: Effective Spring Constant for Electrostatic Loading

Loading Scheme	keff (N/m)	W (um)	L (um)	H (um)
electrostatic force	441.7	53.9	92	2.948
	617.7	74.63	92	2.948
	232.8	29.02	92	2.948

Combining Hooke’s law with Equation 3.31 produces an expression for the static deflection of the actuator cantilever due to an applied DC voltage (Equation 3.32).

$$x_{static} = \frac{\epsilon A V_{in}^2}{2k_{eff} g^2} \quad (3.32)$$

We now have a closed-form expression to compare to the ANSYS electrostatic analysis. Table 3.16 illustrates the static deflection of the actuator cantilever due to an applied 200 volts DC, according to Equation 3.32.

Table 3.16: Electrostatic Deflection Resulting from 200 Volts, DC (Closed-Form)

Loading Scheme	keff (N/m)	W (um)	L (um)	H (um)	displacement at 54% of beam length (um)
electrostatic force	441.7	53.9	92	2.948	0.173
	617.7	74.63	92	2.948	0.171
	232.8	29.02	92	2.948	0.177

The device electrode spans approximately 54% of the entire length of the cantilever (see Figure 3.26) therefore the displacements in Table 3.16 represent the static deflection of

the cantilever at 54% of the length. Thus, the free-end displacement of the cantilever will be greater than that seen in Table 3.16.

In ANSYS, a routine was developed in order to model the static deflection of the entire dual cantilever system from electrostatic forcing. The cantilever structures themselves are comprised of SOLID95 elements; these 3-D elements are defined by 20 nodes having three degrees of freedom per node: translations in the nodal x, y, and z directions [27]. The element may have any spatial orientation. SOLID95 has plasticity, creep, stress stiffening, large deflection, and large strain capabilities [27]. The air gap is comprised of SOLID122 elements; a 3-D, 20-node, charge-based electric element that has one degree of freedom, voltage, at each node [27]. This element is applicable to 3-D electrostatic and time-harmonic quasistatic electric field analyses [27]. Similar to the previous ANSYS models, the electrostatic analysis takes an iterative approach by first applying force conditions followed by static conditions; the routine will execute until the output converges to a set precision. The model does not account for fringing fields. Figure 3.27 displays the static deflection of the system due to a 200-volt DC bias.

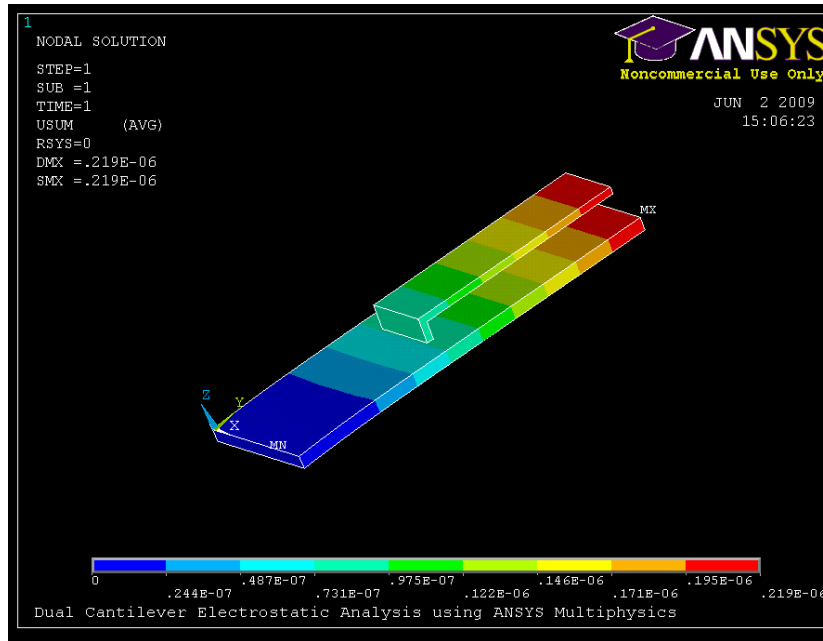


Figure 3.27: ANSYS Electrostatic Displacement

The actuator seen in Figure 3.31 has a width of 29.02 microns, therefore it is expected from Table 2.13 that at 54% of the beam length the displacement will be approximately 0.177 microns. The ANSYS result predicts a displacement of approximately 0.146 to 0.171 microns at 54% of the beam's length. A source of error in this comparison is the extra cantilever in the analysis which adds weight, and consequently stiffness, to the system thus reducing the displacement according to Equation 2.23. Nonetheless, ANSYS provides an accurate illustration of the resulting static displacement due to an applied DC voltage; Table 3.17 shows the free-end displacement of all three cantilever actuators.

Table 3.17: ANSYS Free-End Electrostatic Displacement Resulting from 200 V

Loading Scheme	keff (N/m)	W (um)	L (um)	H (um)	free-end displacement, ANSYS (um)
electrostatic force	441.7	53.9	92	2.948	0.226
	617.7	74.63	92	2.948	0.226
	232.8	29.02	92	2.948	0.219

Similar to the viscous damping analysis, numerous cantilever variations were considered with the aim to reduce actuation voltage. A low actuation voltage (i.e. less than 100 V) is desired in order to reduce the risk of arching; large actuation voltages (i.e. greater than 200 V) increase the risk of spontaneous short-circuit and collapse (discussed in a following section) which is terminal for the device since no passivation layer (insulating oxide) between electrodes exists in the current design. However with the stipulation of mandatory transparency in the laser spot region, the electrode is confined to the stiffest area of the cantilever structure and high electrostatic actuation voltage is unavoidable. Various parameters can be altered in the design but these alterations accompany adverse effects such as increased viscous damping (thus reducing the bandwidth of the structure) or reduced device stiffness. Nonetheless the displacement values found in Table 3.17 are acceptable when imaging smooth to moderate topographies.

The seesaw lever structure was analyzed using the same ANSYS electrostatic coupled-physics approach. Since the lever design was conceived mainly to remedy the high DC bias voltage experienced by the cantilever actuator, it is intuitive that its performance is substantially better. Table 3.18 lists the displacement of the seesaw lever actuators as subject to 100 V DC.

Table 3.18: Electrostatic Deflection of Seesaw Lever Actuators Resulting from 100V

Hinge Length (um)	Hinge width (um)	Width (um)	Length (um)	Thickness (um)	Hinge offset (um) from center	Displacement of sensor end from 100V (um)
Original Seesaw						
10	7	60	150	3	centered	0.539
10	7	40	150	3	centered	0.347
10	7	70	160	3	10	0.471
Seesaw Variation 1						
10	8	40	140	2.5	10	0.588
Seesaw Variation 2						
10	8	40	140	2.5	10	0.406

The benefit in lever design becomes apparent when comparing the electrostatic deflection of each actuator. The seesaw lever consistently displaces twice as much with half of the applied DC bias voltage. A low bias voltage is beneficial when considering such small air gaps since arching is a threat when large voltage potentials are present. Also, low voltage is desired when working with retrofitted AFM systems, eliminating the need for high-voltage power supplies. Both actuators can be operated at voltages under 100V; however the displacement of the cantilever actuator will not exceed that of the current generation FIRAT probes.

3.3 Cantilever Pull-In Voltage Analysis

3.3.1 Theory

Device collapse (otherwise known as pull-in) occurs when the restoring spring force of the device can no longer balance the attractive electrostatic force and the electrodes ‘snap’ together [33]. This is an abrupt phenomenon due to the non-linear

relationship between electrostatic force and device gap as opposed to the linear relationship of spring force with device gap. The most common means of collapse analysis is known as the lumped model wherein the device itself and the electrostatic force are represented as single spring elements (Figure 3.28).

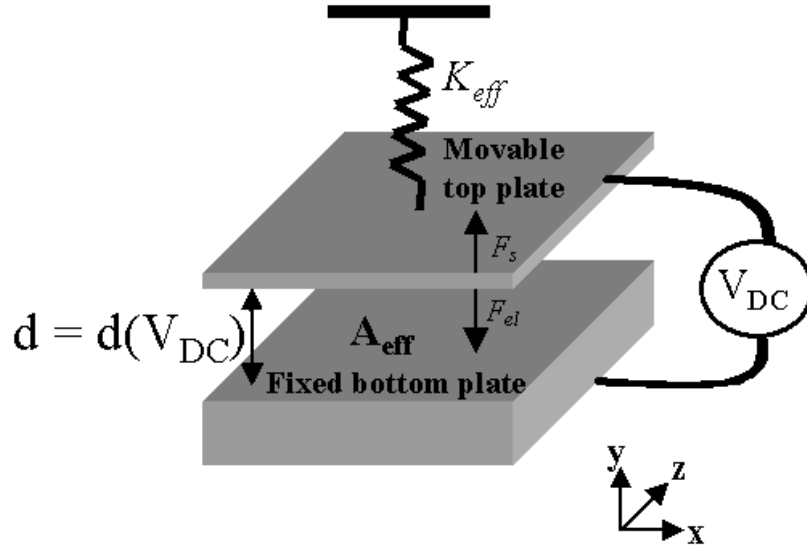


Figure 3.28: Lumped Pull-In Model Schematic [33]

The lumped-model suggests various simplifications that may reduce its accuracy; deformation of the movable plate (or cantilever beam in our case) cannot exactly be represented by one lumped spring element due to non-linearity. Also, fringing fields may drastically affect the pull-in characteristics if the device gap is comparable to the device dimensions. Equation 3.33 provides an expression for the pull-in voltage based on the balance of spring restoring forces and electrostatic attraction forces [33].

$$V_{PI} = \sqrt{\frac{8k_{eff}d_0^3}{27\epsilon_0A_{eff}}} \quad (3.33)$$

Similar to the nomenclature of previous sections, k_{eff} represents the effective mechanical spring constant of the device, ϵ_0 represents the permittivity of free space, and A_{eff} represents the effective area of the electrodes. The air gap at zero DC voltage is represented by d_0 . As a rough estimate, the device will experience pull-in when the maximum displacement of the cantilever or bridge is equal to one-third of the original air gap. In this work we will consider two different pull-in analyses, namely the work presented by Pamidighantam, et al. and Chowdhury, et al.

3.3.2 Lumped Parameter Model

The work presented in [33] relies on the lumped parameter model discussed in the Theory section. In order to produce more accurate results, the model has incorporated phenomena such as partial electrode configuration, axial stress, non-linear stiffening and fringing fields. The closed-form solution (Equation 3.34) as proposed by [33] includes an effective cantilever beam width (see Equation 3.35).

$$V_{PI} = \sqrt{\frac{8k_{eff}d_0^3}{18.2\epsilon_0lb_{eff}}} \quad (3.34)$$

$$b_{eff} = b \left(1 + 0.65 \frac{(1-\beta)d_0}{b} \right) \quad (3.35)$$

The β value denotes the measure of normalized maximum deflection (y_{max}) of the cantilever beam with respect to the original air gap, or $\beta = y_{max} / d_0$. As previously mentioned, the device is expected to collapse when the free-end of the cantilever beam reaches a displacement of one-third of the original air gap, therefore β is approximately 0.33. The effective spring constant has been determined from previous analyses but [33] proposes an expression (Equation 3.36) that incorporates an adjusted elastic modulus, \hat{E} .

$$k_{eff} = \frac{2\hat{E}bh^3}{3l^3} \left[\frac{3}{8 - 6\lambda_r + \lambda_r^3} \right] \quad (3.36)$$

The term λ_r represents the percentage of the length of the beam that is under electrostatic loading; in our case for simplification we will assume the whole beam is under electrostatic force and $\lambda_r = 1$. The final expression for pull-in voltage can now be seen as Equation 3.37 where equivalent elastic modulus and width are included.

$$V_{PI} = \sqrt{\frac{8 \frac{E(1-\nu^2)^{-1}bh^3}{l^3} d_0^3}{18.2\varepsilon_0 lb \left(1 + 0.65 \frac{(1-0.33)d_0}{b} \right)}} \quad (3.37)$$

The elastic modulus, ν , for Silicon Nitride is approximately 0.24. Equation 3.37 can be plotted as a function of beam width in order to estimate the pull-in voltage for the cantilever beam actuators considered in this work (Figure 3.29).

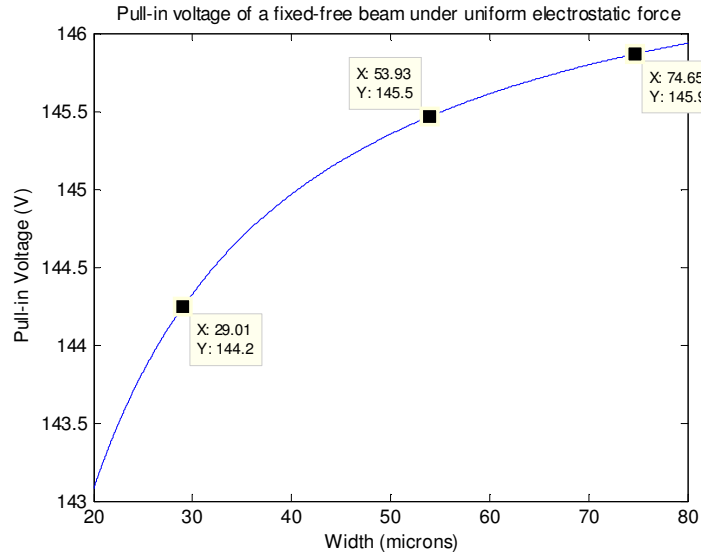


Figure 3.29: Pull-In Voltage for Lumped Parameter Model

On average the expected pull-in voltage is approximately 145 volts. This is a lower bound estimate because the electrostatic force on the actuator beam is not uniform and thus k_{eff} increases significantly.

3.3.3 Linearized Uniform Approximate Model

Similar to the work presented in [33], Chowdhury, et al. suggest a linear approximation method that accounts for non-linearities during electrostatic deflection. Figure 3.30 is a schematic of the pull-in phenomenon as it applies to micro-cantilevers [34].

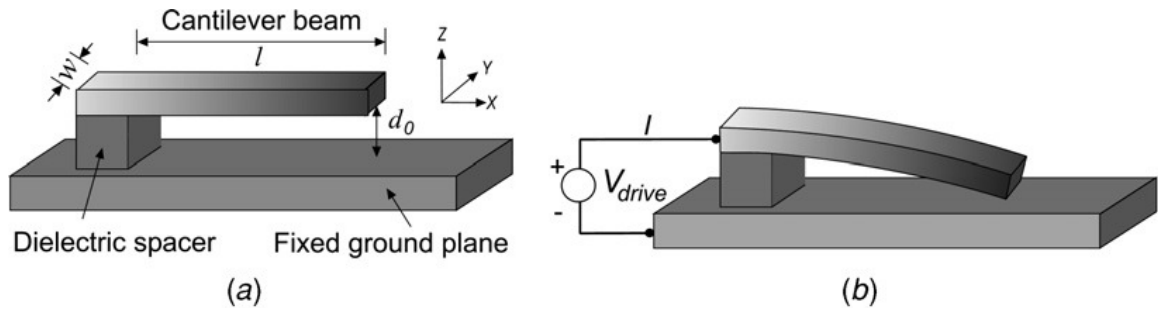


Figure 3.30: (a) Micro-Cantilever at Rest and (b) a Collapsed Micro-Cantilever

To keep consistent with the notation in the previous section, the width of the beam will still be denoted by b , even though it is pictured as w in Figure 3.30. It is worthy to note that cantilever beams which possess a width much greater than d_0 are less affected by fringing field effects while for narrow cantilever beams this effect could increase capacitance by up to a factor of 3 [34]. Equation 3.38 is an expression for pull-in voltage as presented by [34].

$$V_{PI} = \sqrt{\frac{2\hat{E}h^3d_0}{8.37\varepsilon_0l^4\left(\frac{5}{6d_0^2} + \frac{0.19}{d_0^{1.25}b^{0.75}} + \frac{0.19}{d_0^{1.25}l^{0.75}} + \frac{0.4h^{0.5}}{d_0^{1.5}b}\right)}} \quad (3.38)$$

Again, since all parameters are known / constant we can plot Equation 3.6 with respect to a varying beam width (Figure 3.31). Also included in Figure 3.31 is the previous method proposed by [33].

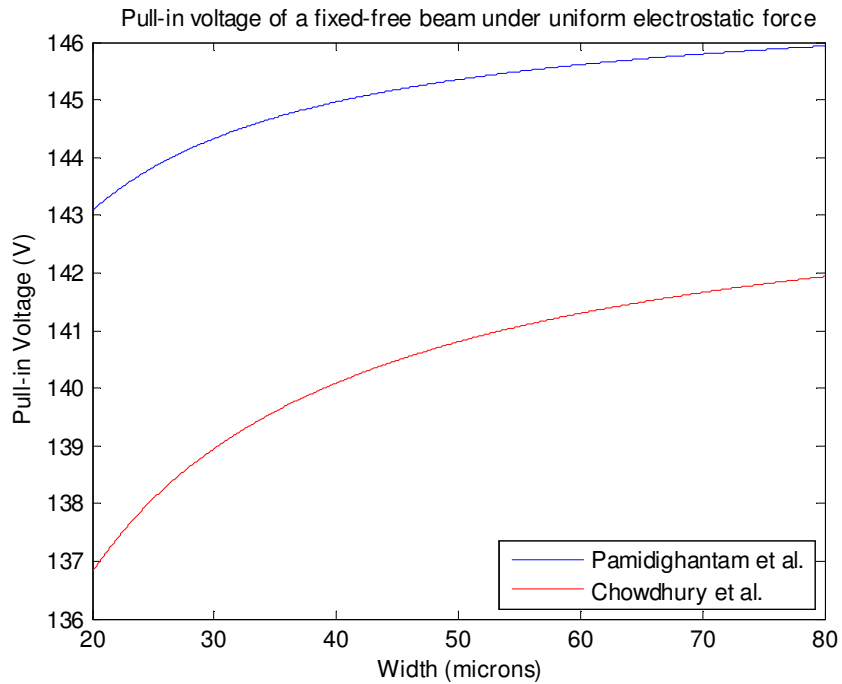


Figure 3.31: Comparison of Pull-In Voltage Estimation Methods

The latter method predicts a lower collapse voltage but the non-linearity in both curves appears to be consistent. The error in agreement between the two methods is perhaps attributed to the type of micro-cantilever under analysis. The approach presented in [33] is more geared towards the compensation of several non-ideal effects experienced by the micro-cantilever under electrostatic force. The approach presented in [34] concentrates

heavily on fringing field effects which are perhaps not as critical when considering the micro-cantilevers used in this work. However, the two methods provide a range of voltages in which the actuator cantilever may experience catastrophic collapse and thus an applied DC bias of 130 to 140 volts should be regarded as a cautionary threshold.

CHAPTER 4:

COUPLED SYSTEM ANALYSES

4.1 ANSYS Harmonic Analysis

It is very important to study the behavior of the coupled system's response to a harmonic excitation. In this section, various device combinations are subject to a one-micronewton point load in ANSYS, simulating the harmonic tapping of the sensor's sharp tip on a sample. The undamped frequency response can thus be obtained; if multiple in-line points are examined on the FEA model, the mode shapes can also be extracted. The harmonic analysis will be executed for the three device combinations: cantilever-on-cantilever, cantilever-on-seesaw lever, and bridge-on-cantilever. There are variations in size of each combination; however knowledge of one provides the general behavior of that specific system.

4.1.1 Cantilever-on-Cantilever

The frequency response characteristics of each cantilever, bridge, and seesaw lever have been evaluated separately; this will provide some insight into the interpretation of the coupled system response. Figure 4.1 is the FEA model of the cantilever-on-cantilever combination in which a point-load is applied at the tip of the sensor cantilever. According to the coordinate axes, all nodes at $Y = 0$ will have zero displacement to simulate a fixed (clamped) boundary condition.

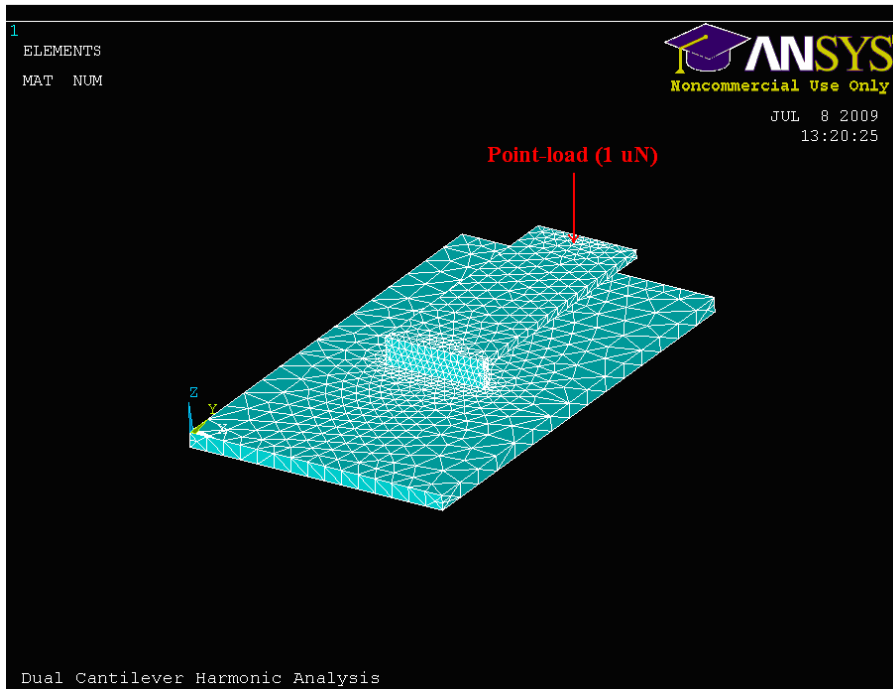


Figure 4.1: Cantilever-on-Cantilever FEA Model

The harmonic analysis sweeps a user-defined frequency range, in this case zero to one megahertz; this range is broad enough to capture the behavior of the fundamental resonance modes of each separate structure. The harmonic analysis is expected to produce coupled system resonances identical or close-to those determined in the modal analysis. The purpose of this analysis is to observe the displacement behavior of each structure at these resonance frequencies, as well as their displacement relative to one another. Figure 4.2 illustrates the path of nodes that are considered in this harmonic analysis. A path along the entire sensor length is necessary to capture the entire mode shape of the cantilever; at the same time it is necessary to view the displacement of the actuator segment beneath the sensor such that relative displacement can be obtained.

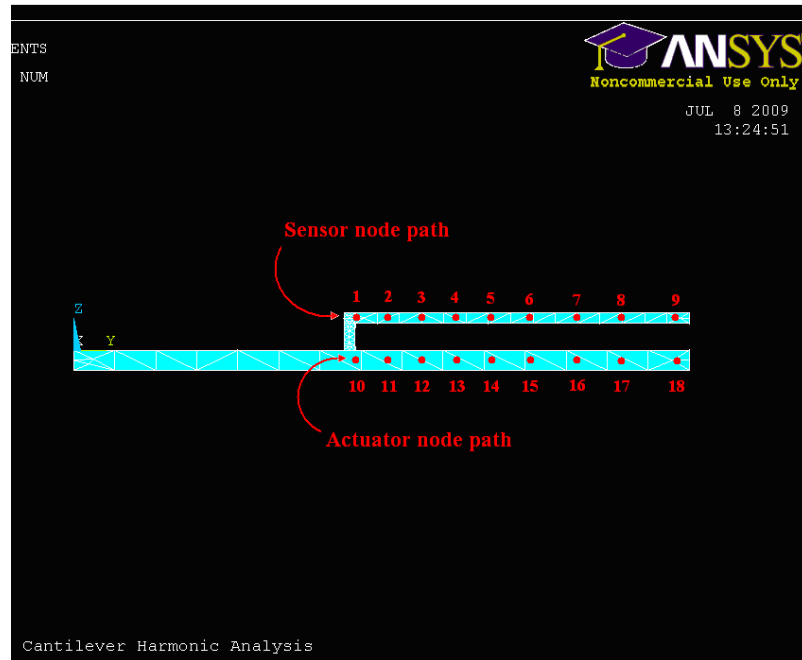


Figure 4.2: Actuator and Sensor Node Paths

A unique frequency response can be obtained for each node; the nine responses for each structure (sensor and actuator) can be positioned next to each other such that a mode shape becomes apparent (Figures 1.3 and 1.4). Note from Figure 4.2 that nodes 1 through 9 correspond to the sensor while nodes 10 through 18 correspond to the actuator. The cantilever actuator in Figure 4.1 has a width, length, and thickness of 54 microns, 92 microns, and 3 microns, respectively; the cantilever sensor has a width, length, and thickness of 50 microns, 31 microns, and 1.6 microns, respectively. From the cantilever sensor length it can be inferred that each node is spaced approximately 6.25 microns apart. These specific dimensions will be used throughout the cantilever-on-cantilever harmonic analysis example in this section.

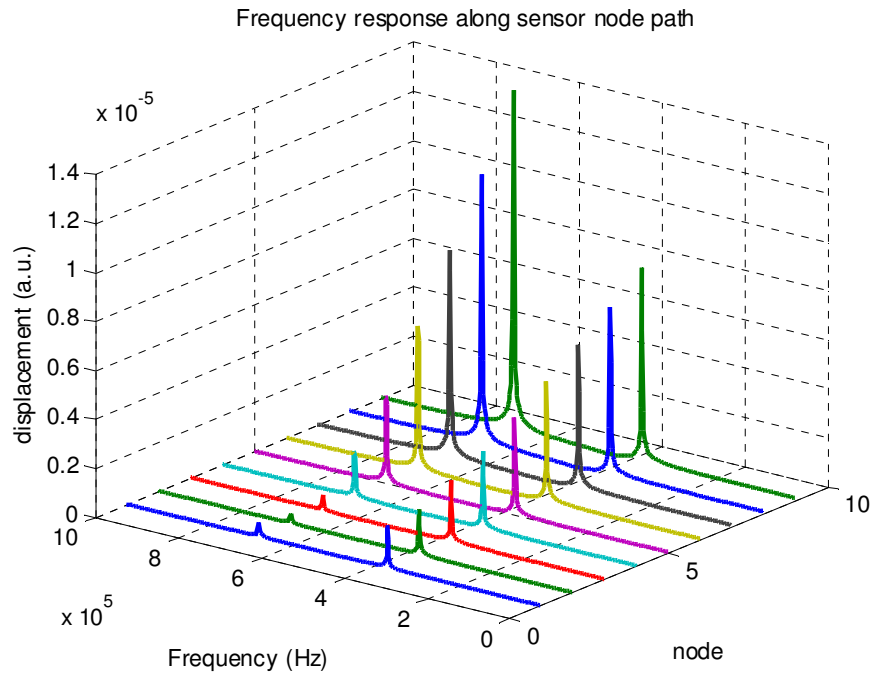


Figure 4.3: Frequency Response along Cantilever Sensor Node Path

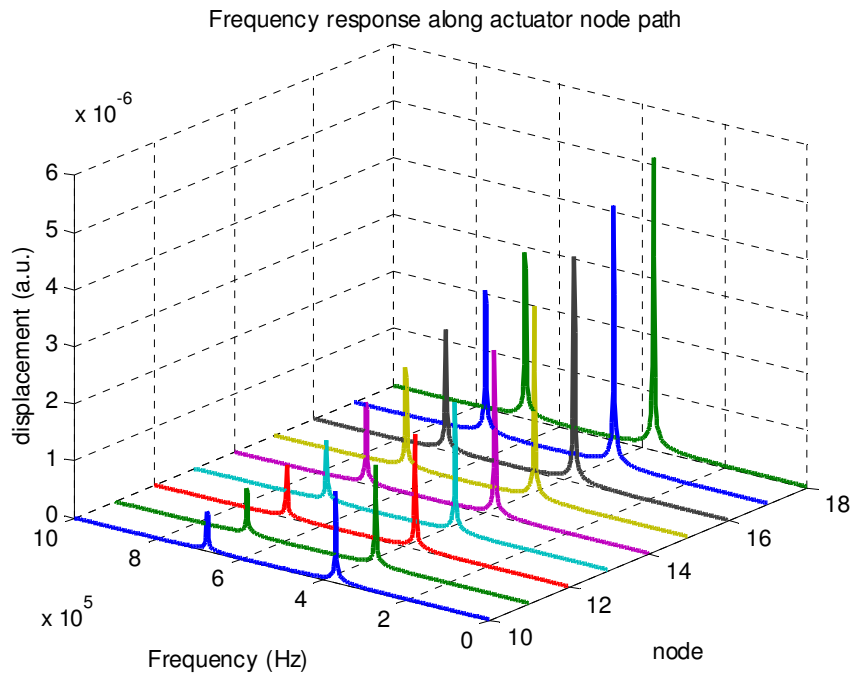


Figure 4.4: Frequency Response along Cantilever Actuator Node Path

According to the plots, the first two modes of the system occur at approximately 372 kHz and 682 kHz. This is expected since these specific actuator and sensor cantilevers have fundamental resonances of 400 kHz and 750 kHz, respectively. In the case of a coupled system, the independently calculated resonance frequencies will shift due to mass loading and consequent stiffness changes. Using a peak-finding program in MATLAB, the mode shapes were extracted in order to display the relative displacement of the sensor and actuator cantilevers. Figure 4.5 illustrates the relative displacement in arbitrary units (a.u.) as a function of the sensor node path (nodes 1 through 9).

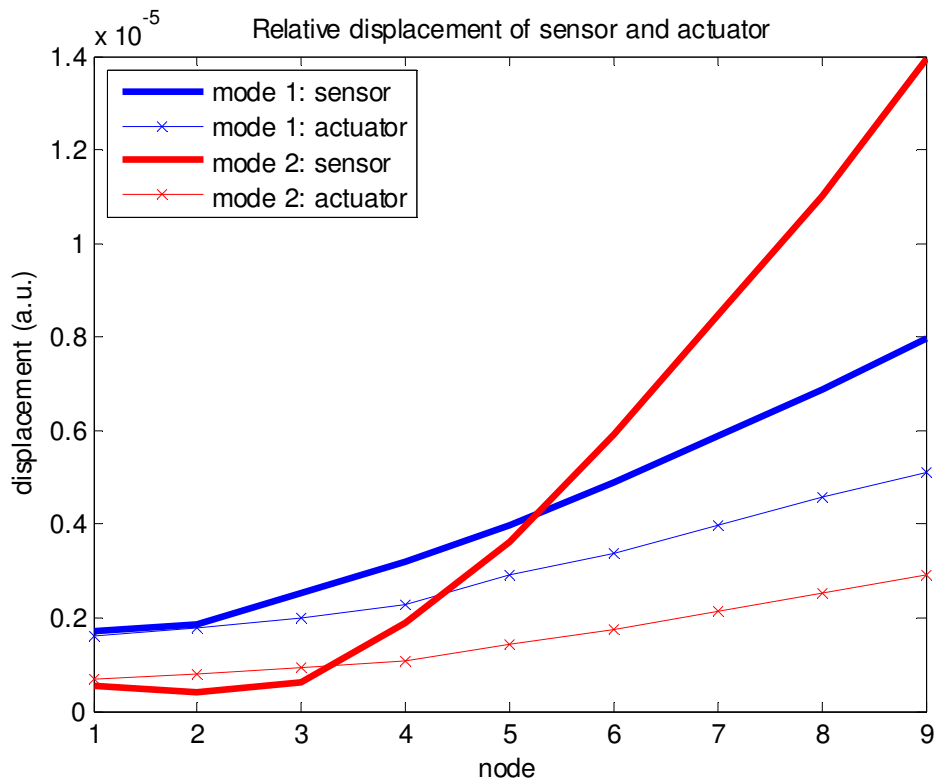


Figure 4.5: Relative Displacement of Sensor and Actuator

The displacement of the sensor relative to the actuator is greatest when the system is harmonically excited at the second mode, or ~ 682 kHz; this frequency is essentially the fundamental resonance mode of the sensor cantilever. Figure 4.5 displays the ideal behavior of the system; the relative displacement should not be significant until the second mode of the system, so as not to contribute to noise within the actuation bandwidth. Figure 4.6 is a comparison of the system at each modal frequency; note the displacement of each cantilever at their respective fundamental resonance frequencies.

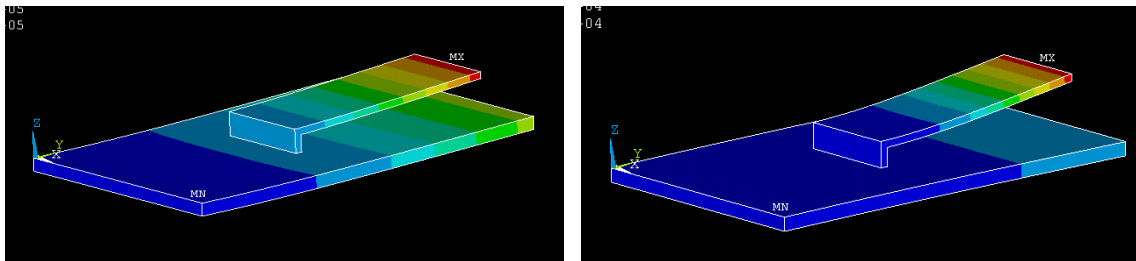


Figure 4.6: Modal Displacements, Left) 372 kHz and Right) 682 kHz

Again, this behavior is ideal since the latter of the resonance modes will be used for sample-tapping, thus the actuator should not significantly displace in relation to the sensor. As a reference, the blue color in the FEA model represents little or no displacement while red represents the maximum displacement.

4.1.2 Cantilever-on-Seesaw Lever

The same harmonic analysis parameters apply to the cantilever-on-seesaw lever system. The FEA model can be seen in Figure 4.7; the same node paths for the sensor and actuator were used in this case as well. This specific system has seesaw lever actuator dimensions as seen in Table 3.6, variation 1, while the cantilever sensor has a

width, length, and thickness of 16 microns, 50 microns, and 1.6 microns, respectively. The nodes are therefore spaced approximately 6.25 microns apart.

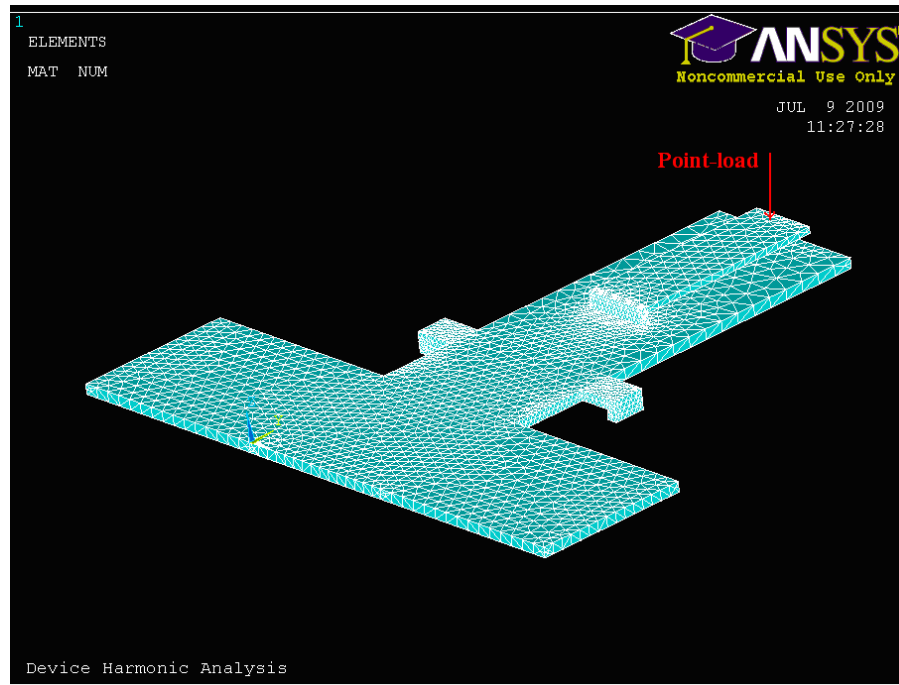


Figure 4.7: Cantilever-on-Seesaw Lever FEA Model

From the analyses in the previous sections it is expected that the coupled system exhibits two resonance peaks, one at the fundamental resonance of the seesaw lever (~ 244 kHz) and one at the fundamental resonance of the cantilever sensor (~750 kHz). Figures 1.8 and 1.9 are the frequency response plots from the node paths of each structure. Surprisingly a third mode is apparent at approximately 390 kHz; this mode is likely due to the coupling of the structures. According to further modal analysis, this mode corresponds to the flapping motion of the seesaw lever actuator. The first mode of the system occurs at an expected 220 kHz while the third mode occurs at approximately 750 kHz.

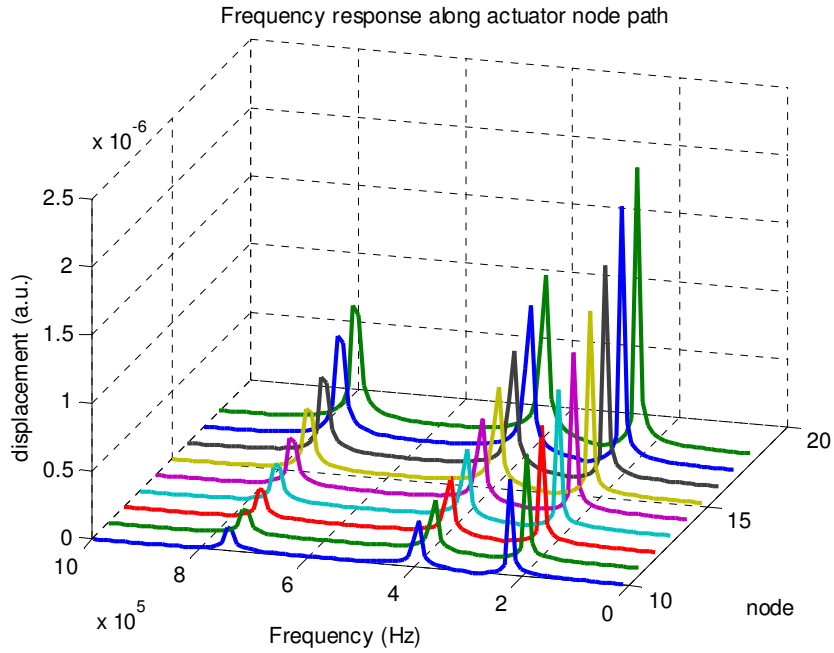


Figure 4.8: Frequency Response along Seesaw Lever Actuator Node Path

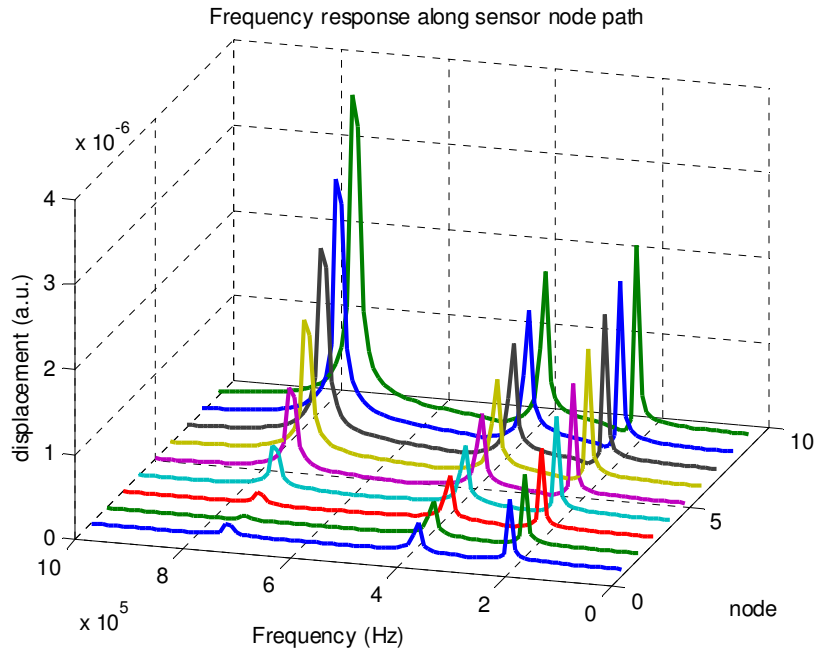


Figure 4.9: Frequency Response along Cantilever Sensor Node Path

From the relative displacement plot (Figure 4.10) the third mode exhibits the greatest displacement of the cantilever sensor; this behavior is once again ideal since the tapping motion will occur at the fundamental resonance frequency of the sensor cantilever, or in this case the third mode of the system.

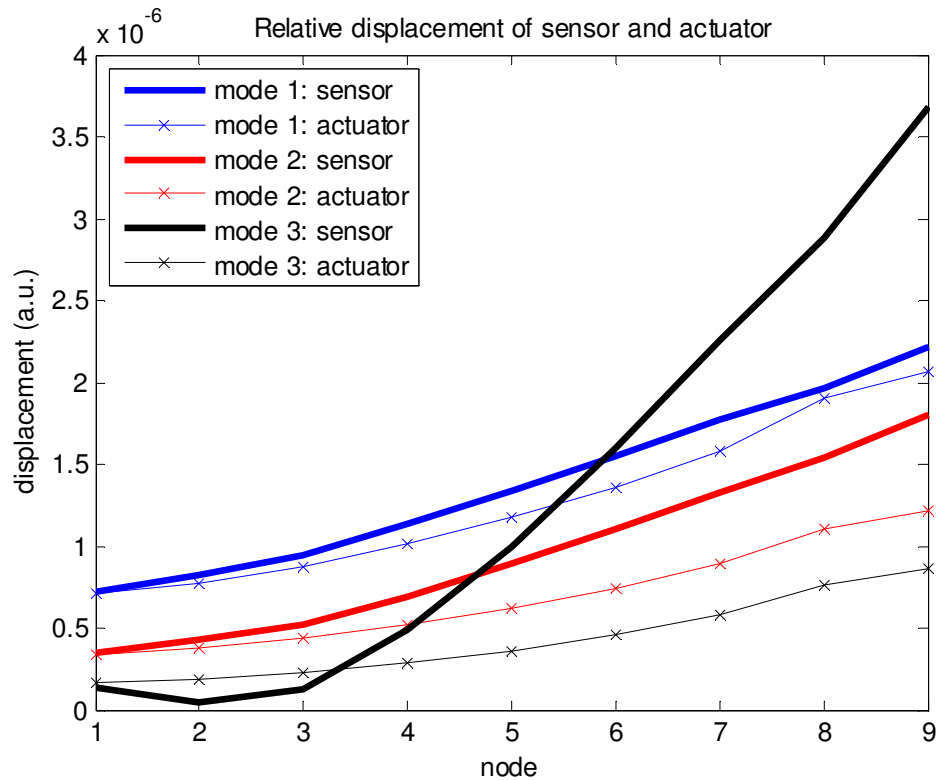


Figure 4.10: Relative Displacement of Sensor and Actuator at System Resonance Modes

It is once again important to view the displaced structure at the system modal frequencies.

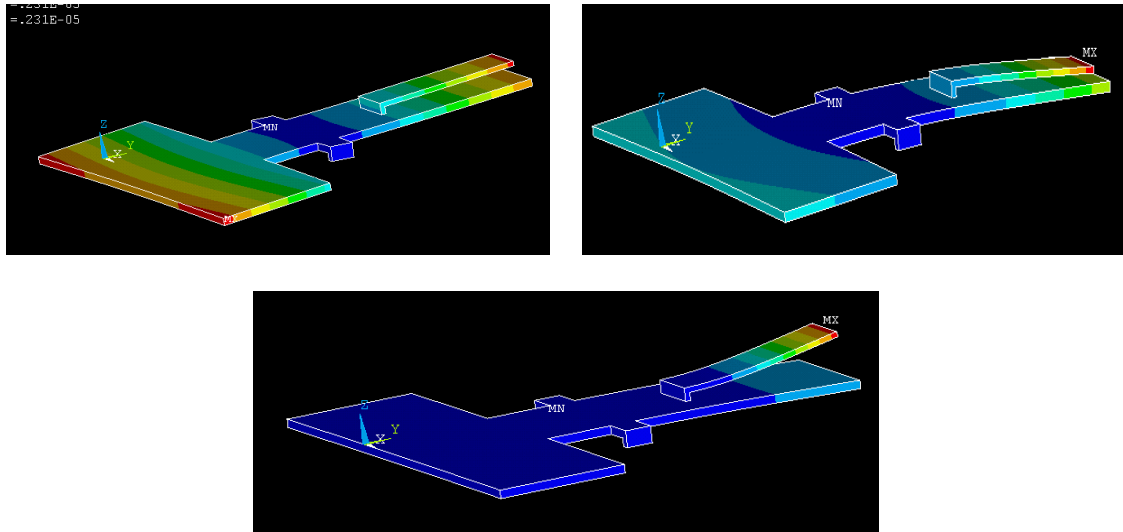


Figure 4.11: Modal Displacements, (Top Left) ~ 220 kHz, (Top Right) ~ 390 kHz, and (Bottom) ~750 kHz

At 750 kHz the seesaw lever actuator remains relatively stiff while the sensor cantilever is free to oscillate with the preferred motion for sample-tapping (Figure 4.11). At 220 kHz the system exhibits the “seesaw” mode.

4.1.3 Bridge-on-Cantilever

Since the fundamental resonance frequencies of the bridge sensors considered in this work occur outside of the user-defined frequency range, the range has been extended from 0 to 1.5 MHz. This specific harmonic analysis has a cantilever actuator with length, width, and thickness of 92 microns, 75 microns, and 3 microns, respectively. The bridge sensor has a length, width, and thickness of 50 microns, 20 microns, and 0.4 microns, respectively; the nodes are spaced approximately 6.25 microns apart. Since the bridge sensor experiences maximum displacement at the center of the beam, the sensor is positioned sideways (Figure 4.12) in order to utilize the maximum free-end displacement

of the cantilever actuator. The one Newton point-load is thus subject to the center of the beam, as well.

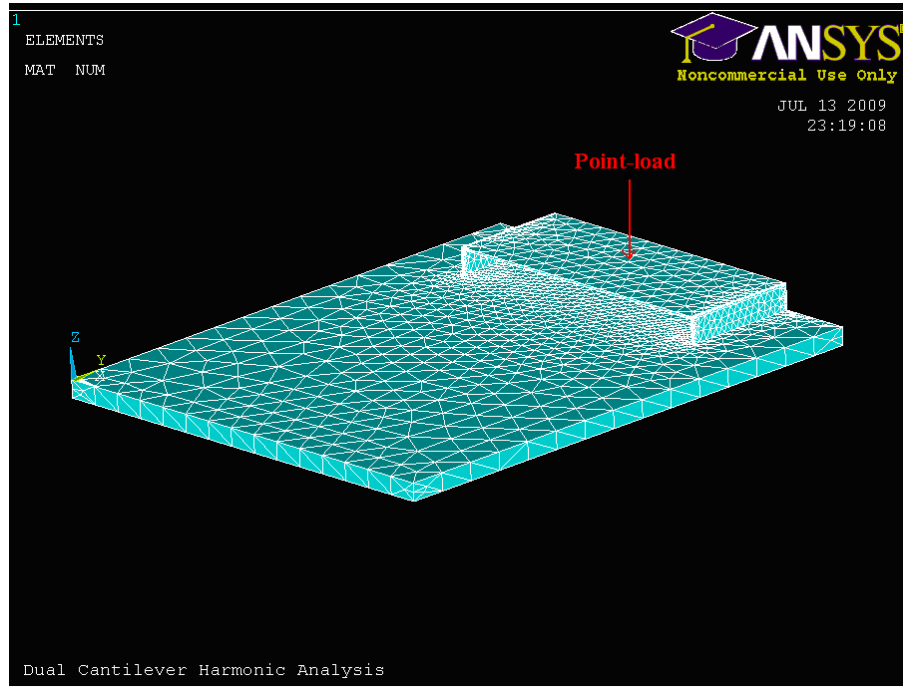


Figure 4.12: Bridge-on-Cantilever FEA Model

Since the sensor is positioned differently than the previous analyses, this requires the sensor and actuator node paths to change accordingly (Figure 4.13). The cantilever actuator is expected to exhibit minimal deformation during both system modes since significant anticlastic curvature does not take place until higher modal frequencies.

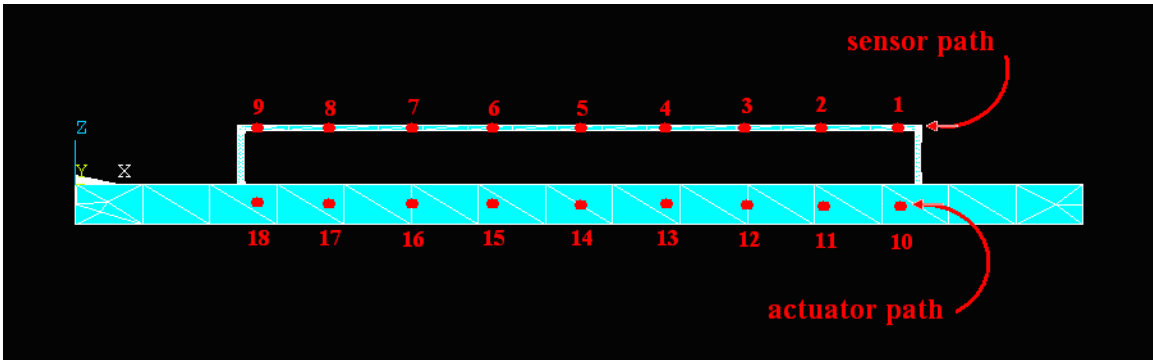


Figure 4.13: Sensor and Actuator Node Paths

Notice the position of the axes origin in Figure 4.13, this suggests that we are viewing the structure from the front and looking towards the clamped-end of the actuator. From the simulation, it appears that the modes occur very close to their predicted frequencies; this is perhaps due to the insignificant mass of the bridge sensor since it is substantially thinner than the cantilever sensor. Figures 1.14 and 1.15 reveal system modes at approximately 405 kHz and 1.17 MHz.

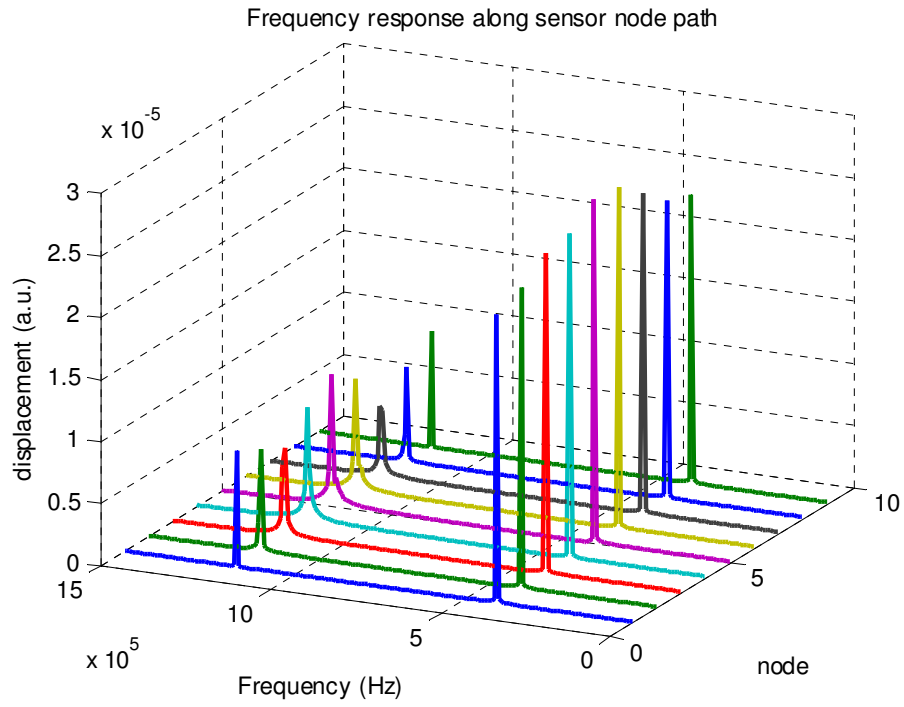


Figure 4.14: Frequency Response along Bridge Sensor Node Path

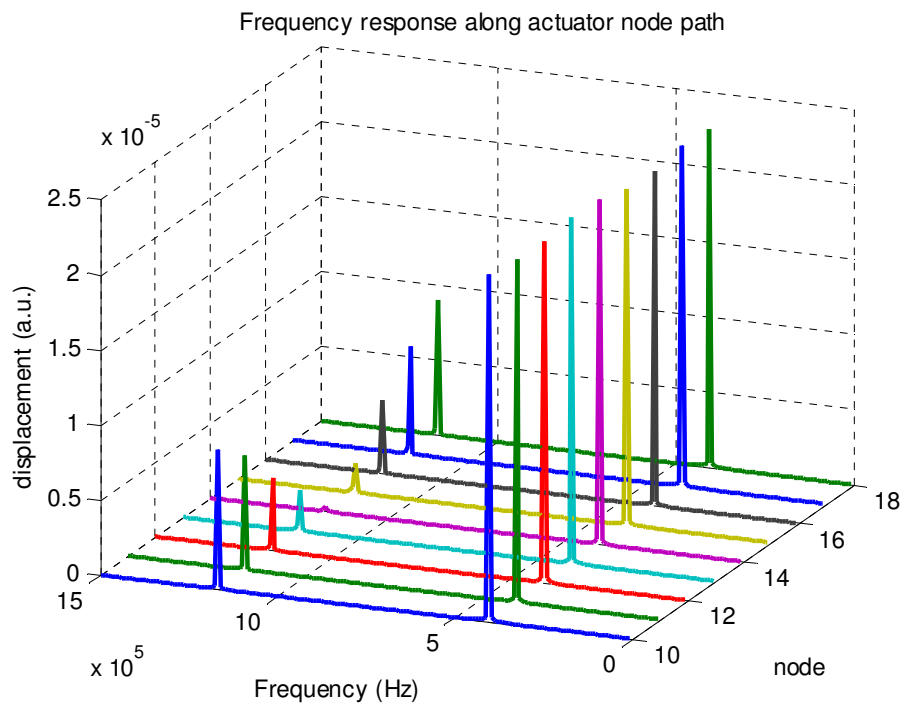


Figure 4.15: Frequency Response along Cantilever Actuator Node Path

Symmetry can be observed along the node path of each structure. Anticlastic curvature is noticeable in the second mode of the system for the cantilever actuator; during the first mode this curvature is non-existent. Figure 4.16 is a plot of relative displacement in arbitrary units.

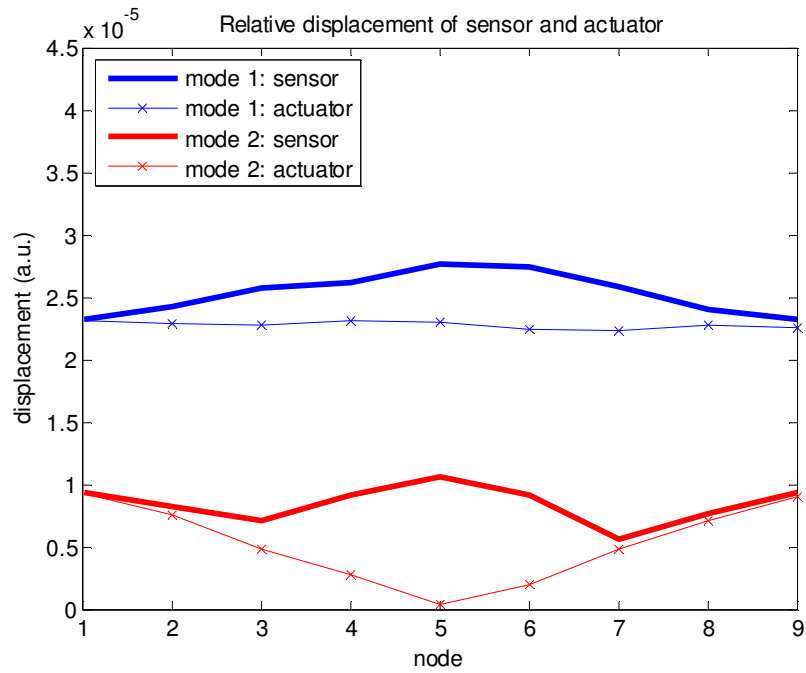


Figure 4.16: Bridge-on-Cantilever Relative Displacement

Finally, in order to gage the intensity of oscillation at the modal frequencies, we can look at the contour plot of the deformed system (Figure 4.17).

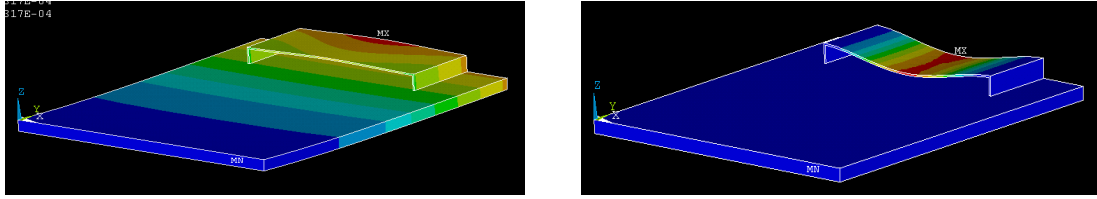


Figure 4.17: Modal Displacements, Left) ~ 405 kHz and Right) ~ 1.17 MHz

The rightmost mode shape in Figure 4.17 reveals that the cantilever actuator is very stiff at the bridge sensor's fundamental resonance frequency; once again this is ideal behavior for sample tapping.

4.2 Component Mode Synthesis

Complementary to the finite element method, component mode synthesis [35] (CMS, first realized by Hurty in the 1960's [36]) attempts to analyze multi-component structures on a large-scale basis. The aim of CMS is to define each component separately and ultimately constrain the components to work as a single structure [35]. Computational power and time are directly related to the degrees of freedom one specifies in the modeling of the system. In this sense, CMS exhibits great advantages due to its drastically reduced degree-of-freedom model. Generally, a finite element model consists of hundreds of elements and thus several hundred degrees of freedom which are necessary in order to achieve accurate results that converge within a specified range. The CMS approach displays accurate results from a very limited degree-of-freedom system. This is a beneficial approach considering one of the simple systems discussed in this work; a fixed-free large cantilever with an attached smaller cantilever (Figure 4.18). The system thus consists of two components that will each be analyzed as undamped Euler-

Bernoulli beams; the smaller cantilever is assumed to be fixed-free with relaxed transverse and rotational motion at the fixed boundary (also considered the interface in this case).

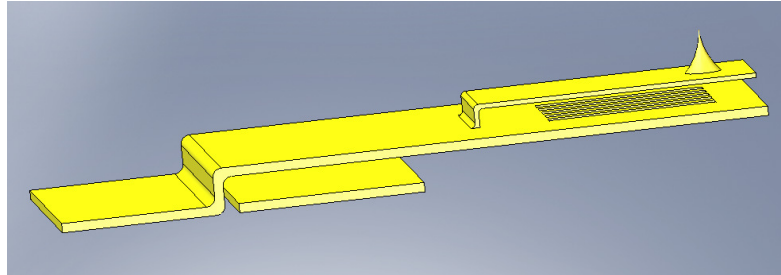


Figure 4.18: Dual Cantilever Schematic

Justification for the Euler-Bernoulli beam method:

- Small angle displacement of each cantilever, thus the cross-section of each beam stays orthogonal to its respective neutral axis (Timoshenko beam theory compensates for non-orthogonal displacement of the cross-section).
- The length and width of the beams are relatively large in relation to their thicknesses (stubby beams are best analyzed using the Timoshenko beam theory).
- Anticlastic curvature negligible

Closed-form eigenfunctions are readily available for fixed-free cantilever beams [35].

The goal of the analysis is to accurately predict the first five undamped eigenfrequencies of the system as well as produce accurate mode shapes of the combined cantilever system.

4.2.1 Euler-Bernoulli Analysis

As previously mentioned, each beam structure in the CMS of the system will be analyzed using the Euler-Bernoulli method. This is a valid means of analysis due to the relative dimensions of each cantilever (long and slender). Each cantilever assumes very small angles of deflection and therefore the Timoshenko beam theory is not utilized. To begin, consider a fixed-free cantilever beam as seen in Figure 4.19. The field Equation is therefore expressed as Equation 4.1 and has matching boundary conditions as seen in Equations 4.3 and 4.4.

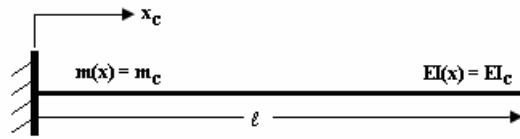


Figure 4.19: Schematic of a Fixed-Free Cantilever

$$m(x) \frac{\partial^2 w(x, t)}{\partial t^2} = - \frac{\partial^2}{\partial x^2} (EI(x) \frac{\partial^2 w(x, t)}{\partial x^2}) \quad (4.1)$$

$$w(0, t) = 0 \quad ; \quad \frac{\partial w(0, t)}{\partial x} = 0 \quad (4.2)$$

$$-EI(x) \frac{\partial^2 w(l, t)}{\partial x^2} = 0 \quad ; \quad EI(x) \frac{\partial^3 w(l, t)}{\partial x^3} = 0 \quad (4.3)$$

Equation 4.2 and 4.3 yield the geometric and natural boundary conditions, respectively. In Equation 4.2, the left expression represents zero-displacement while the right expression represents zero-slope. In Equation 4.3, the left-expression represents zero

shear force while the right-expression represents zero bending moment. From Figure 4.2 we deduce that the cantilever is of length ℓ and assumed to be uniform where:

- $m \rightarrow$ mass per unit length
- $E \rightarrow$ Elastic modulus
- $I \rightarrow$ Area moment of inertia

The subscript “c” makes the quantities component-specific (either 1 for the large cantilever or 2 for the small). By separation of variables, it is possible to solve the boundary value problem and achieve a workable characteristic equation (Equation 4.4).

Using MATLAB to solve Equation 4.4 produces the natural frequencies.

$$\alpha^3 \left\{ \sin \alpha - \sinh \alpha + \left(\frac{\cos \alpha + \cosh \alpha}{\sin \alpha + \sinh \alpha} \right) (\cos \alpha + \cosh \alpha) \right\} = 0 \quad (4.4)$$

Where $\alpha^3 = \beta^3 \ell^3$ and $\beta^4 = \frac{m\omega^2}{EI}$. The solved characteristic equation produces α values of 1.8751, 4.6941, 7.8548, 10.9955, ... , α_n . For this analysis, we will consider an arbitrary number of normal modes; better convergence of the final eigenfrequencies occurs when there are more normal modes present in the analysis. The transcendental Equation 4.4 exhibits asymptotic behavior at higher values of α_n , thus Equation 4.5 is an acceptable approximation for α_n . The natural frequencies can be expressed as Equation 4.6.

$$\alpha_n \cong (2n - 1) \frac{\pi}{2} \quad (4.5)$$

$$\omega_n = \beta_n \sqrt{\frac{EI}{m\ell^4}} = \frac{\alpha_n}{\ell} \sqrt{\frac{EI}{m\ell^4}} = \frac{\alpha_n}{\ell^3} \sqrt{\frac{EI}{m}} \rightarrow n = 1, 2, 3, 4 \quad (4.6)$$

It is noteworthy that Equation 4.5 can produce values of α_n with four-decimal-place precision (based on the solutions of Equation 4.4). The general solution to the field equation can finally be obtained on a mode-to-mode basis (Equation 4.7). These solutions, or eigenfunctions, predict the normal mode shapes of the fixed-free cantilever beam.

$$\varphi_n(x) = A_n \left\{ \left(\frac{\cosh \beta_n l + \cos \beta_n l}{\sinh \beta_n l + \sin \beta_n l} \right) (\sinh \beta_n x - \sin \beta_n x) \right\} \quad (4.7)$$

Since Equation 4.7 cannot be normalized explicitly, we will assume a value of one for all A_n .

4.2.2 Rigid Body and Constraint Modes

The remaining modes to consider consist of rigid body and constraint modes. For the larger cantilever, since it is assumed to be rigidly fixed at the left end, rigid body modes are not necessary. Constraint modes in this case are also unnecessary since the larger cantilever is assumed to move independently of the smaller cantilever. However this is not the case for the smaller cantilever as its motion depends partly upon the motion of the larger cantilever. We will assume rigid body transverse (superscript w) and rigid body rotational (superscript θ) modes for the smaller cantilever to be $\varphi_1^w = 1$ and $\varphi_2^\theta = x_2$, respectively. Equations 4.8 (transverse, w) and 4.9 (rotational, θ) describe the constraint modes associated with relaxing the “fixed” boundary condition of the smaller cantilever [37]. This must be so in order to later assemble the two components into one system.

$$\varphi_2^w(x_2) = 3 \frac{(l_2 - x_2)^2}{l_2^2} - 2 \frac{(l_2 - x_2)^3}{l_2^3} \quad (4.8)$$

$$\dots \text{where } \varphi_2^w(0) = 1 ; \frac{d\varphi_2^w(0)}{dx} = 0$$

$$\varphi_2^\theta(x_2) = l_2 \left\{ - \left[\frac{(l_2 - x_2)^2}{l_2^2} \right] + \frac{(l_2 - x_2)^3}{l_2^3} \right\} \quad (4.9)$$

$$\dots \text{where } \varphi_2^\theta(0) = 0 ; \frac{d\varphi_2^\theta(0)}{dx} = -1$$

Again, the subscript “2” denotes expressions or values pertaining to the smaller cantilever while “1” is for the larger cantilever. It should be noted that either rigid body modes or constraint modes can be used and that the use of both sets presents some level of redundancy.

4.2.3 Assemblage of Modes

Finally, we can arrive at the matrix notation of the eigenfunctions for each cantilever. As seen in Equation 4.10, each matrix consists of n normal mode eigenfunctions, two rigid body modes and two constraint modes. Since the larger cantilever does not possess the latter of the two sets of modes, it will remain as an n -by-1 matrix of normal modes. For the smaller cantilever these last two sets will be non-zero, as previously explained.

$$\Phi_1^T = \left| \Phi_1^N \right| ; \Phi_2^T = \left| \Phi_2^N \quad \Phi_2^R \quad \Phi_2^C \right| \quad (4.10)$$

The superscripts N, R and C denote Normal, Rigid and Constraint modes, respectively (superscript T refers to the transpose of a matrix). The total response for each separate cantilever can thus be expressed as Equations 4.11 and 4.12.

$$w_1(x_1, t) = \Phi_1^T \mathbf{a} \quad (4.11) \quad ; \quad w_2(x_2, t) = \Phi_2^T \mathbf{b} \quad (4.12)$$

Vectors \mathbf{a} and \mathbf{b} represent the modal coordinates; i.e., $\mathbf{a}^T = [a_1 \dots a_n]$ and $\mathbf{b}^T = [b_1 \dots b_{n+4}]$.

4.2.4 Energy Contributions

Each component in the CMS of the system will contribute a mass and stiffness matrix to the disjoint set of equations. The term ‘disjoint’ refers to the fact that the components have not yet been assembled, or rather they are in the pre-combined state. In order to obtain these components, we must consider the kinetic and potential energy contributions of each. The mass matrix, \mathbf{M}_c , arises from computing the kinetic energy contribution (Equation 4.13) while the stiffness matrix, \mathbf{K}_c , arises from the potential energy contribution (Equation 4.14).

$$T_c = \frac{1}{2} \int_0^{l_c} m_c \dot{w}_c^2 dx \quad (4.13)$$

$$\therefore \mathbf{M}_c = \int_0^{l_c} m_c \boldsymbol{\phi}_c^T \boldsymbol{\phi}_c dx \quad c = 1, 2$$

$$V_c = \frac{1}{2} [w_c, w_c] \quad (4.14)$$

$$\therefore \mathbf{K}_c = [\boldsymbol{\phi}_c^T, \boldsymbol{\phi}_c] \quad c = 1, 2$$

The computation of the stiffness matrix in each case involves the energy inner-product. The purpose of the energy inner-product is to capture the total potential energy contribution from each component, which includes strain energy and the work done at the boundaries. The energy inner-product arises from a double integration-by-parts of the inner-product since the system is of the order $p = 2$. The final expression is seen in Equation 4.15.

$$[\boldsymbol{\varphi}_c^T, \boldsymbol{\varphi}_c] = \int_0^{l_c} EI \frac{d^2 \boldsymbol{\varphi}_c^T}{dx^2} \frac{d^2 \boldsymbol{\varphi}_c}{dx^2} dx = \mathbf{K}_c \quad c = 1, 2 \quad (4.15)$$

Trailing terms from Equation 4.15 were eliminated using the original boundary conditions specified in Equations 4.2 and 4.3. We now have the pieces necessary to express each component as Equation 4.16. From these expressions (total of two), we can assemble a disjoint set of equations that can eventually be linked (or combined) using the interface conditions of the two cantilevers.

$$\mathbf{M}_c \ddot{\boldsymbol{\xi}} + \mathbf{K}_c \boldsymbol{\xi} = \mathbf{Z}_c \quad (4.16)$$

Since we are only concerned with the modal analysis of the system, we can disregard the external forcing matrix, \mathbf{Z}_c , and equate it to zero.

4.2.5 Component Mode Synthesis

Equation 4.17 represents the disjoint-set of equations for the large and small cantilever components.

$$\mathbf{M}^d \ddot{\boldsymbol{\xi}} + \mathbf{K}^d \boldsymbol{\xi} = \mathbf{0} \quad (4.17)$$

\mathbf{M}^d and \mathbf{K}^d are block-diagonal compilations of the mass and stiffness matrices for each component and $\boldsymbol{\xi}$ is a vertical concatenation of the modal coordinate matrices \mathbf{a} and \mathbf{b} .

Equation 4.18 is the block-diagonal mass matrix, for example.

$$\mathbf{M}^d = \begin{vmatrix} \mathbf{M}_1 & \mathbf{0} \\ \mathbf{0} & \mathbf{M}_2 \end{vmatrix} \quad (4.18)$$

Figure 4.20 is a schematic of the system and helps to illustrate the interface of the two components.

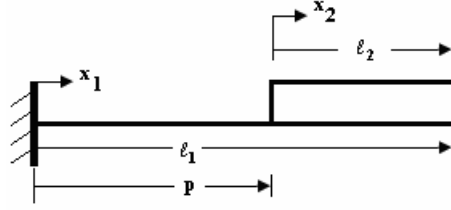


Figure 4.20: CMS System Schematic

From Figure 4.20 it is clear that the small and large cantilevers share a common transverse displacement as well as rotational motion at the point $x_1 = p$ and $x_2 = 0$.

Therefore we can derive two constraining equations for this point (Equations 4.19 and 4.20).

$$w_1(p, t) = w_2(0, t) \quad (4.19) \quad ; \quad \frac{dw_1(p, t)}{dx} = \frac{dw_2(0, t)}{dx} \quad (4.20)$$

The mass of the support between the cantilevers is neglected.

4.2.6 Elimination of Redundant Modal Coordinates

Having two constraint equations makes it possible to eliminate two modal coordinates from the set ξ . In order to do so, the constraint equations must be represented as Equation 4.21; this arises from previous notation of the total response of each component as seen in Equations 4.11 and 4.12.

$$\begin{vmatrix} \boldsymbol{\Phi}_1^T(p) & -\boldsymbol{\Phi}_2^T(0) \\ \frac{d\boldsymbol{\Phi}_1^T(p)}{dx} & -\frac{d\boldsymbol{\Phi}_2^T(0)}{dx} \end{vmatrix} \cdot \begin{vmatrix} \mathbf{a} \\ \mathbf{b} \end{vmatrix} = \mathbf{0} \quad (4.21)$$

If we choose to arbitrarily eliminate modal coordinates a_1 and a_2 (and thus label them as “redundant”) it is possible to manipulate Equation 4.21 into Equation 4.22. For this section of the discussion we will refer to $\boldsymbol{\Phi}_1^T$ as $\boldsymbol{\Phi}^T$ (large cantilever) and $\boldsymbol{\Phi}_2^T$ as $\boldsymbol{\Psi}^T$ (small cantilever).

$$\begin{vmatrix} \frac{\varphi_3(p)\dots}{dx} & \frac{\varphi_n(p)}{dx}, & -\frac{\psi_1(0)\dots}{dx} & -\frac{\psi_{n+4}(0)}{dx} \end{vmatrix} \cdot \begin{vmatrix} \mathbf{a}^* \\ \mathbf{b} \end{vmatrix} = \begin{vmatrix} -\frac{\varphi_1(0)}{dx} & -\frac{\varphi_2(0)}{dx} \end{vmatrix} \cdot \begin{vmatrix} a_1 \\ a_2 \end{vmatrix}$$

OR

$$\mathbf{Q} \cdot \begin{vmatrix} \mathbf{a}^* \\ \mathbf{b} \end{vmatrix} = \mathbf{C} \cdot \begin{vmatrix} a_1 \\ a_2 \end{vmatrix}$$

(4.22)

We now have a truncated version of the original modal coordinate matrix where $\mathbf{a}^* = [a_3 \dots a_n]^T$. The next step is to isolate the matrix $[a_1 \ a_2]^T$ by pre-multiplying \mathbf{Q} by the inverse of \mathbf{C} where $\mathbf{R} = \mathbf{C}^{-1}\mathbf{Q}$. Next, ξ can be expressed as Equation 4.23. The matrix \mathbf{B} will allow us to solve the eigenvalue problem as posed by the combined system of cantilevers.

$$\xi = \begin{vmatrix} \mathbf{R}_{2X(2n-2)} \\ \mathbf{I}_{(2n-2)X(2n-2)} \end{vmatrix} \cdot \begin{vmatrix} \mathbf{a}^* \\ \mathbf{b} \end{vmatrix} = \mathbf{B} \cdot \begin{vmatrix} \mathbf{a}^* \\ \mathbf{b} \end{vmatrix} \quad (4.23)$$

In Equation 4.23, \mathbf{I} represents the identity matrix with dimensions $2n-2$ by $2n-2$. Finally, we can write our collected set of equations as Equation 4.24 and extract the overall system mass and stiffness matrices.

$$\mathbf{B}^T \mathbf{M}^d \mathbf{B} \ddot{\mathbf{q}} + \mathbf{B}^T \mathbf{K}^d \mathbf{B} \mathbf{q} = \mathbf{0}$$

OR

$$\mathbf{M} \ddot{\mathbf{q}} + \mathbf{K} \mathbf{q} = \mathbf{0} \quad (4.24)$$

4.2.7 The Eigenvalue Problem

Since the external forcing of the system is assumed to be zero for a modal analysis, the solution to Equation 4.24 is straightforward. Equation 4.25 shows an intermediate step in which the generalized eigenvalue problem is evident.

$$(-\omega_p \mathbf{M} + \mathbf{K})\mathbf{q} = \mathbf{0} \quad (4.25)$$

The modal frequency ω_p surfaces in Equation 4.25 due to the assumed harmonic solution, $\mathbf{q} = \mathbf{q}_0 e^{i\omega t}$. The remaining expression is exactly the generalized eigenvalue problem and can be solved in MATLAB for the system eigenfunctions and corresponding eigenvalues. Table 4.1 is a list of the first five modal frequencies using four normal modes ($n = 4$) for each cantilever.

Table 4.1: CMS Modal Frequencies

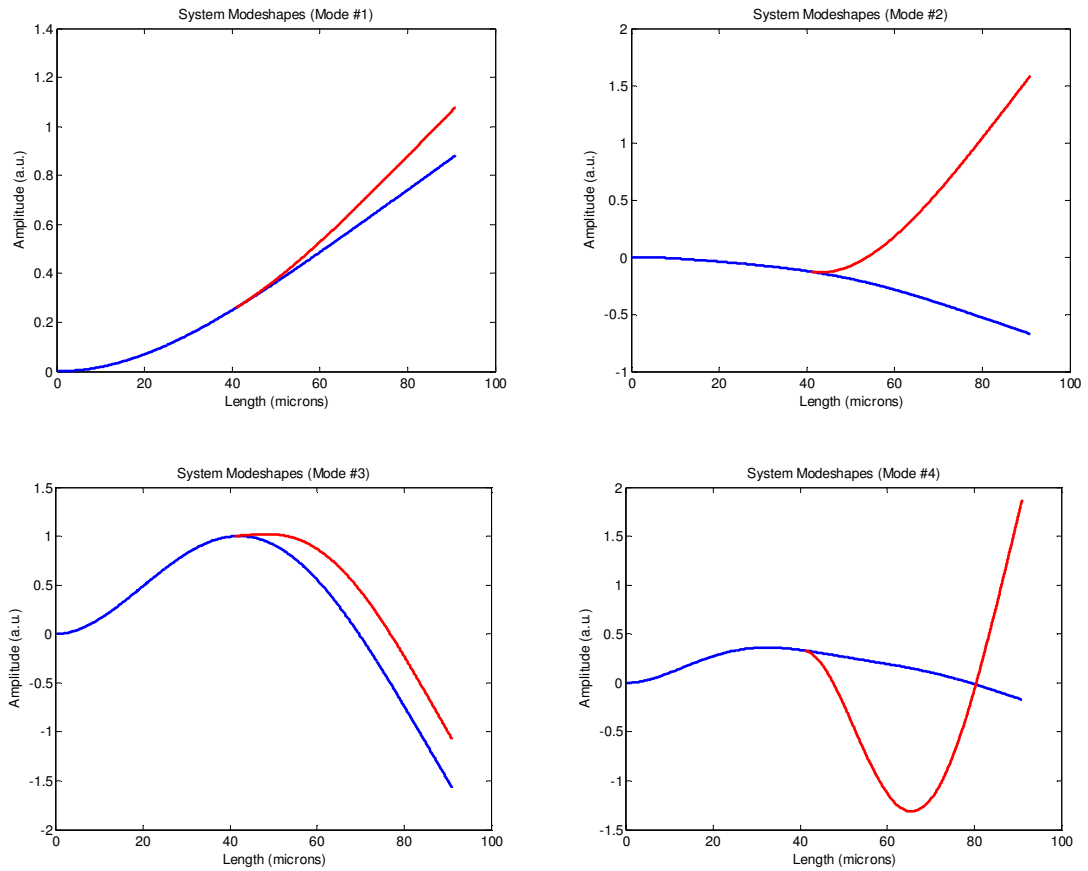
Mode #	Frequency (Hz)
1	332625.58
2	853040.8
3	2337298.7
4	4872212.8
5	7382390.7

The values in Table 4.1 were obtained using a routine in MATLAB (see appendix A). The cantilever system is assumed to be comprised of Silicon Nitride, which has an elastic modulus of 110GPa and a density of 2200kg/m³. The larger cantilever has a length, width, and thickness of 91 microns (μm), 30 μm , and 3 μm , respectively. The smaller cantilever has a length, width, and thickness of 50 μm , 30 μm , and 1.6 μm , respectively.

4.2.8 Mode Shapes

In order to plot the mode shapes of the system, the original $2n+4$ modal coordinates must be recovered (recall we eliminated two modal coordinates in section 4.2.7). Since $\xi = \mathbf{B}\mathbf{q}$ it is possible to back-solve for the remaining two coordinates and thus proceed with the full set. Pairing the eigenvectors (also acquired from the

MATLAB routine) with their respective eigenvalues allows us to plot the normalized mode shapes. Note that in figure 4.21 the amplitudes of each cantilever are expressed in arbitrary normalized units and the shapes of the beams are exaggerated to display the deformation.



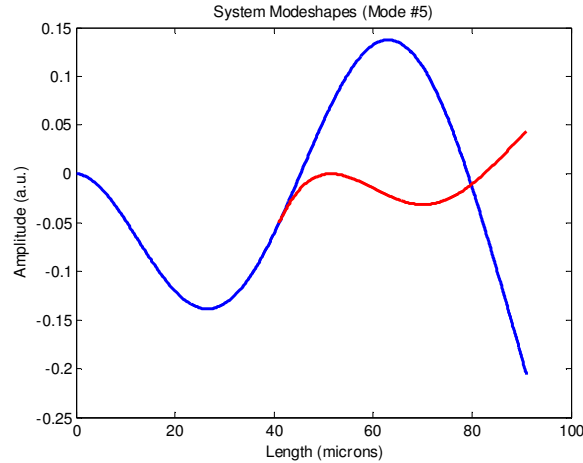


Figure 4.21: First Five System Mode Shapes; Red Curve Indicates Smaller Cantilever

Figure 4.21 depicts how the oscillation of the larger cantilever directly affects the oscillation of the smaller cantilever. For example, the first mode shows minimal oscillation contribution from the small cantilever since this system frequency corresponds to the fundamental frequency of the large cantilever (~350 kHz). Similarly, the second mode shows minimal contribution from the large cantilever since this system frequency corresponds to the fundamental frequency of the small cantilever (~850 kHz). During higher modes of oscillation (i.e. 3 through 5) the system begins to exhibit equal motion from both cantilevers. In modes 4 and 5, the intersecting curves (blue and red) are misleading since the cantilevers never come in contact because of small-angle deflection; they are also separated by a large air gap on the order of several microns.

4.2.9 Validation

Finite element analysis (FEA) is an accurate means of validating the CMS of any system. In order to test convergence of the first five modal frequencies of the system

(Table 4.1), a two-dimensional finite element model was constructed in ANSYS assuming the same dimensions and material properties used in the MATLAB CMS routine. Figure 4.22 represents the meshed finite element model of this particular dual cantilever system.

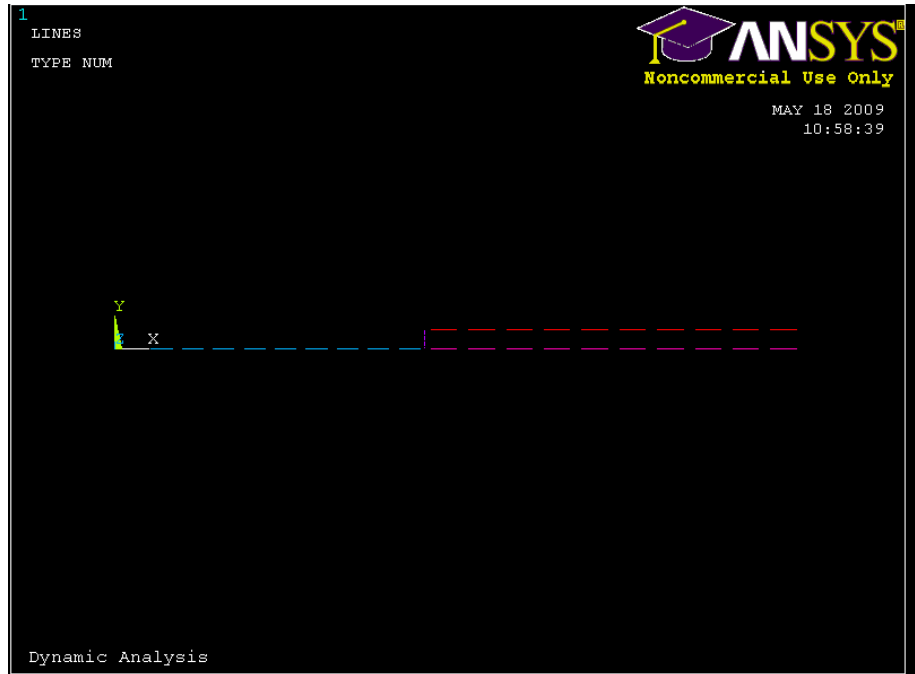


Figure 4.22: FEM of a Dual Cantilever System

To simulate the fixed-free boundary condition, all degrees-of-freedom at $x = 0$ are assumed to be zero (clamped). The support in between the two cantilevers creates an interesting challenge since it cannot assume a zero mass in ANSYS. In order to remedy this issue, the support was set to have the density of Silicon Nitride (2200 kg/m^3) but a high elastic modulus of 8000 GPa to simulate a rigid connection. This assumption is well-justified considering the nature of the connector beam. The connector beam was analyzed separately in ANSYS as a fixed-fixed beam, which produced a fundamental

resonance frequency in the range of GHz; this frequency is well above even the fifth mode of the entire system therefore it is assumed that for system modes below the fifth mode, the connector beam does not contribute significantly to the modal motion. If we proceed with this assumption, the connector beam is “rigid” and mimics the same scenario used in the CMS MATLAB routine. It is noteworthy however that this is the only source of error during validation. Table 4.2 lists the first five modal frequencies as obtained from ANSYS.

Table 4.2: ANSYS Modal Frequencies

Mode #	Frequency (Hz)
1	332035
2	842296
3	2333852
4	4803206
5	7262572

The results from Table 4.2 were obtained by meshing each line in the finite element model with 40 elements (a total of 160 system elements); convergence occurs when increasingly more elements are used in the model. Likewise, convergence occurs when more and more normal modes are added to the CMS routine. Table 4.3 is the convergence progression for each method (CMS and ANSYS) while Figure 4.23 is a plot of CMS percent error assuming the 40-element ANSYS model produces perfect modal frequencies.

Table 4.3: CMS, ANSYS Modal Frequency Convergence

ANSYS MODE CONVERGENCE (Hz)					
# of beam elements per cantilever	4	16	20	24	40
mode 1	332331	332036	332035	332035	332035
mode 2	845603	842323	842307	842301	842296
mode 3	2366761	2334167	2333978	2333909	2333852
mode 4	6957708	4808230	4805290	4804163	4803206
mode 5	9142097	7267220	7264487	7263451	7262572
CMS MODE CONVERGENCE (Hz)					
# of normal modes	4	6	8	10	12
mode 1	332626	332486	332420	332384	332361
mode 2	853041	849572	847983	847108	846566
mode 3	2337299	2337017	2336930	2336892	2336872
mode 4	4872213	4851915	4842919	4837940	4834803
mode 5	7382391	7379172	7377782	7377023	7376547

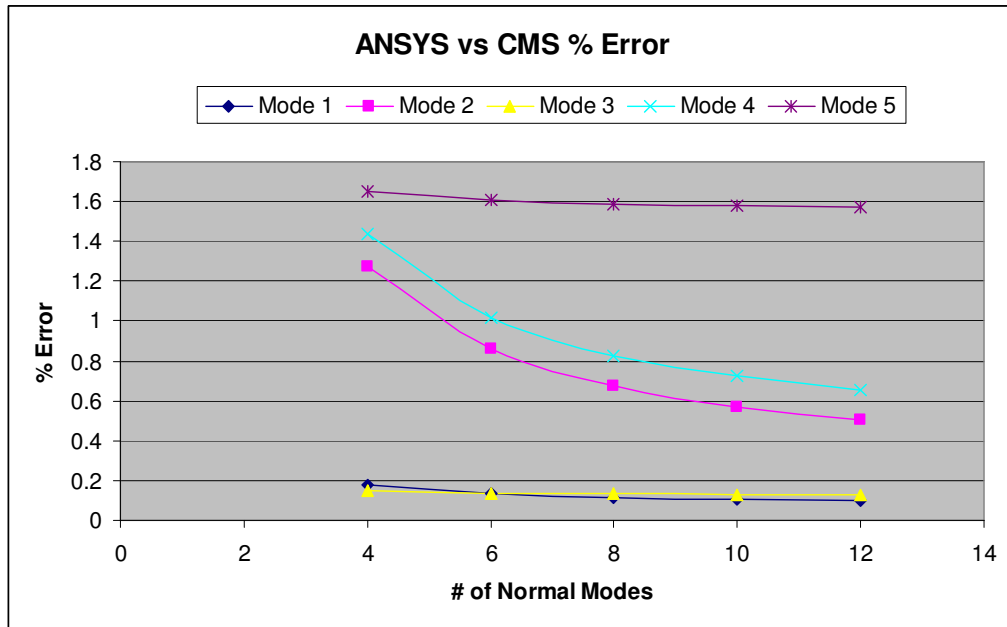


Figure 4.23: Percent Error in CMS Convergence

With only four normal modes considered in the CMS routine, the maximum error is under 2% and occurs for the fifth mode, which is expected. If n system modes are

considered in the calculations then the n^{th} mode will have the poorest estimate i.e. if we consider four normal modes for each cantilever this is a total of 12 system modes (normal, rigid body and constraint modes) and therefore the 12th mode will be the least accurate. As more normal modes for each cantilever are considered, the percent error begins to reduce as seen in Figure 4.6. Figures 4.24 and 4.25 depict how quickly each method converges; the CMS method produces accurate results using a minimal number of modes while ANSYS requires at least 16 elements per line segment (a total of 64 system elements) to produce comparable results.

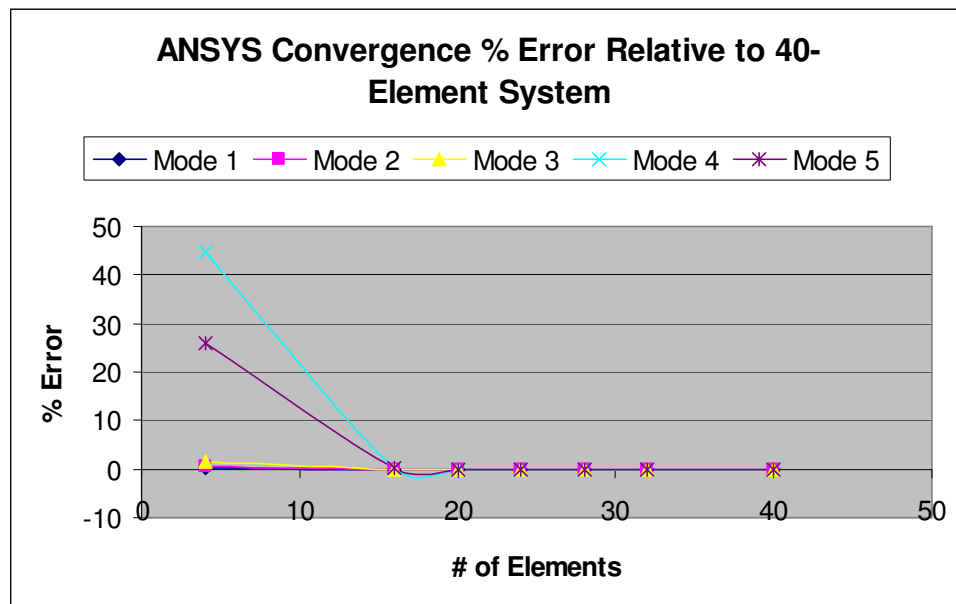


Figure 4.24: ANSYS Mode Convergence

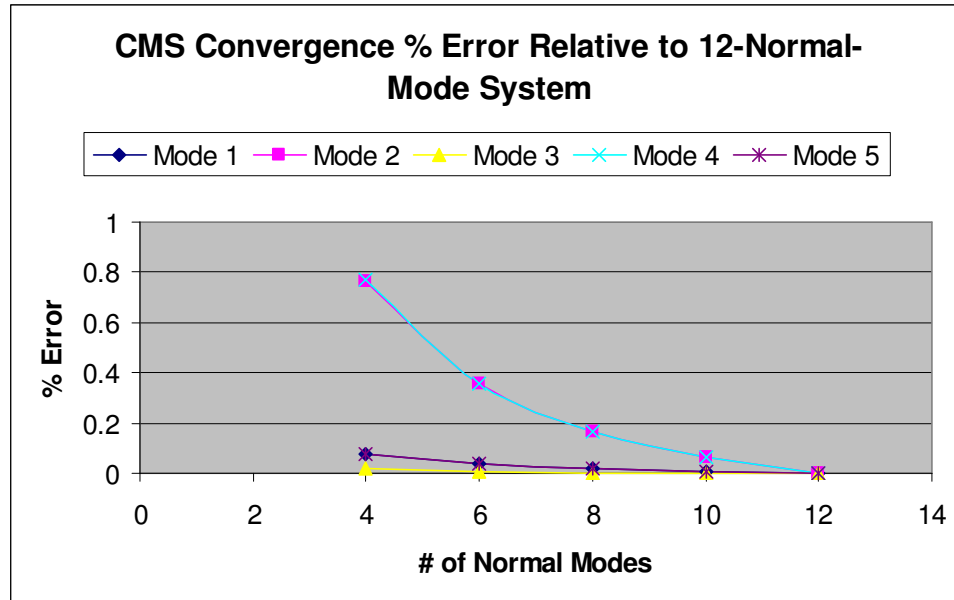


Figure 4.25: CMS Mode Convergence

4.2.10 Discussion

As previously mentioned, computation time and power are highly dependent on the number of degrees of freedom associated with the model. Figure 4.8 demonstrates that accurate results can be obtained with only 4 normal modes per cantilever (12 system modes) which translates to 12 degrees of freedom. In order to achieve the same accuracy with ANSYS, the finite element model must contain at least 16 elements per section (64 system elements) which translates to approximately 380 degrees of freedom. The MATLAB routine is executed within a matter of seconds while ANSYS may take several minutes. Reducing the number of elements in the ANSYS finite element model will drastically reduce computation time but this significantly decreases accuracy.

Since the mathematics behind the derivation of the CMS routine involve only in-plane transverse displacement and rotation, the comparative ANSYS model was constructed as two-dimensional (Figure 4.22). When compared to a three-dimensional

ANSYS finite element model, the modal frequencies begin to significantly disagree after the 3rd or 4th mode. This is a result of torsional and out-of-plane bending modes that are not present in the CMS code. As expected the mathematics increase in complexity when more degrees of freedom are considered; but this alteration would make the code much more accurate and all-encompassing. Only the first two modes of the dual cantilever system are important in this work because we are only concerned with the 3dB bandwidth of the large cantilever and the first resonance mode of the small cantilever, which are both below one megahertz. Since all other modes occur well over one megahertz they are assumed to not contribute significantly to the system response. However, if high-frequency modes (i.e. torsional) become relevant to the analysis, their addition to the routine is very straightforward.

Table 4.4 summarizes the dual cantilever devices considered in this work. It is more concise to use the code of each device as opposed to listing the dimensions at every juncture. Actuator cantilever codes are preceded by an ‘A’ while sensor cantilever codes are preceded by a ‘C’.

Table 4.4: Summary of Cantilevers

W (um)	L (um)	H (um)	Code
53.9	92	2.948	A9
74.63	92	2.948	A10
29.02	92	2.948	A8
15.67	50	1.632	C2
31.35	50	1.632	C3
20.9	50	1.632	C1

For example, a device containing cantilever C2 atop cantilever A8 would be referred to as device A8C2. The base cantilever must be wider than the top cantilever; this restricts

the combinations to devices A8C2, A9C1 and A9C3. From Figures 4.7 and 4.8 it is assumed that the ANSYS model will contain 16 beam elements per line segment (384 elements total) and the CMS code will utilize 10 normal modes (24 system modes). Table 4.5 is a comparison of the outputs from a 3D ANSYS (out-of-plane motion accounted for) model, a 2D ANSYS (no out-of-plane modes) model, and the CMS approach.

Table 4.5: ANSYS vs. CMS for Actual Devices

Device	mode	3D ANSYS frequency	2D ANSYS frequency	CMS frequency
A9C3	1	350624.257	344298.6	344538.941
	2	731868.7	817762.2	821428.365
	3	1477630.4	2334875.44	2337857.2
	4	2369733.9	4795772.1	4823927.85
	5	2495266.2	6997247.466	7072240
A9C1	1	365899.5	359126.3	359316.764
	2	704420.7	796790.8	799643.693
	3	1511956.3	2380715.7	2383829.55
	4	2420030.1	4757809	4781113.6
	5	2836301	6984559	7042393.5
A8C2	1	350537.1	347302.3	347532.407
	2	720496.6	813473.1	816965.803
	3	2270246.1	2344325.7	2347334.58
	4	2362604.6	4788119.8	4815246.78
	5	2535814.8	6994546.7	7065871.45

As expected, the 3D ANSYS results do not agree with the CMS results after the second modal frequency. However, the 2D ANSYS results agree to within ~1% error, which is illustrated in Figure 4.26. It is important to note that even though the widths of each cantilever differ (therefore the structure is not uniform out-of-plane), the area-moment of inertia accounts for this in the routine and therefore complex three-dimensional mathematics is avoided.

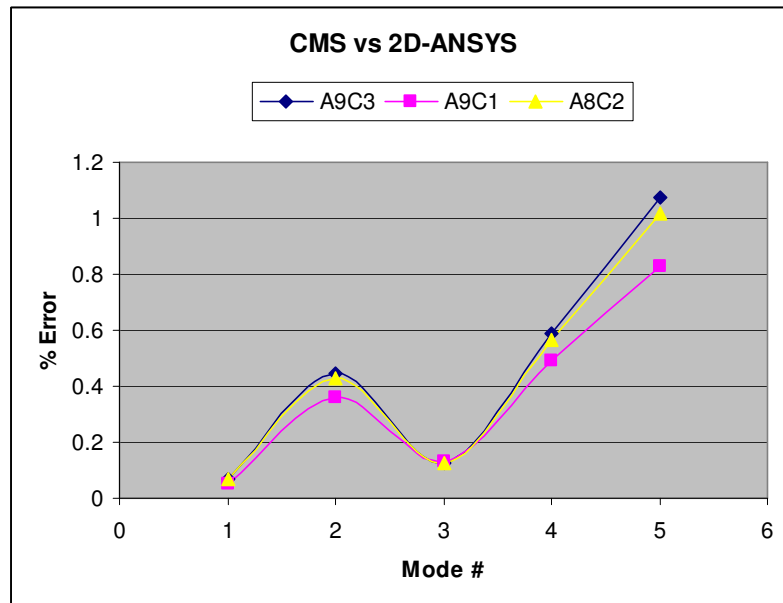


Figure 4.26: Percent Error Plot of CMS Relative to ANSYS Results

It is expected that if more modes are included in the CMS routine then a greater accuracy is obtained for the first several modes.

Incorporating an air-damping scheme into CMS would increase the accuracy of the model; this is realized by the addition of a Winkler foundation which is generally an addition of spring and dashpot elements connected in parallel to the entire base of the oscillating cantilevers [38, 39]. These additional stiffness and damping elements are simply incorporated into the energy contributions and a damping matrix becomes evident in the mathematics (a stiffness matrix already exists).

CHAPTER 5: DEVICE FABRICATION

5 Process Flow

A novel process flow was developed in order to overcome the logistical challenge of fabricating stacked structures. Since material selection is paramount, the eight-mask process was executed using several trial wafers in order to check material characteristics such as etch-selectivity, etch-rate, etc. A process flow was finalized, which can be seen in the following figures in consecutive order; the dual cantilever case is used as an example since the cross-sections of the device are simple to visualize (the other device combinations utilize the same exact process flow). The process flow requires at least eight lithography steps (and therefore eight masks), all of which are used as etch masks with the exception of the first step, the lift-off process.

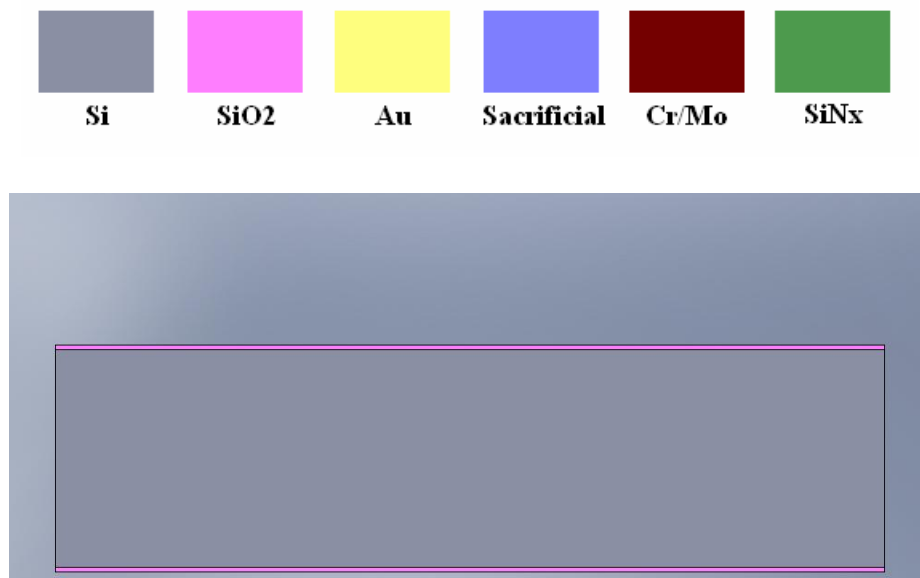


Figure 5.1: Thermally Oxidized Wafer

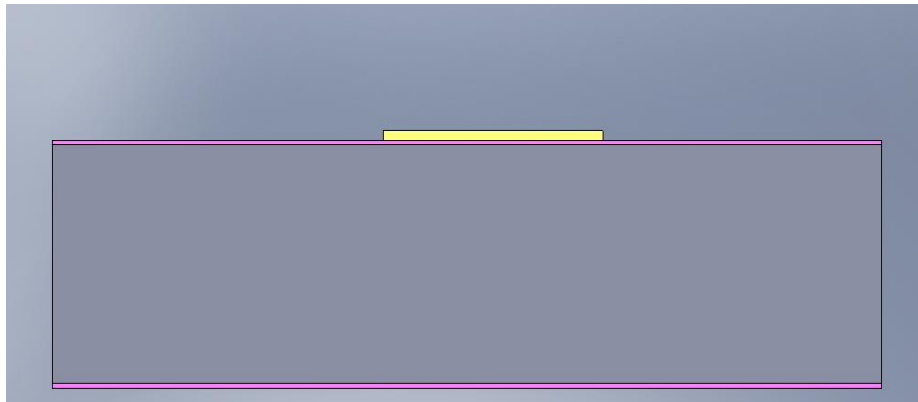


Figure 5.2: First Electrode

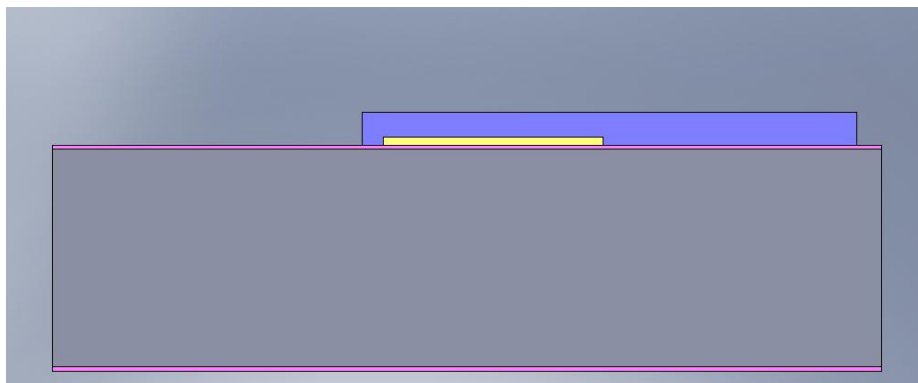


Figure 5.3: First Sacrificial Layer

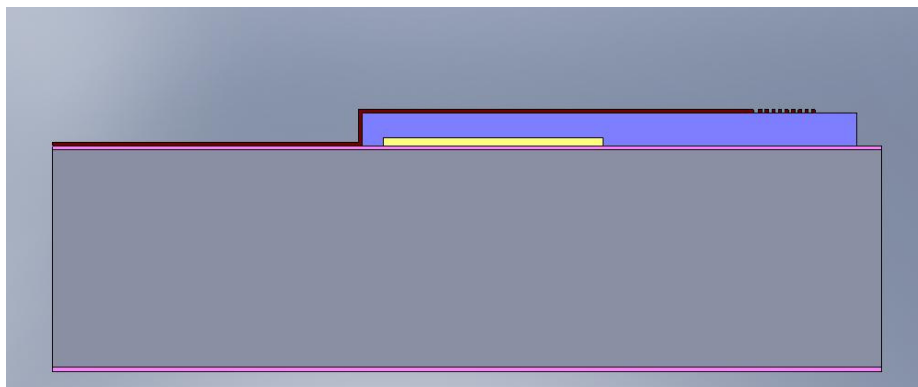


Figure 5.4: Second Electrode / Diffraction Grating

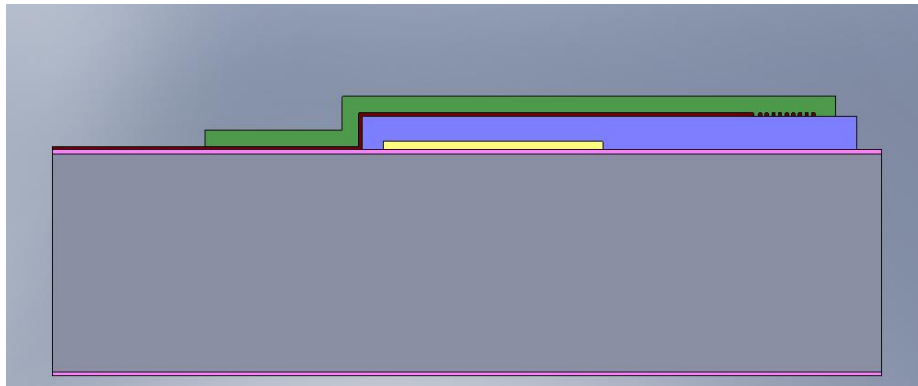


Figure 5.5: First Cantilever

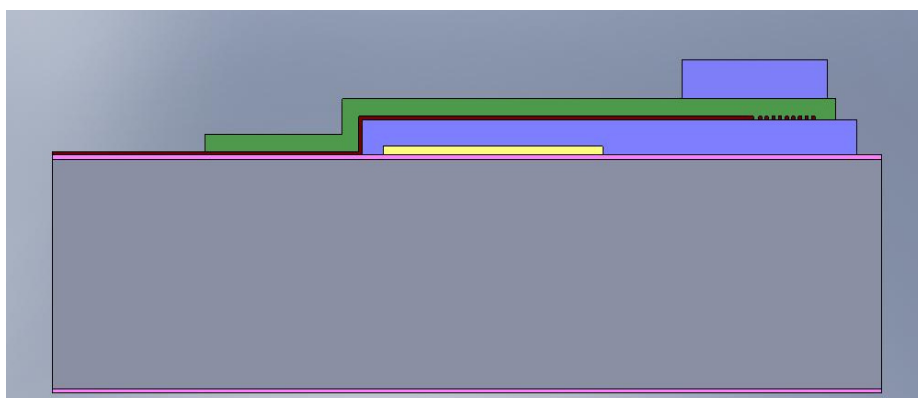


Figure 5.6: Second Sacrificial Layer

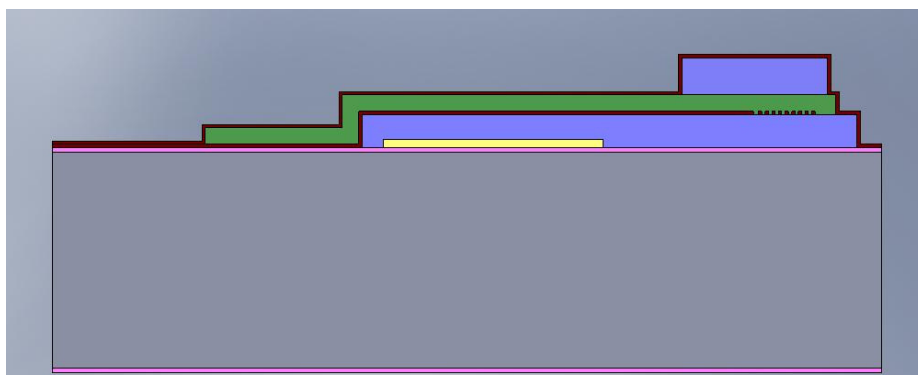


Figure 5.7: Third Electrode Deposition

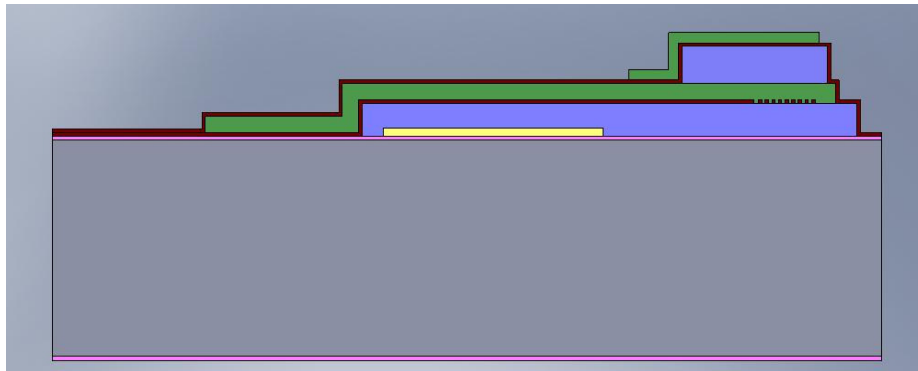


Figure 5.8: Second Cantilever

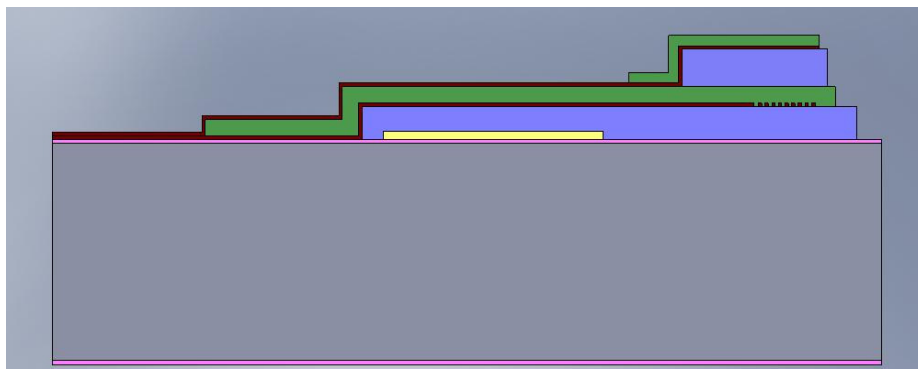


Figure 5.9: Third Electrode Patterning

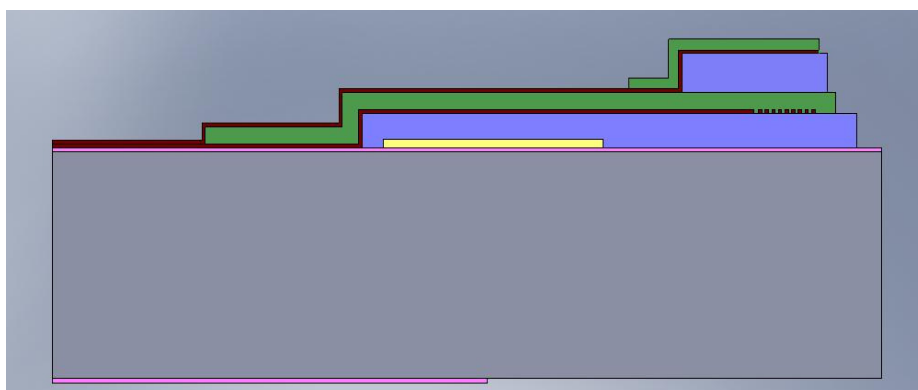


Figure 5.10: Backside Etch Mask

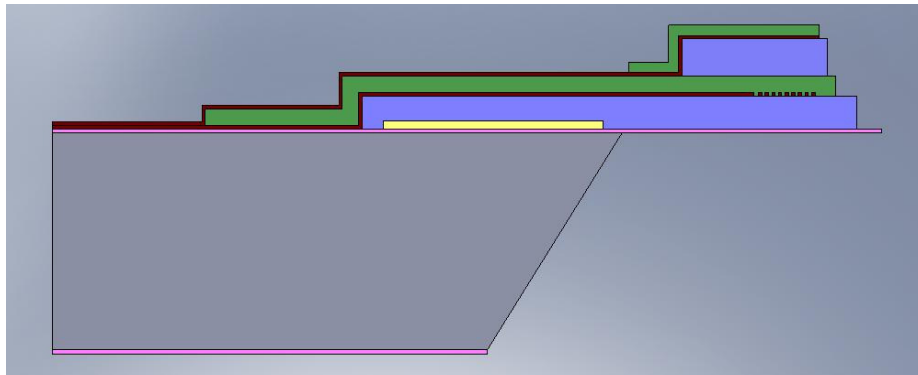


Figure 5.11: KOH Backside Etch

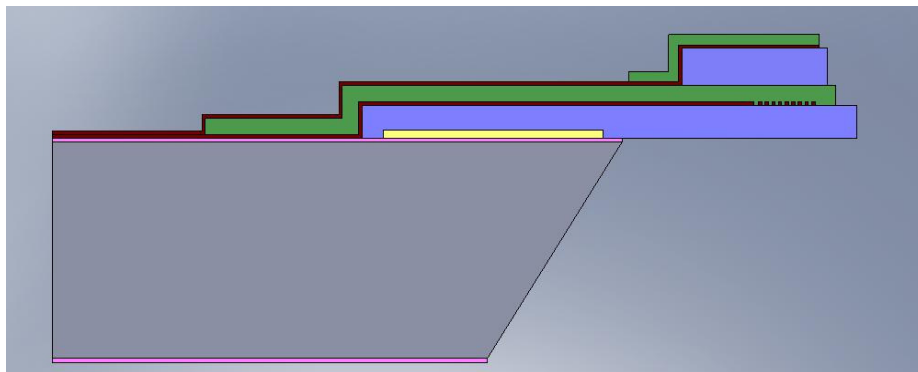


Figure 5.12: BOE Etch of Remaining Oxide

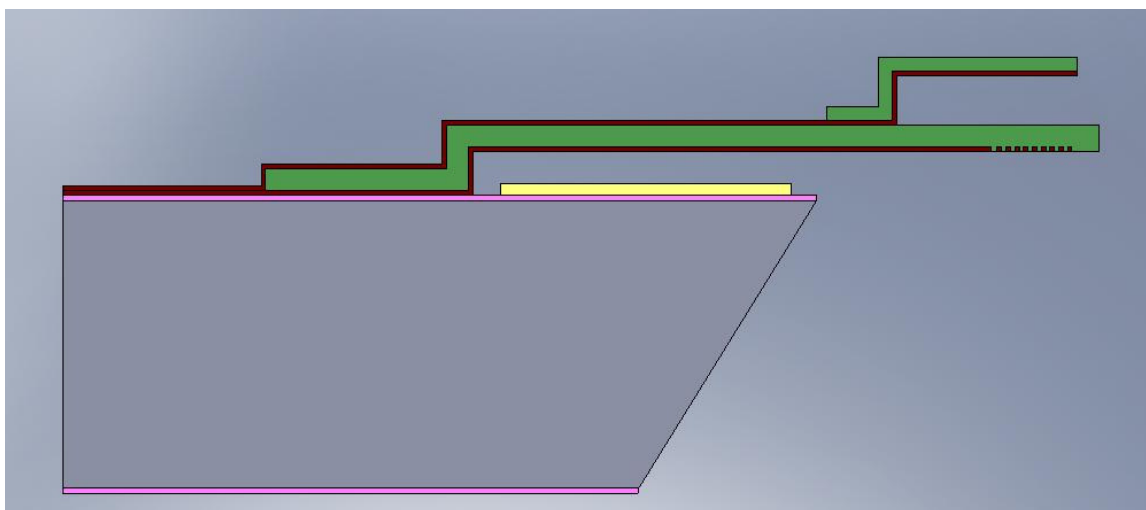


Figure 5.13: Released Dual Cantilever Device

Each step in the process flow will be outlined in detail in the following sections. In addition to the successful fabrication process, this work will discuss various shortcomings of the materials that were tested during the preliminary fabrication phase. At the start of most sections is a schematic of the desired outcome. All photoresist and etch recipes can be found in Appendix A.

5.1 Isolation Layer on Silicon Substrate

As mentioned in the design requirements section, the devices will be surface-micromachined atop a Silicon substrate; this allows for a final bulk micromachining step known as KOH backside-etching (detailed in a later section). To begin, the wafer must be thoroughly cleaned using either a CMOS cleaning process or a particular order of solvent rinsing (Acetone + Methanol + Isopropanol) in the attempts to remove stray organic particles from the wafer surface. The wafer is then prepared for either thermal oxidation growth in a furnace or Silicon Oxide (SiO_2) deposition via plasma-enhanced chemical vapor deposition (PECVD). The advantage of thermal oxidation is the coverage of both wafer sides, unlike PECVD which only deposits on the polished wafer face. SiO_2 must eventually exist on the backside (unpolished) of the wafer in order to serve as a mask for the final backside etching step. The ideal thickness of thermal oxide as measured by the Nanospec refractometer is approximately one micron.

5.2 Lift-Off Patterning of First Electrode

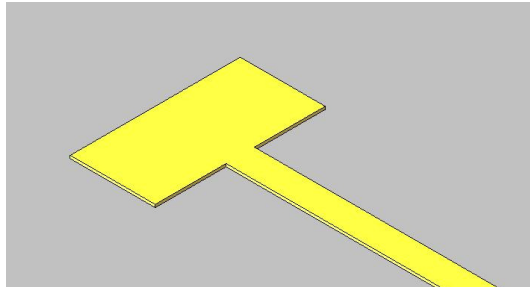


Figure 5.14: Schematic of First Electrode

Since no alignment is necessary for the first lithography step, the first mask was designed with dark-field polarity such that the lift-off process becomes possible. Following the spin-on application and patterning of SPR 220 7.0 positive photoresist (PR), 300 Angstroms of Titanium (Ti), 1000 Angstroms of Gold (Au), and finally 300 Angstroms of Chromium (Cr) were evaporated onto the wafer at a low deposition rate in order to promote thin-film uniformity. Next, the wafer was immersed in Acetone for approximately one hour in order to dissolve the PR and consequently “lift-off” the metal in the regions where the photoresist is present. The remaining pattern consists of the Ti-Au-Cr electrode and bond pad (Figure 5.15).

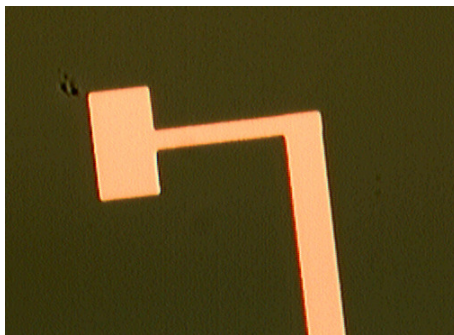


Figure 5.15: Successful Lift-Off Patterning of First Electrode

Dangling PR would often remain after Acetone immersion; this can be remedied with a three-minute ultrasonic agitation of the wafer while immersed in Acetone.

5.3 First Sacrificial Layer

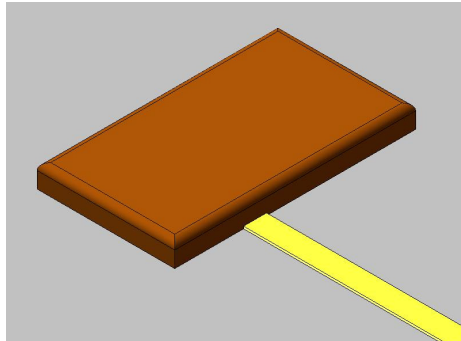


Figure 5.16: Schematic of First Sacrificial Layer

Perhaps the most critical material, the first sacrificial layer is meant to withstand etchants for the remaining course of the surface-micromachining. After various materials were tested (Aluminum, SiO_2 and amorphous Silicon), the best combination was chosen for the actual device-grade wafer. Figure 5.17 shows all three materials tested as first sacrificial layers.

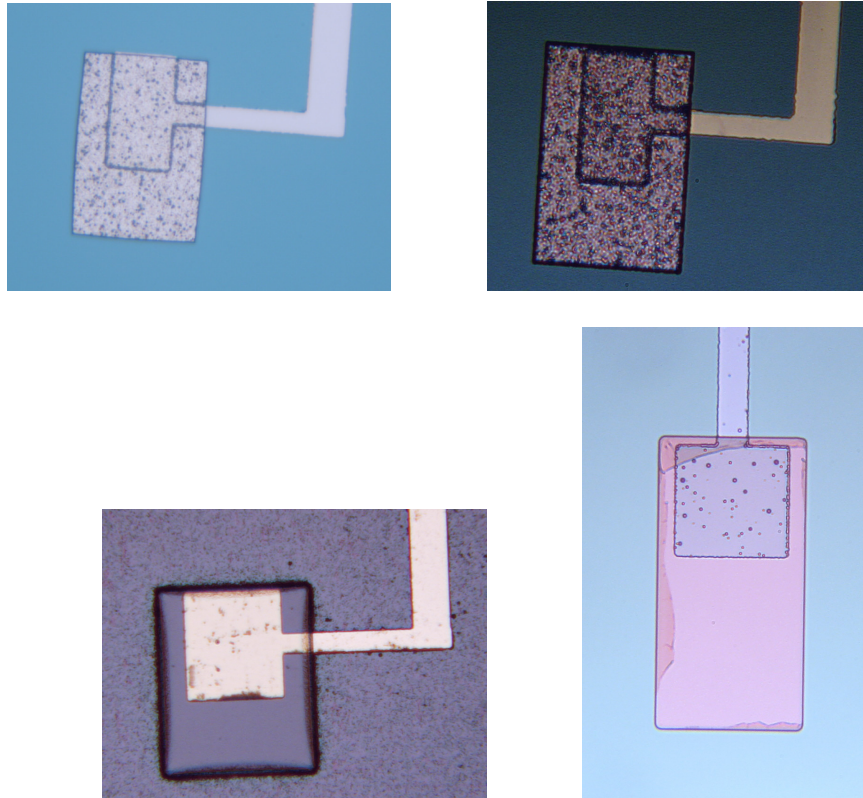


Figure 5.17: Top Left) Al Sacrificial Layer, Etched with Al Type-A Etchant at 50°C. Top Right) Al Sacrificial Layer, Etched with Al Type-A Etchant at Room Temperature. Bottom Left) SiO₂ Sacrificial Layer Etched by Reactive Ion Etch (RIE). Bottom Right) Amorphous Silicon Sacrificial Layer Etched with Inductively Coupled Plasma (ICP) Using the Bosch process [40].

It is apparent from Figure 5.17 that undercut enormity greatly depends upon the etch method. The etch rate of wet-etchants generally increases with temperature (as in the case of Al Type-A etch) and this causes a drastic undercut of the PR pattern due to poor anisotropy. When etched using RIE or ICP, the sacrificial layer dimensions remain intact; this is due to the anisotropic nature of dry-etch methods. For the final process, amorphous silicon (aSi) was chosen as the first sacrificial layer (Figure 5.17, bottom

right); this material is deposited via PECVD at a high rate (approximately 2.5 microns per hour) while maintaining excellent surface uniformity. The aSi is readily attacked by Potassium Hydroxide (KOH), which will be used to eventually release the devices from their sacrificial layers. The process attempts to avert the use of SiO₂ as a construction material since it requires Hydrofluoric acid (HF) as an etchant; HF causes damage to the nitride structures.

5.4 Second Electrode / Diffraction Grating

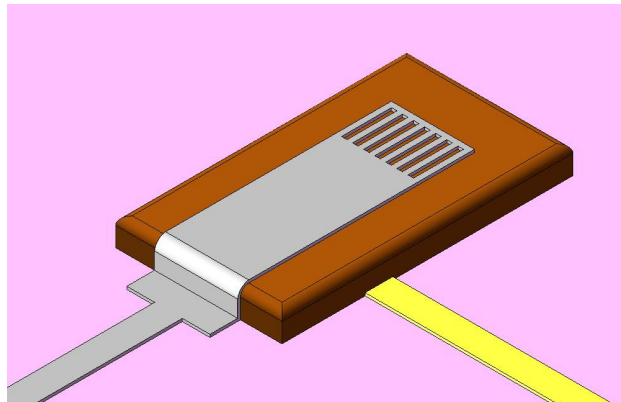


Figure 5.18: Schematic of Second Electrode / Diffraction Grating

Approximately 2000 Angstroms of Cr was sputtered onto the wafer at a low deposition rate of 300 Angstroms per minute in the Unifilm Sputterer. Shipley 1813 positive PR was patterned onto the metal in order to etch the second electrode and diffraction grating patterns. As mentioned in the previous section, wet-etchants can create a deep undercut of the photoresist pattern and are often difficult to control in terms of etch rate. Figure 5.19 illustrates the adverse effects of wet-etching when two-micron features are involved.

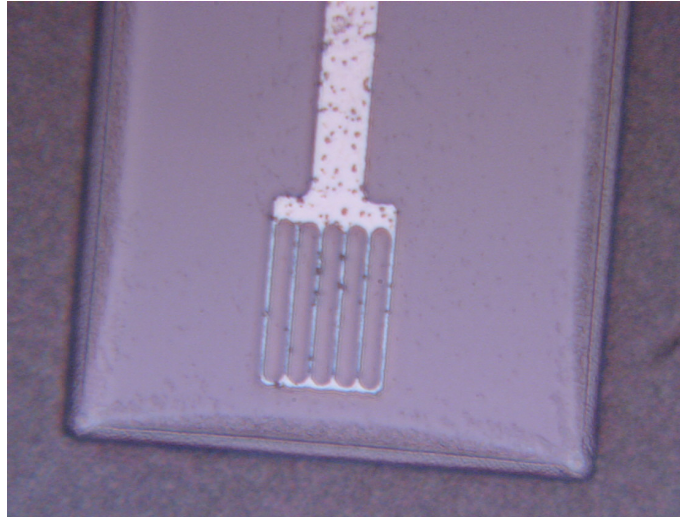


Figure 5.19: Deep Undercut of Cr Diffraction Grating

The diffraction grating seen in Figure 5.19 no longer contains a periodicity of four microns. It was discovered that jostling the wafer during the wet-etch step causes greater undercut; if the wafer remains undisturbed for approximately six minutes in Cr7s Cr-etchant, the features remain intact (Figure 5.20).

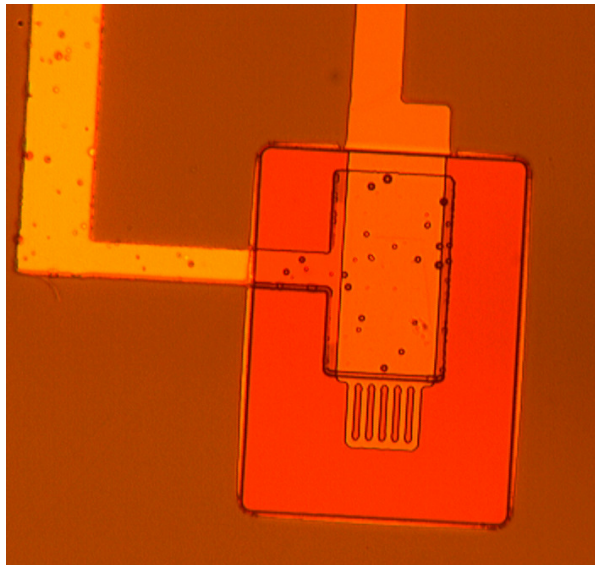


Figure 5.20: Intact Wet-Etched Cr Diffraction Grating

The wet-etch method is considerably less difficult than RIE or ICP etch; however it is not guaranteed that the grating fingers will remain intact. The graininess and speckled appearance of the metal layers is due to the non-uniformity of the thin-film deposition. Since metal sputtering occurs at low-vacuum pressure ($\sim 10^{-3}$ Torr) the uniformity is expected to be of a lesser quality in relation to metal evaporation. Sputtering metal at a very low deposition rate is proven to increase thin-film uniformity. Ti was avoided for this step since it must be etched using HF; once again this causes unwanted etching of the nitride structures; Figure 5.21 illustrates the adverse effects of HF in this fabrication process.

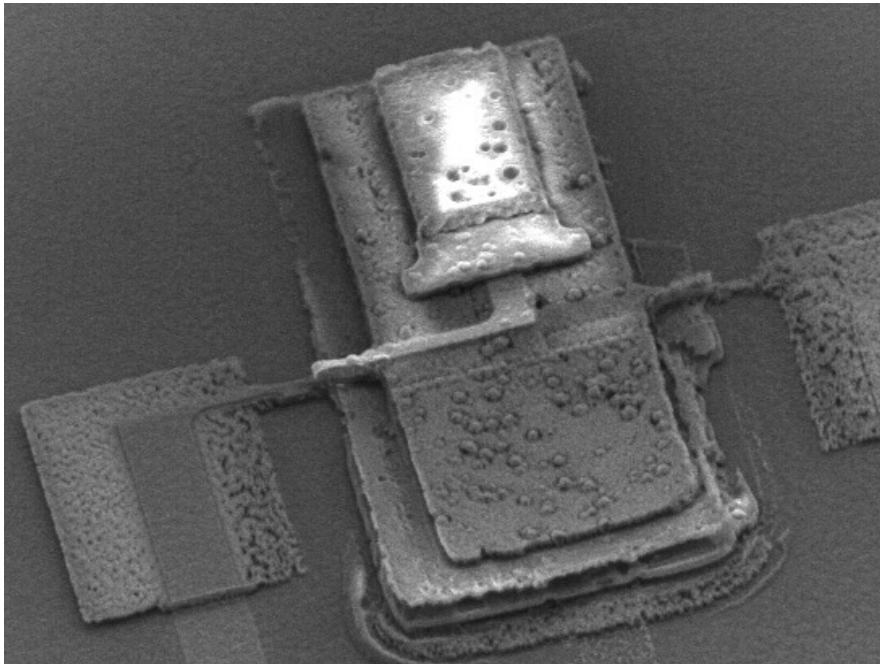


Figure 5.21: Scanning Electron Micrograph of HF-Damaged Nitride Cantilever-on-Seesaw Lever Device

The SEM image of the damaged structure illustrates evidence of dissolved nitride as well as the delamination of the substrate electrode.

5.5 Silicon Nitride Actuator

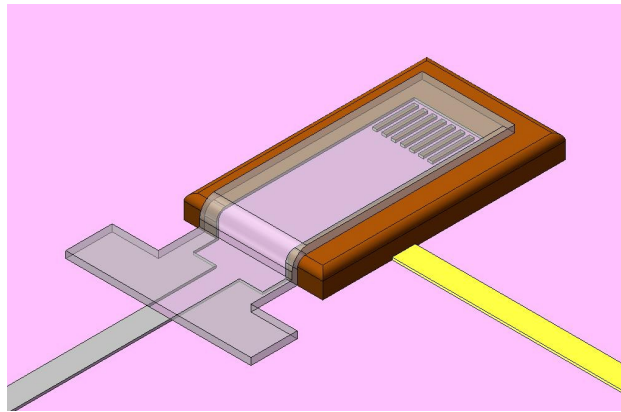


Figure 5.22: Schematic of First Silicon Nitride Cantilever

Three microns of low-stress PECVD silicon nitride (SiN_x) was deposited for the actuator structure. Using SPR 220 7.0 positive PR, the actuator patterns were formed and the wafer was etched using an SF_6/O_2 plasma RIE at high power. The same recipe was used for all test wafers and little problem was encountered during this step. Figure 5.23 is a microscope image of a SiN_x cantilever actuator atop a grainy Al sacrificial layer. Although it appears that the remainder of the device (the sacrificial layer, the second electrode) is in poor shape, the actuator cantilever is very well defined.

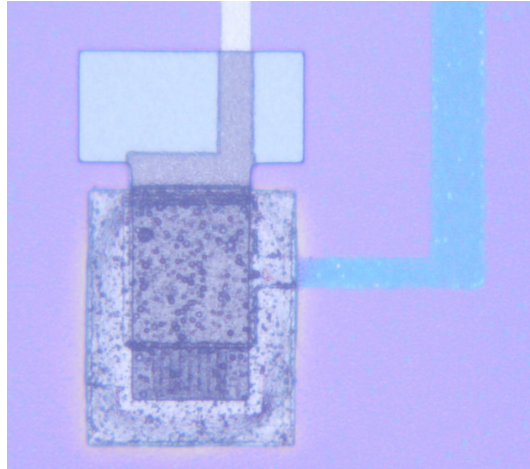


Figure 5.23: First SiN_x Cantilever

Etch time is critical since the etch recipe for SiN_x will also readily attack the insulating SiO₂ if exposed for too long. Since the plasma-etch recipe contains O₂ gas, there will be a proportional ablation of the masking PR, thus it is important to use a thick resist during lithography. The SiN_x actuators on the wafer from Figure 5.20 were patterned using a low-powered RIE recipe and thus an undercut is evident (Figure 5.24).

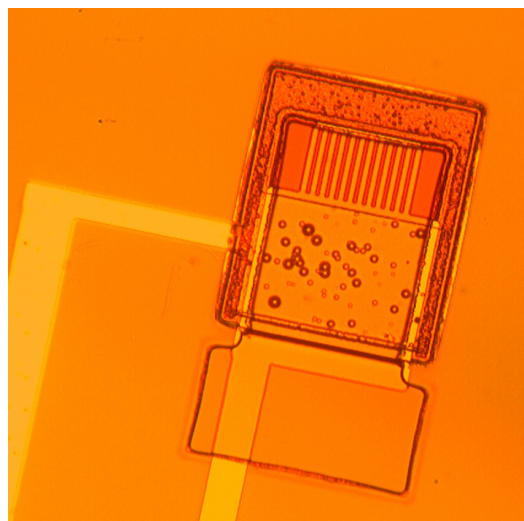


Figure 5.24: Undercut of SiN_x Cantilever Actuator

In Figure 5.24 the second electrode is visibly protruding from the sides of the cantilever actuator and will eventually be etched during a final Cr-etching step. Also apparent in Figure 5.24 is the slight etching of the aSi sacrificial layer by the RIE recipe. The wafer is next covered in a protective Al layer, 500 Angstroms in thickness, such that the ICP-etch of the second sacrificial layer does not attack any of the existing features.

5.6 Second Sacrificial Layer

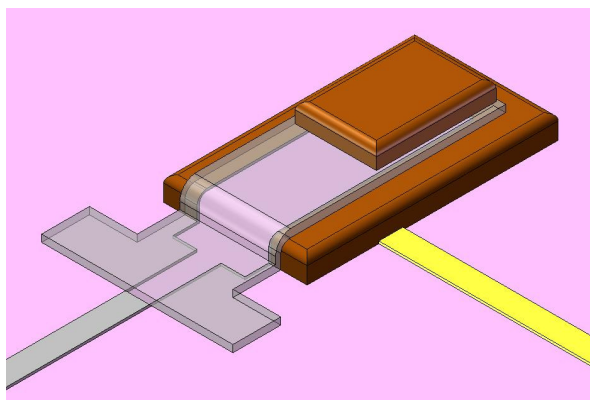


Figure 5.25: Schematic of Second Sacrificial Layer

Since aSi proved to be a highly uniform material, it was again chosen for this step. The second sacrificial layer is patterned in the same manner as the first sacrificial layer, using ICP with the Bosch process. Since there is a protective 500 Angstrom Al layer, the underlying features should remain intact through the duration of the etch step. Al was tested as a second sacrificial layer, however since this layer is targeted at approximately 4 microns in thickness, the aspect ratio is increased and thus undercut was much more drastic. From Figure 5.26 it is apparent that the feature has been attacked from all four sides, leaving the sacrificial layer both undersized and jagged. The

topography of the diffraction grating is also evident in the second sacrificial layer; this unavoidable regardless of the material chosen for this step. Since a high deposition rate was used in the application of the four micron Al layer, the grain size is large and the uniformity of the sacrificial layer is quite poor.

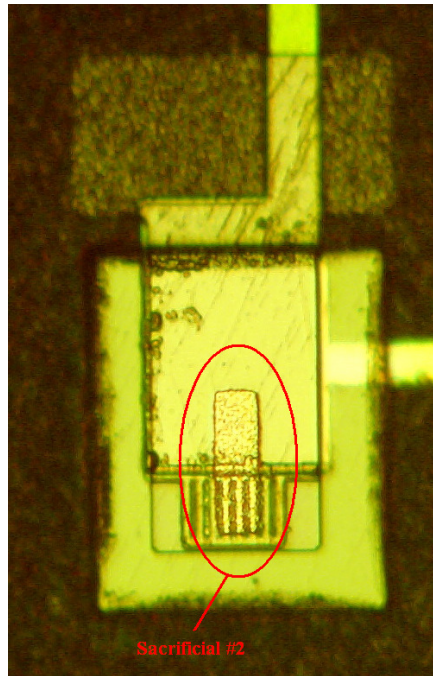


Figure 5.26: Al Second Sacrificial Layer

The dimensions of the second SiN_x structure (or sensor) are dependent upon the geometry of the second sacrificial layer; it is imperative that a highly anisotropic etch method be employed during this step. Figure 5.27 is an optical micrograph of an aSi sacrificial layer atop a cantilever actuator; notice the uniformity and smooth edges. The diffraction grating periodicity appears to have changed, however this is not the case and can be attributed to the microscope objective. Once the aSi sacrificial layer has been patterned,

the wafer is immersed in Al Type-A etchant in order to etch the protective Al, leaving Al only beneath the aSi (Al is also readily attacked by KOH during device release).

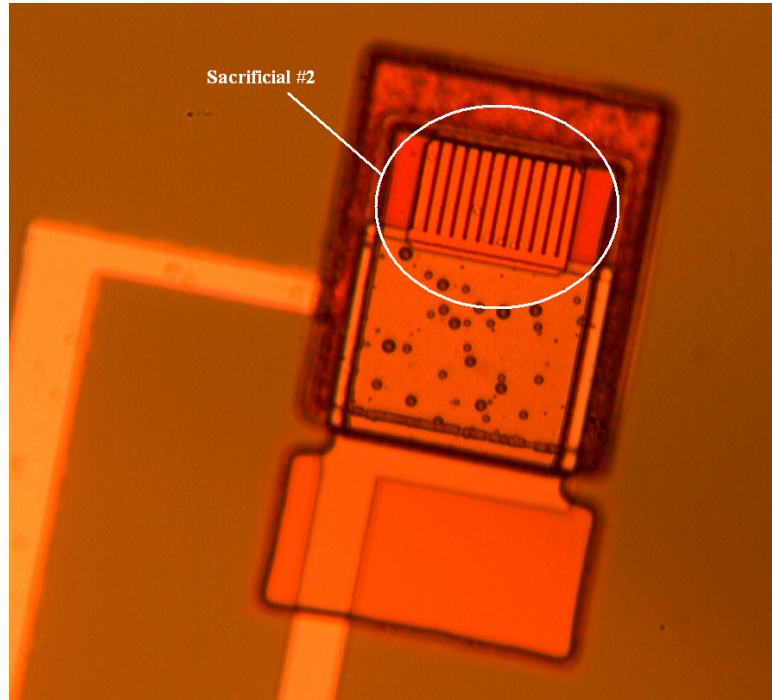


Figure 5.27: Amorphous Silicon Second Sacrificial Layer

Directly after the patterning of the second sacrificial layer, a 2000 angstrom layer of Cr is sputtered onto the wafer. This Cr layer will serve as a protective layer when plasma-etching the second nitride structure (refer to Figure 5.7); it will also eventually be patterned into the third electrode as a final step.

5.7 Silicon Nitride Sensor and Third Electrode Patterning

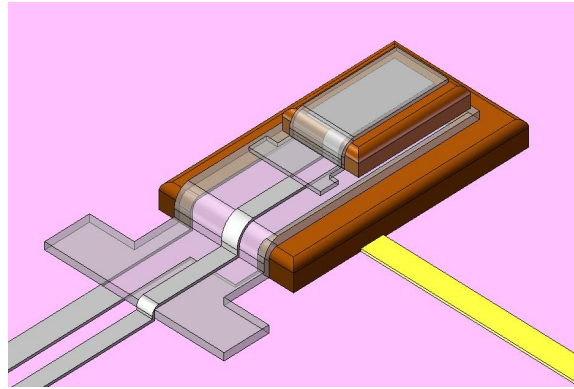


Figure 5.28: Schematic of Second Nitride Cantilever and Third Electrode

Following the deposition of the protective Cr layer, approximately 1.5 microns of SiN_x is deposited via PECVD. Using the same RIE recipe from section 5.5, the second SiN_x structure is defined. The thin Cr protective layer is not affected by this etch step and therefore the underlying features remain fully intact.

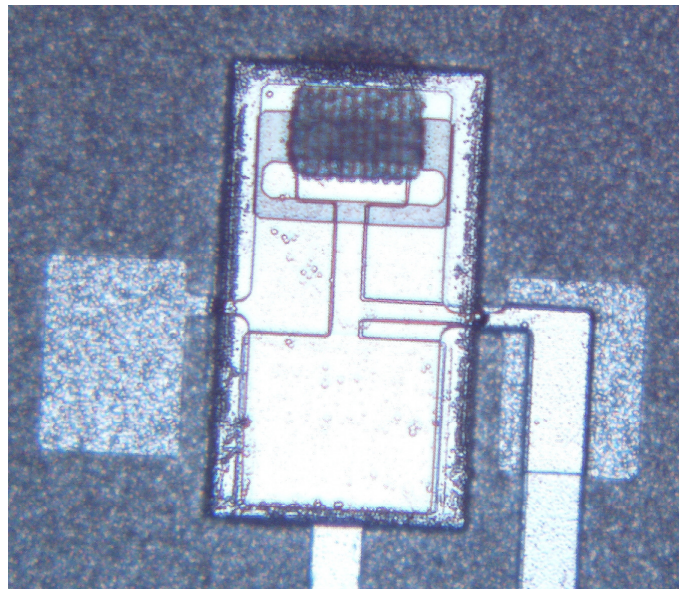


Figure 5.29: Bridge Sensor atop Seesaw Lever Actuator

Figure 5.29 is a microscope image of a patterned SiN_x bridge atop a seesaw lever actuator; the image appears shiny metallic due to the presence of the protective Cr layer beneath the sensor. Thinning of the bridge structure is evident in Figure 5.29 and is due to a lack of masking PR. As previously mentioned, the masking resist must be thick or else rapid ablation of the masking layer occurs and the desired nitride pattern will be etched and possibly destroyed (Figure 5.30). Lithographic registration error is a critical issue with this process flow, however various precautions were taken (large diffraction grating region, over-sized sacrificial layers) in order to ensure the functionality of the devices. Al was used as the second sacrificial layer for the wafer in Figure 5.29; once again note the graininess of the feature as well as the ill-defined edges.

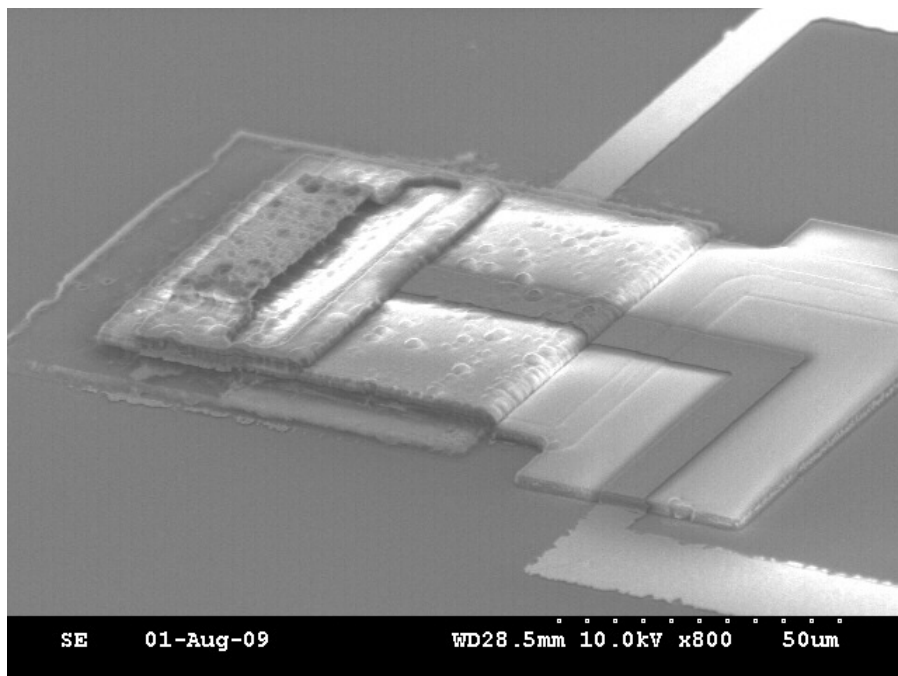


Figure 5.30: SEM Image of Damaged Bridge Sensor

In Figure 5.30 it is apparent that the bridge sensor is roughened due to the lack of PR during the etch step. A clever way to remedy this issue is to pattern Al in the shape of the sensor structures and use this Al layer (along with the PR) as a mask for the SiN_x during RIE; Since Cl gas is not present in the chamber during the etch step, the Al masking layer is unaffected. This method's effectiveness can be seen in Figure 5.31; the bridge structure has well-defined edges and the surface is smooth.

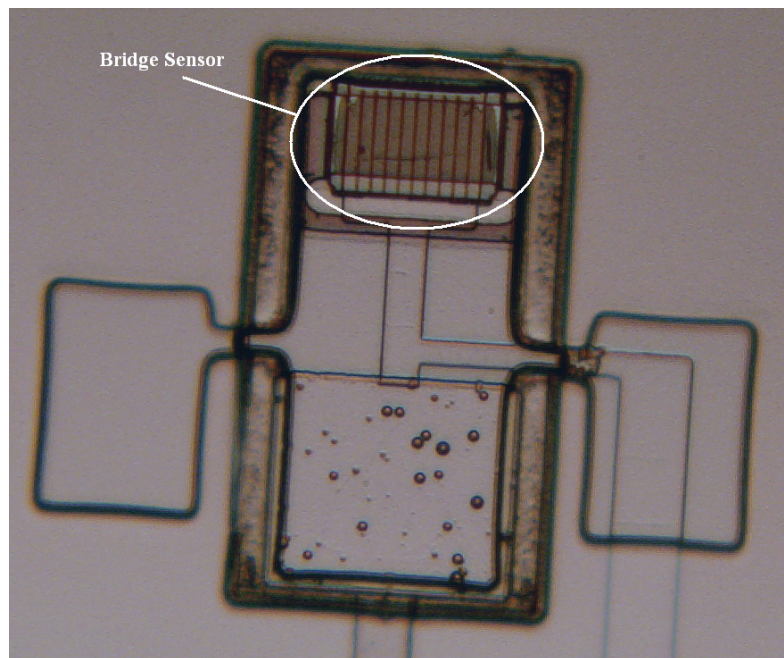


Figure 5.31: Bridge Sensor Etched with Al Masking Layer

Once the sensor structure is patterned, both the PR and the Al masking layer are dissolved exposing the 2000 Angstrom Cr layer. Using SPR 220 resist, the Cr layer is patterned into the third electrode (Figure 5.32). Since Cr is also masked by the sensor structure, it will remain there as a reflective mirror for the incoming HeNe laser light; it also serves as the electrode for AC excitation of sensor resonance if needed.

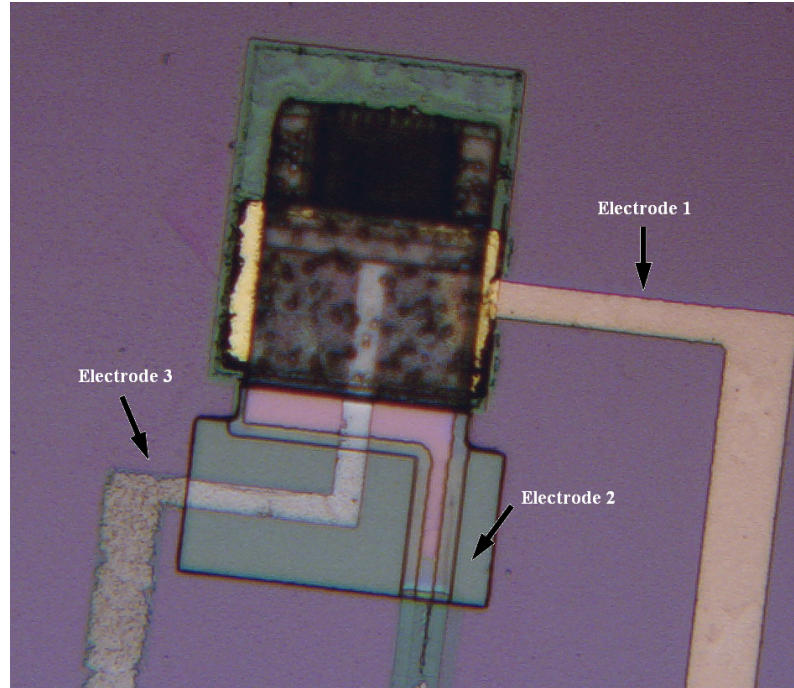


Figure 5.32: Patterned Third Electrode

Sufficient coverage of the stepped features is critical such that electrical contact is maintained. Figure 5.33 is a scanning electron micrograph of ideal Cr-electrode step coverage. The Cr wet-etch has undercut the PR pattern in Figure 5.33, however sufficient contact has been achieved. Also apparent in Figure 5.32 is a drastic undercut of the second electrode due to Cr7s wet-etchant over-exposure.

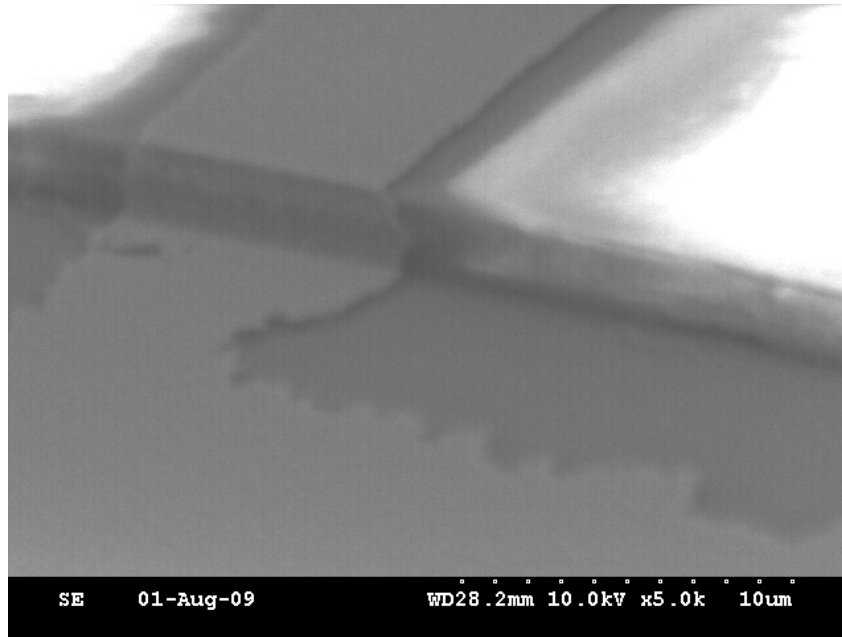


Figure 5.33: Ideal Electrode Step Coverage

5.8 KOH Backside Etching

KOH is not highly selective when an oxide masking layer is involved; recall that approximately one micron of thermal SiO_2 was grown as the first processing step. The etch rate for Si (100) in KOH is approximately 1.4 microns per minute while the etch rate for SiO_2 is approximately 28 Angstroms per minute; a selectivity of 500:1. Thus, an ideal KOH masking layer must be approximately one micron in thickness; however it is very dangerous to push the limitations of a thin masking oxide. With this in mind, an additional 0.5-micron PECVD SiO_2 layer was deposited, followed by a one-micron PECVD SiN_x layer. The etch selectivity of KOH with regards to PECVD SiN_x is greater than 10,000:1 (it is almost infinite with regards to LPCVD SiN_x). Using the EVG mask aligner, the backside patterning was accomplished with very little shift in alignment. KOH etching the (100) Si crystalline plane exposes the (111) crystalline planes at an

inward slope of 54.74° ; thus the backside mask boxes were intentionally designed to be oversized. The SiO_2 and SiN_x layers are next patterned using an ICP etch; this is a highly anisotropic method and preserves the pattern dimensions. The front side of the wafer is spin-coated with ProTEK B3 primer and coating in order to protect the surface-micromachined devices from KOH. The wafer is then submerged into a 75°C KOH bath; this bath is expected to etch the (100) crystalline plane of Si at the documented 1.4 microns per minute (almost 7 hours at best). The total etch time is nominally nine hours in actuality. Figure 5.34 is an optical micrograph of a KOH backside-etched bridge-on-cantilever device.

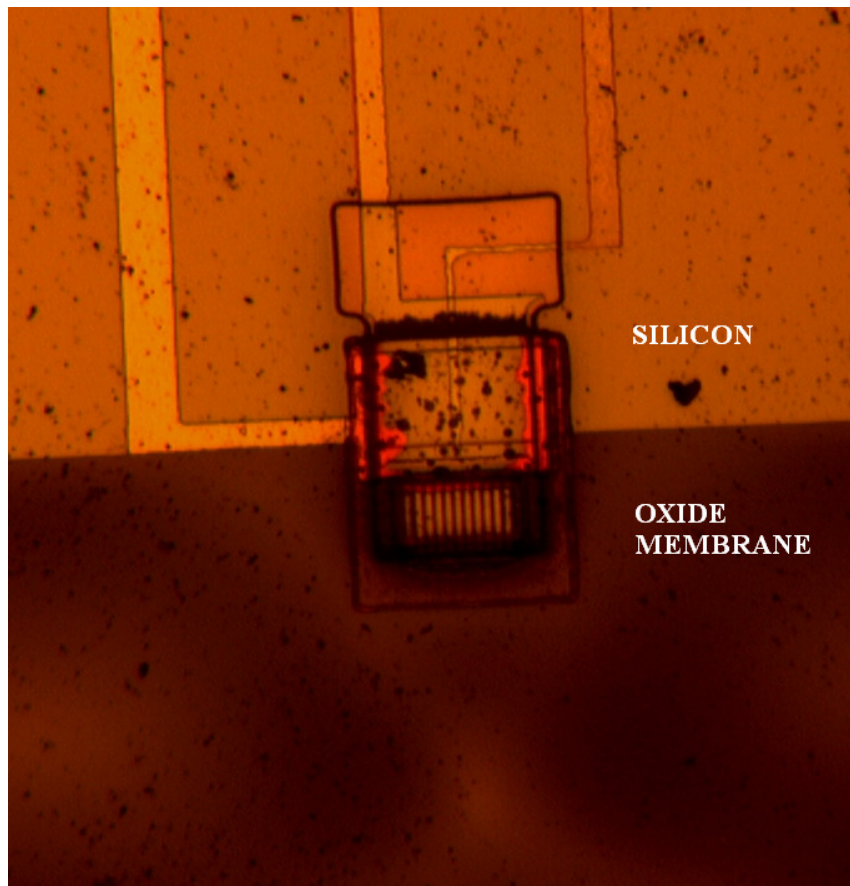
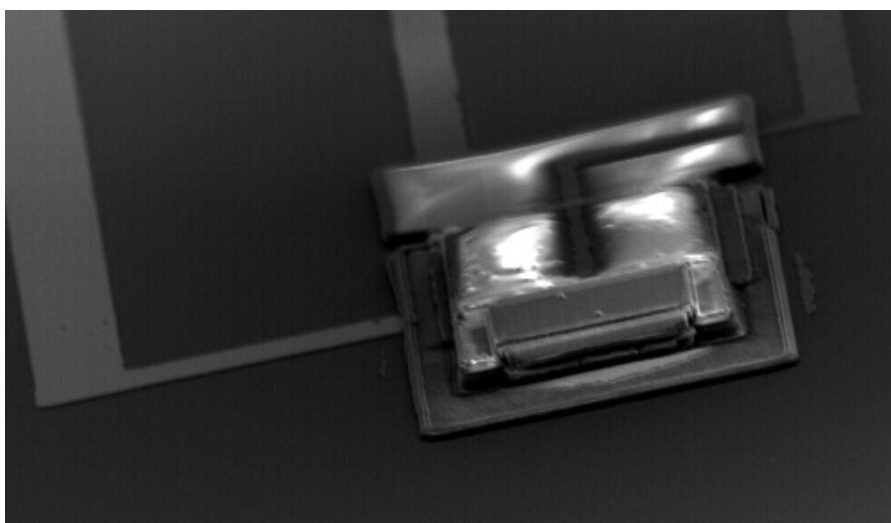


Figure 5.34: KOH Backside-Etched Bridge-on-Cantilever Device

There is evidence of a slight misalignment in Figure 5.34; the KOH opening has receded too far back and has undercut the first electrode. Large variations can occur during KOH etching due to the uncertainty of the wafer thickness (nominally 525 microns +/- 20 microns for a prime wafer).

5.9 Release of Device

The last step before dicing the devices is to remove the thin SiO₂ membrane in the opening left over from the KOH backside etch step; this can be done either with a dry etch method (RIE) or a buffered oxide etch (BOE). Since the ProTEK B3 coating still exists on the front side, it is safe to place the devices in the dicing saw without damaging the structures. After the devices are diced to the specified die-size, the ProTEK B3 coating can be removed in Acetone and further descummed with RIE. Figure 5.35 is a series of SEM images of devices before the sacrificial layer release step.



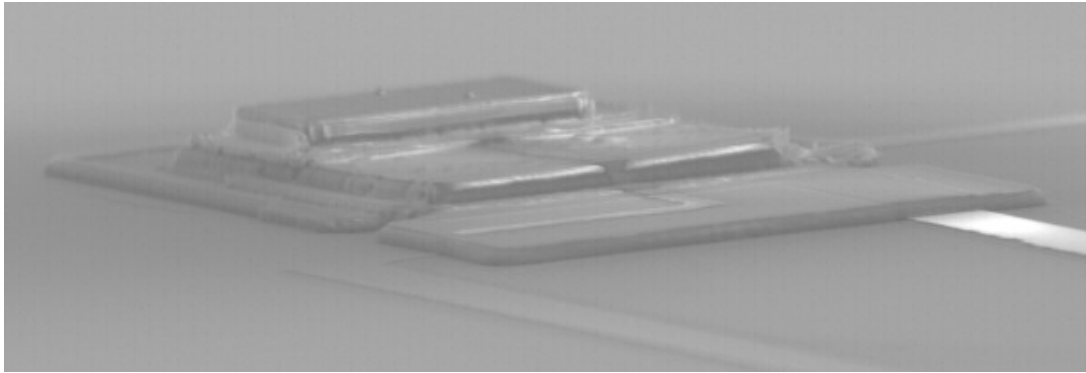
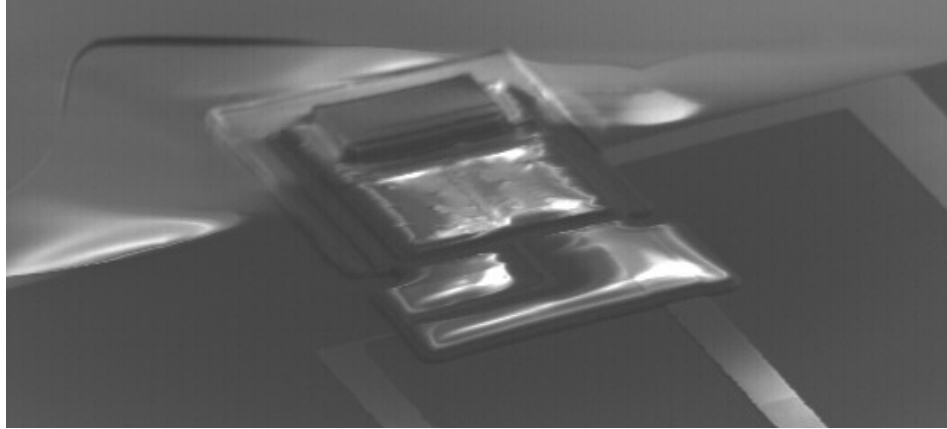


Figure 5.35: Scanning Electron Micrographs of Bridge-on-Cantilever Devices, Pre-Sacrificial Layer Release

The center image in Figure 5.35 depicts cracked oxide membrane remnants from the KOH backside release. The SiN_x features appear shiny due to charging effects from the SEM imaging. In order to remove the sacrificial layers, the devices must be placed in a 2:1 aqueous KOH solution to dissolve the aSi; this step takes considerably less time than the backside etch step (approximately 30 minutes). The backside Si will be exposed during this step, however only the (111) crystalline planes are exposed and are very slowly (if at all) etched by further exposure to KOH. The devices are then transferred to DI water and then to IPA; it is imperative that the sample remain in liquid throughout the

entire release sequence such that stiction does not collapse the devices. Lastly, the IPA is dried at its critical point (to prevent stiction) using a supercritical drying machine. Figure 5.36 is an optical micrograph of a fully released structure.

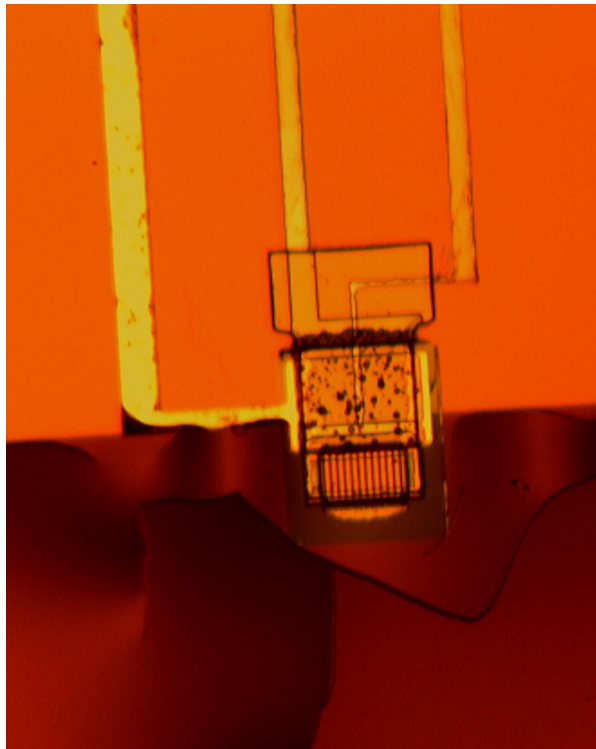


Figure 5.36: Optical Micrograph of Released Bridge-on-Cantilever Device

The device in Figure 5.36 was released without removing the oxide membrane (it appears cracked in the image). It is worthy to note that this fabrication process is still compatible with a Quartz substrate; a backside etch would be unnecessary in this case. It is certainly possible to remedy the critical issues encountered during this fabrication process, such as wet-etching undercut and KOH window misalignment.

CHAPTER 6:

CONCLUSIONS AND FUTURE WORK

Novel AFM probe designs have been analyzed as well as micro-fabricated in this work. The simulated behavior of these structures predicts a broad actuation bandwidth of up to 100 kHz and a sensor fundamental resonance frequency from 750 kHz to 1.2 MHz. The new design alleviates the need for a slow z-axis piezoelectric actuator, similar to the architecture utilized in the second generation FIRAT probes. To remedy the high actuation voltage of the cantilever actuator, the seesaw lever actuator was developed and further simulated to display large range deflection with reduced applied DC bias. The seesaw lever actuator can potentially exhibit micron-range z-axis motion, a much needed improvement from the limited hundred-nanometer actuation range of the previous FIRAT probes. Sensor structures have a simulated stiffness between 15 and 30 N/m while actuator stiffness varies from 23 to 133 N/m. The sensors considered in this work are simulated to have a low equilibrium force-noise of approximately 63 pN for a 100 kHz tapping bandwidth. The actuator structures exhibit a low displacement-noise of approximately 0.63 pm for the same 100 kHz bandwidth. The quality factor was determined to be on the low end for the sensor structures (< 2); however this characteristic can be improved by better manipulating the geometry of the structures.

A component-mode-synthesis code was developed in MATLAB in order to accurately predict the modal frequencies of dual cantilever structures. The code requires very little execution time and computational power, and is accurate in comparison to ANSYS results with less than two percent error.

Micro-fabrication of the devices was successful; a novel surface-micromachining process flow was developed. The selectivity of various materials was determined throughout the test phase of fabrication, enabling a finalized recipe for the device construction. Device thicknesses were tailored such that several combinations are able to be fabricated on a single four-inch Silicon wafer.

Some aspects of this work are yet to be completed, namely the extensive characterization of the fabricated devices. The preliminary characterization will consist of device actuation within a frequency range in order to capture the frequency response via interferometric readout. Thermal-mechanical noise will be determined in a similar fashion. The characterization will take place both in ambient and vacuum conditions in order to validate ANSYS simulations. Basic AFM contact experiments can be executed to determine the stiffness of the sensor cantilevers and bridges.

Once the devices have been characterized with respect to their frequency response, sharp tips will be deposited onto the sensors (using a focused ion beam, or FIB) with the intention of imaging samples at high speed. The fabrication flow will likely migrate to an integrated tip design in order to eradicate the need for FIB deposition; this will ultimately expedite probe fabrication with a substantially more economic approach.

APPENDIX A:

FABRICATION RECIPES

SPR 220 7.0 Positive Photoresist (PR)

- Spin coat PR onto wafer at 4000 rpm with 1000 r/s ramp for 33 seconds
- Soft bake PR for 4 minutes at 115°C
- MA6 Mask aligner
 - o Set to 405 nm wavelength (Channel 2)
 - o Exposure dose (D) of $\sim 470 \text{ mJ/cm}^2$
 - o Measure intensity (I) and adjust exposure time (t) accordingly, $t = D/I$
 - o Vacuum contact, alignment gap set accordingly
- Develop in MF319
- Hard bake for 15 minutes at 120°C

For lift-off process:

- Same recipe as above, NO HARD BAKE

Shipley 1827 Positive PR

- Spin coat PR onto wafer at 4000 rpm with 1000 r/s ramp for 40 seconds (~ 2.7 microns in thickness)
- Soft bake PR for 4 minutes at 100°C
- MA6 Mask aligner
 - o Set to 405 nm wavelength (Channel 2)
 - o Exposure dose (D) of $\sim 270 \text{ mJ/cm}^2$
 - o Measure intensity (I) and adjust exposure time (t) accordingly, $t = D/I$
 - o Vacuum contact, alignment gap set accordingly
- Develop in MF319
- Hard bake for 15 minutes at 110°C

Shipley 1813 Positive PR

- Spin coat PR onto wafer at 4000 rpm with 1000 r/s ramp for 50 seconds (~ 1.3 microns in thickness)
- Soft bake PR for 4 minutes at 100°C
- MA6 Mask aligner
 - o Set to 405 nm wavelength (Channel 2)
 - o Exposure dose (D) of $\sim 135 \text{ mJ/cm}^2$
 - o Measure intensity (I) and adjust exposure time (t) accordingly, $t = D/I$
 - o Vacuum contact, alignment gap set accordingly
- Develop in MF319
- Hard bake for 10 minutes at 115°C

*** All photoresist is stripped using Acetone → Methanol → Isopropanol → deionized (DI) water ***

Unaxis PECVD Silicon Nitride Deposition Recipe (filename: Kia SiN2)

- SiH₄ @ 200 sccm / NH₃ @ 8 sccm / He @ 560 sccm / N₂ @ 150 sccm
- 45 W Power
- 900 mTorr Pressure
- 250°C Deposition Temperature
- Approximately 4000 Angstroms / hr

*** Oxide Deposition (Kia_SiO₂) Approximately 63 nm / min

Vision RIE Silicon Nitride Etch Recipe (filename: Kia SiNx)

- SF₆ @ 50 sccm / O₂ @ 5 sccm
- 200 W RF Power
- 20 mTorr Pressure
- Etch time based on visual inspection

*** *This same recipe used for etching Molybdenum* ***

ICP Amorphous Silicon Etch Recipe / Bosch Process [40]

- Etch
 - o SF₆ @ 130 sccm
 - o 9 Second Active Time
 - o 33 mTorr Pressure
 - o 600 W Coil Power
 - o 15 W Platen Power
 - o 350-400 V Bias
- Passivation
 - o C₄F₈ @ 80 sccm
 - o 8 Second Active Time
 - o ~ 18 mTorr Pressure
 - o 600 W Coil Power
 - o Zero Platen Power and Bias Voltage

*** *A nine-second etch step followed by an eight-second passivation step is considered one cycle* ***

- Etch rate approximately 100 nm / cycle

Type-A Aluminum Wet-Etch Recipe

- ROOM TEMPERATURE, do not heat
- Etch Rate ~ 60 nm / sec

Cr7s Chromium Wet-Etch Recipe

- ROOM TEMPERATURE, do not heat
- DO NOT JOSTLE WAFER
- Etch rate ~ 33 nm / min

ProTEK B3 Protective Coating and Primer

- Primer
 - Spin Speed: 1500 rpm
 - Acceleration: >1000 to 5000 rpm / sec
 - Time: 30 sec
 - Bake at 205°C for 60 sec
- Protective Coating
 - Spin Speed: >1000 rpm (1500 rpm for 7 micron thickness)
 - Acceleration: >5000 rpm / sec
 - Time: 60 sec
 - First Bake: 140°C for 120 sec
 - Second Bake: 205°C for 60 sec

KOH Etch of (100) Si Crystalline Plane

- Solution Temperature: 75°C
- Etch Rate Approximately 1.4 microns per minute
- (111) Crystalline Si Plane Exposed at 54.74°

APPENDIX B:

ANSYS AND MATLAB CODES

VISCOUS DAMPING (MATLAB)

```
%%%%%%%% Code to determine frequency response of actuator %%%%%%%%%
%%%%%%%% and sensor cantilevers while subject to squeeze %%%%%%%%%
%%%%%%%% film damping. Input files are generated by ANSYS %%%%%%%%%
%%%%%%%% fluidic squeeze film damping elements APDL code %%%%%%%%%

%% Rameen Hadizadeh 10.29.2008 %%%%%%%%%%%%%%%
clear

% Units are m-kg-s
% Specs of PECVD Si-Nitride
rho = 2200;
E = 110e9;

% Specs of Air at 15 deg C
nu = 1.78e-5;
Po = 1e5;
kb = 1.3806504e-23;
T = 288;

% Physical actuator parameters
km = 130;
La = 92e-6;
lenA = La*1e6;
Wa = 53.9e-6;
widA = Wa*1e6;
Ha = 2.948e-6;
m = 0.64*La*Wa*Ha*rho;

% Physical sensor parameters
km2 = 15;
Ls = 50e-6;
lenS = Ls*1e6;
Ws = 15.67e-6;
widS = Ws*1e6;
Hs = 1.632e-6;
m2 = 0.24*Ls*Ws*Hs*rho;

%%%%%%%%%%%%%% Actuator %%%%%%%%%%%%%%%

% Actuator Response with dynamic squeeze film damping coefficients

[f,ksfd,bsfdx] = textread('SiN92x54act25g.txt', '%f %f
%f', 'delimiter', ' ');
w = 2.*pi.*f;
```

```

FoX = (km + ksfd) - w.^2.*m + j.*w.*bsfdx;
xferfxn = (FoX).^(-1);
Hjwx = abs(xferfxn);
phase1 = (90/pi)*atan(imag(xferfxn)./real(xferfxn));
dBH = 20.*log10(Hjwx);
semilogx(f,dBH)
title('Sensor and Actuator Transfer Functions');
xlabel('Frequency (Hz)'); ylabel('|H(jw)| dB');
hold;

%%%%%%%%%%%%%% SENSOR %%%%%%%%%%%%%%%

% Sensor Response with dynamic squeeze film damping coefficients

[f2,ksfd2,bsfd2x] = textread('SiN50x16sen40g.txt', '%f %f
%f', 'delimiter', ' ');
w2 = 2.*pi.*f2;
FoX2 = (km2 + ksfd2) - w2.^2.*m2 + j.*w2.*bsfd2x;
xferfxn2 = (FoX2).^(-1);
Hjw2x = abs(xferfxn2);
phase2 = (90/pi)*atan(imag(xferfxn2)./real(xferfxn2));
dBH2 = 20.*log10(Hjw2x);
semilogx(f2,dBH2,'r');
h = legend('Actuator','Sensor',3);
set(h,'Interpreter','none');
figure;

semilogx(f,phase1); hold; semilogx(f,phase2,'r');
h = legend('Actuator','Sensor',2);
set(h,'Interpreter','none');
title('Actuator & Sensor Phase');
xlabel('Frequency (Hz)'); ylabel('Phase (deg)');
figure;

%%%%%%%%%%%%%% Thermal Noise Calculations %%%%%%%%%%%%%%%

% Force noise, actuator
SnFf = 4.*kb.*T.*bsfdx;
subplot(2,1,1);
semilogx(f,sqrt(SnFf)*(1e15),'b')
hold;
% Force noise, sensor
SnFf2 = 4.*kb.*T.*bsfd2x;
semilogx(f,sqrt(SnFf2)*(1e15),'r')
title('Spectral Density of T-M Force Noise');
ylabel('fN/{\surd}Hz');

% Displacement noise, actuator
SnXf = sqrt(SnFf.*(Hjwx.^2));
subplot(2,1,2);
semilogx(f,SnXf.*(1e15),'b');
hold;
% Displacement noise, sensor
SnXf2 = sqrt(SnFf2.*(Hjw2x.^2));
semilogx(f,SnXf2.*(1e15),'r');

```

```

title('Spectral Density of T-M Displacement Noise');
xlabel('Frequency (Hz)'); ylabel('fm/{\surd}Hz');
h = legend('Actuator','Sensor',3);
set(h,'Interpreter','none');

```

COMPONENT MODE SYNTHESIS (MATLAB)

```

% The component mode synthesis of a dual-cantilever structure
% Rameen Hadizadeh / Georgia Institute of Technology
% Spring 2009

```

```
clear
```

```

%%%%%%%%%%%%%%%%%%%%%%%%%%%%%%%%%%%%%%%%%%%%%%%%%%%%%%%%%%%%%%%%%%%%%%%%
% Physical properties of large cantilever
L1 = 92e-6; width1 = 29.02e-6/L1; thick1 = 2.948e-6/L1;
rho = 1; E = 1; % rho and E are same for both cantilevers
A1 = width1*thick1; m1 = A1*rho;
I1 = (1/12)*(width1)*(thick1^3);
%%%%%%%%%%%%%%%%%%%%%%%%%%%%%%%%%%%%%%%%%%%%%%%%%%%%%%%%%%%%%%%%%%%%%%%%

```

```

%%%%%%%%%%%%%%%%%%%%%%%%%%%%%%%%%%%%%%%%%%%%%%%%%%%%%%%%%%%%%%%%%%%%%%%%
% Physical properties of small cantilever
L2 = 50e-6/L1; width2 = 15.67e-6/L1; thick2 = 1.632e-6/L1;
A2 = width2*thick2; m2 = A2*rho;
I2 = (1/12)*(width2)*(thick2^3);
%%%%%%%%%%%%%%%%%%%%%%%%%%%%%%%%%%%%%%%%%%%%%%%%%%%%%%%%%%%%%%%%%%%%%%%%
L1 = 1;
gap = 2.5e-6;

```

```

%%%%%%%%%%%%%%%%%%%%%%%%%%%%%%%%%%%%%%%%%%%%%%%%%%%%%%%%%%%%%%%%%%%%%%%%
% SPECIFY number of normal modes for large cantilever
NL = 10;
%%%%%%%%%%%%%%%%%%%%%%%%%%%%%%%%%%%%%%%%%%%%%%%%%%%%%%%%%%%%%%%%%%%%%%%%

```

```

%%%%%%%%%%%%%%%%%%%%%%%%%%%%%%%%%%%%%%%%%%%%%%%%%%%%%%%%%%%%%%%%%%%%%%%%
% SPECIFY number of extra modes for small cantilever
NE = 2;
%%%%%%%%%%%%%%%%%%%%%%%%%%%%%%%%%%%%%%%%%%%%%%%%%%%%%%%%%%%%%%%%%%%%%%%%

```

```

%%%%%%%%%%%%%%%%%%%%%%%%%%%%%%%%%%%%%%%%%%%%%%%%%%%%%%%%%%%%%%%%%%%%%%%%
% Number of normal modes for small cantilever
NS = NL + (4-NE);
%%%%%%%%%%%%%%%%%%%%%%%%%%%%%%%%%%%%%%%%%%%%%%%%%%%%%%%%%%%%%%%%%%%%%%%%

```

```

% Number of total modes for the system
Nt = NL + NS + NE;

```

```
%%%%%%%%%%%%%%%%%%%%%%%%%%%%%%%%%%%%%%%%%%%%%%%%%%%%%%%%%%%%%%%%%%%%%%%%
```

```

% Large Cantilever %%%
%%%%%%%%%%%%%%%%%%%%%%%%%%%%%%%%%%%%%%%%%%%%%%%%%%%%%%%%%%%%%%%%%%%%%%%%

% Determine eigenvalues of fixed-free cantilever beam (Euler Bernouli)
fn = @(x) cos(x).*cosh(x) + 1;

b1 = fzero(fn,2);
b2 = fzero(fn,4);
b3 = fzero(fn,7);

b4_Nt = (2*(4:Nt)-1)*pi/2;

Lam = [b1 b2 b3 b4_Nt];

% Constant term in eigenfunction
for i = 1:Nt
    TE(i) = (cosh(Lam(i))+cos(Lam(i)))/(sinh(Lam(i)) + sin(Lam(i)));
end

% Evaluate eigenfunctions for x1 = 0 to L1 with 1/1000 resolution using
% a change of variables where z1 = x1/L1

x1 = linspace(0,L1,1000);
z1 = x1/L1;
Lz1 = length(z1);
Pm1 = zeros(NL,Lz1);
Pmpp1 = Pm1;
for i = 1:NL;
    Pm1(i,:) = cosh(Lam(i)*z1) - cos(Lam(i)*z1) -
    TE(i)*(sinh(Lam(i)*z1)-sin(Lam(i)*z1));
    Pmpp1(i,:) = cosh(Lam(i)*z1) + cos(Lam(i)*z1) -
    TE(i)*(sinh(Lam(i)*z1) + sin(Lam(i)*z1));
    Pmpp1(i,:) = Pmpp1(i,)*(Lam(i)^2)/(L1^2);
end
=====
==

% Rigid Body and Constraint Modes are Non-Existent for large cantilever

% Mass Matrix (M1)
for i = 1:NL;
    for j = 1:NL;
        mass1 = Pm1(i,).*Pm1(j,:);
        M1(i,j) = rho*A1*trapz(x1,mass1);
    end
end

% Stiffness Matrix (K1)
for i = 1:NL;
    for j = 1:NL;
        stiff1 = Pmpp1(i,).*Pmpp1(j,:);
        K1(i,j) = E*I1*trapz(x1,stiff1);
    end
end

```

```

%%%%%%%%%%%%%%%%%%%%%%%%%%%%%%%%%%%%%%%%%%%%%%%%%%%%%%%%%%%%%%%%%%%%%%%%
% Smaller Cantilever %%%%%%%%%
%%%%%%%%%%%%%%%%%%%%%%%%%%%%%%%%%%%%%%%%%%%%%%%%%%%%%%%%%%%%%%%%%%%%%%%%

% Evaluate eigenfunctions for x2 = 0 to L2 with 1/1000 resolution using
% a change of variables where z2 = x2/L2

x2 = linspace(0,L2,1000);
z2 = x2/L2;
Lz2 = length(z2);
Pm2 = zeros(NS+NE,Lz2);
Pmpp2 = Pm2;
for i = 1:NS;
    Pm2(i,:) = cosh(Lam(i)*z2) - cos(Lam(i)*z2) -
    TE(i)*(sinh(Lam(i)*z2)-sin(Lam(i)*z2));
    Pmpp2(i,:) = cosh(Lam(i)*z2) + cos(Lam(i)*z2) -
    TE(i)*(sinh(Lam(i)*z2) + sin(Lam(i)*z2));
    Pmpp2(i,:) = Pmpp2(i,)*(Lam(i)^2)/(L2^2);
end
=====
==

% RGB modes
Pm2(NS+1,:) = 1; Pm2(NS+2,:) = x2;
Pmpp2(NS+1,:) = 0; Pmpp2(NS+2,:) = 0;

% Constraint modes
%Pm2(NS+3,:) = (3*((L2-x2).^2)/(L2^2)-(2*((L2-x2).^3)/(L2^3));
%Pmpp2(NS+3,:) = (6/(L2^2))-12*((L2-x2)/(L2^3));
%Pm2(NS+4,:) = L2*((-(L2-x2).^2)/(L2^2))+((L2-x2).^3/(L2^3));
%Pmpp2(NS+4,:) = -(2/L2)+6*((L2-x2)/(L2^2));

% Mass Matrix (M2)
% Since rigid body and constraint modes are present for
% the small cantilever, there will be non-zero entries
% away from the diagonal

for i = 1:NS+NE;
    for j = 1:NS+NE;
        mass2 = Pm2(i,).*Pm2(j,);
        M2(i,j) = rho*A2*trapz(x2,mass2);
    end
end

% Stiffness Matrix (K2)
% Since rigid body and constraint modes are present for
% the small cantilever, there will be non-zero entries
% away from the diagonal

for i = 1:NS+NE;
    for j = 1:NS+NE;
        stiff2 = Pmpp2(i,).*Pmpp2(j,);
        K2(i,j) = E*I2*trapz(x2,stiff2);
    end
end
end

```

```

% Assemble Disjoint Set
Md = blkdiag(M1,M2);
Kd = blkdiag(K1,K2);

%%%%%%%%%%%%%%%%%%%%%%%%%%%%%%%%%%%%%%%%%%%%%%%%%%%%%%%%%%%%%%%%%%%%%%%%
% Eliminate 2 Coefficients %
%%%%%%%%%%%%%%%%%%%%%%%%%%%%%%%%%%%%%%%%%%%%%%%%%%%%%%%%%%%%%%%%%%%%%%%%

% Evaluate large cantilever eigenfunctions (and first derivatives) at
x1 = p
p1 = (L1 - L2)/L1;
for i = 1:NL;
    WLp(i) = cosh(Lam(i)*p1) - cos(Lam(i)*p1) -TE(i)*(sinh(Lam(i)*p1)-
sin(Lam(i)*p1));
    dWLp(i) = sinh(Lam(i)*p1) + sin(Lam(i)*p1) -TE(i)*(cosh(Lam(i)*p1)
- cos(Lam(i)*p1));
    dWLp(i) = dWLp(i)*Lam(i)/L1;
end

% Evaluate small cantilever eigenfunctions at z2 = 0
p2 = 0;
for i = 1:NS;
    WSp(i) = cosh(Lam(i)*p2) - cos(Lam(i)*p2) -TE(i)*(sinh(Lam(i)*p2)-
sin(Lam(i)*p2));
    dWSp(i) = sinh(Lam(i)*p2) + sin(Lam(i)*p2) -TE(i)*(cosh(Lam(i)*p2)
- cos(Lam(i)*p2));
    dWSp(i) = dWSp(i)*Lam(i)/L2;
end

WSp(NS+1) = 1;
dWSp(NS+1) = 0;
WSp(NS+2) = 0;
dWSp(NS+2) = 1;
%WSp(NS+3) = 1;
%dWSp(NS+3) = 0;
%WSp(NS+4) = 0;
%dWSp(NS+4) = -1;

% Choose to eliminate a1 and a2
for j = 1:NL-2;
    Q(1,j) = WLp(j+2);
end
for j = NL-1:Nt - 2;
    Q(1,j) = -WSp(j-(NS-4));
end
for j = 1:NL-2;
    Q(2,j) = dWLp(j+2);
end
for j = NL-1:Nt - 2;
    Q(2,j) = -dWSp(j-(NS-4));
end

C(1,1) = -WLp(1); C(1,2) = -WLp(2);

```

```

C(2,1) = -dWLp(1); C(2,2) = -dWLp(2);

R = inv(C)*Q;

% Fill B matrix with appropriate partitions

for i = 1:2;
    for j = 1:Nt - 2;
        B(i,j) = R(i,j);
    end
end
% Fill the remainder with the identity matrix
for i = 3:Nt;
    for j = 1:Nt - 2;
        if (i-2) == j;
            B(i,j) = 1;
        else B(i,j) = 0;
        end
    end
end

% Final Mass / Stiffness Matrices
Mfinal = B.'*Md*B;
Kfinal = B.'*Kd*B;

%%%%%%%%%%%%%%%%%%%%%%%%%%%%%%%%%%%%%%%%%%%%%%%%%%%%%%%%%%%%%%%%%%%%%%%%
% Solve eigenvalue problem, extract modes %
[V,D] = eig(Kfinal,Mfinal);
lambda = diag(D);
E = 110e9; rho = 2200; L1 = 92e-6;
scaling = sqrt(E/rho)/L1;
frequencies = sort((sqrt(lambda)*scaling)./(2*pi))
[new_lambda,Isort] = sort(lambda);

%%%%%%%%%%%%%%%%%%%%%%%%%%%%%%%%%%%%%%%%%%%%%%%%%%%%%%%%%%%%%%%%%%%%%%%%
% Pick Rth mode (1 through Nt) to plot
pick = 1;
%%%%%%%%%%%%%%%%%%%%%%%%%%%%%%%%%%%%%%%%%%%%%%%%%%%%%%%%%%%%%%%%%%%%%%%%

R = Isort(pick);
% Recover eliminated coordinates
a1_a2 = inv(C)*Q*V(:,R);
VR = vertcat(a1_a2, V(:,R));
% Plot Rth mode of large cantilever
x1 = linspace(0,L1,1000);
phiL = Pm1(1:NL,:)'*VR(1:NL);
figure(1)
plot(x1*(1e6),phiL,'linewidth',2)
hold
% Plot Rth mode of small cantilever
L2 = L2*L1;
x2 = linspace(0,L2,1000);
phiS = (Pm2(1:NS+NE,:)'*VR(NL+1:Nt));

```

```

plot((x2+(L1-L2))*(1e6),phiS,'r','linewidth',2)

title(['System Modeshapes (Mode #',num2str(pick),')'])
xlabel('Length (microns)')
ylabel('Amplitude (a.u.)')

```

HeNe LASER DIFFRACTION INTENSITY MODULATION (MATLAB)

```

% Estimation of the modulation of diffracted 0th and
% 1st order HeNe laser intensity
% Rameen Hadizadeh / Georgia Tech 2009

clear;

Lambda = 635e-9;
do = linspace(3e-6,5e-6,100);
Iin = 3e-3;
num = 2*pi*do;
arg1 = cos(num./Lambda);
arg2 = sin(num./Lambda);
Iout0 = Iin*(arg1.^2);
Iout1 = (4/(pi^2))*Iin*(arg2.^2);
plot(do*(1e6),Iout0*(1e3))
hold
plot(do*(1e6),Iout1*(1e3),'r')
xlabel('Gap (microns)');
ylabel('Intensity (mW)');
title('Modulation of Diffracted Intensity as a Function of Gap');
legend('0th-order','1st-order');

```

PULL-IN VOLTAGE ANALYSIS (MATLAB)

```

% MATLAB code to determine the pull-in voltages
% of a fixed-free beam of varying widths
% Vpi1 is adapted from Pamidighantam et al.
% Vpi2 is adapted from Chowdhury et al.

% Rameen Hadizadeh

clear;

h = 2.948e-6;
L = 92e-6;
b = linspace(20e-6,80e-6,1000);
E = 110e9/(1-0.24^2);
lambdaR = 1;

```

```

do = 2.5e-6;
beta = 0.33;
Eo = 8.854e-12;

% Pamidighantam

beff = b.*(1+0.65*((1-beta)*do)./b);
Keff = (2/3)*((E*b*(h^3))./(L^3))*(3/(8-6*lambdaR+lambdaR^3));
Vpil = sqrt((8*Keff*(do^3))./(18.2*Eo*L*beff));

plot(b*1e6,Vpil); hold;

%[AX,H1,H2] = plotyy(b*(1e6),Vpil,b*(1e6),Keff)
%set(get(AX(1),'ylabel'),'string','Pull-in Voltage (V)')
%set(get(AX(2),'ylabel'),'string','Stiffness (N/m)')
xlabel('Width (microns)');
%title('Pull-in Voltage and Stiffness of a Cantilever (L = 92
microns)');
ylabel('Pull-in Voltage (V)');
title('Pull-in voltage of a fixed-free beam under uniform electrostatic
force');

% Chowdhury

f0 = 8.37*Eo*(L^4);
f1 = 5/(6*(do^2));
f2 = 0.19./((do^1.25)*(b.^0.75));
f3 = 0.19./((do^1.25)*(L^0.75));
f4 = (0.4*(h^0.5))./((do^1.5).*b);

num = 2*E*(h^3)*do;

Vpi2 = sqrt(num./(f0*(f1+f2+f3+f4)));

plot(b*1e6,Vpi2,'r')

h = legend('Pamidighantam et al.','Chowdhury et al.',4);
set(h,'Interpreter','none');

figure
plot(b*1e6,Keff);
xlabel('Width (microns)');
ylabel('Stiffness (N/m)')
title('Stiffness of a fixed-free beam with uniform distributed
electrostatic load')
hold;
plot(29.02,70,'or');
plot(53.9,130,'or');
plot(74.36,180,'or');

h = legend('Pamidighantam et al.','ANSYS',4);
set(h,'Interpreter','none');

```

HARMONIC ANALYSIS (MATLAB)

```
%% Rameen Hadizadeh 7.6.2009 %%%%%%%%%%%%%%%%%%%%%%%%%%%%%%%%%%%%%%%%%%%%%%%%%%%%%%%%%%%%%%%%%%%%%%%%%%
clear

%%% SENSOR PATH DATA %%%
SENnodes = 9; % number of nodes chosen on sensor path

[f,amp,phase] = textread('A9C3node1.txt', '%f %f %f','delimiter',' ');
H = abs(amp);
dBH = 20.*log10(H);

[f2,amp2,phase2] = textread('A9C3node2.txt', '%f %f %f','delimiter',' ');
H2 = abs(amp2);
dBH2 = 20.*log10(H2);

[f3,amp3,phase3] = textread('A9C3node3.txt', '%f %f %f','delimiter',' ');
H3 = abs(amp3);
dBH3 = 20.*log10(H3);

[f4,amp4,phase4] = textread('A9C3node4.txt', '%f %f %f','delimiter',' ');
H4 = abs(amp4);
dBH4 = 20.*log10(H4);

[f5,amp5,phase5] = textread('A9C3node5.txt', '%f %f %f','delimiter',' ');
H5 = abs(amp5);
dBH5 = 20.*log10(H5);

[f6,amp6,phase6] = textread('A9C3node6.txt', '%f %f %f','delimiter',' ');
H6 = abs(amp6);
dBH6 = 20.*log10(H6);

[f7,amp7,phase7] = textread('A9C3node7.txt', '%f %f %f','delimiter',' ');
H7 = abs(amp7);
dBH7 = 20.*log10(H7);

[f8,amp8,phase8] = textread('A9C3node8.txt', '%f %f %f','delimiter',' ');
H8 = abs(amp8);
dBH8 = 20.*log10(H8);

[f9,amp9,phase9] = textread('A9C3node9.txt', '%f %f %f','delimiter',' ');
H9 = abs(amp9);
dBH9 = 20.*log10(H9);
```

```

%%% ACTUATOR PATH DATA %%%
ACTnodes = 9; % Number of nodes chosen on actuator path

[f10,amp10,phase10] = textread('A9C3node10.txt', '%f %f
%f','delimiter',' ');
H10 = abs(amp10);
dBH10 = 20.*log10(H10);

[f11,amp11,phase11] = textread('A9C3node11.txt', '%f %f
%f','delimiter',' ');
H11 = abs(amp11);
dBH11 = 20.*log10(H11);

[f12,amp12,phase12] = textread('A9C3node12.txt', '%f %f
%f','delimiter',' ');
H12 = abs(amp12);
dBH12 = 20.*log10(H12);

[f13,amp13,phase13] = textread('A9C3node13.txt', '%f %f
%f','delimiter',' ');
H13 = abs(amp13);
dBH13 = 20.*log10(H13);

[f14,amp14,phase14] = textread('A9C3node14.txt', '%f %f
%f','delimiter',' ');
H14 = abs(amp14);
dBH14 = 20.*log10(H14);

[f15,amp15,phase15] = textread('A9C3node15.txt', '%f %f
%f','delimiter',' ');
H15 = abs(amp15);
dBH15 = 20.*log10(H15);

[f16,amp16,phase16] = textread('A9C3node16.txt', '%f %f
%f','delimiter',' ');
H16 = abs(amp16);
dBH16 = 20.*log10(H16);

[f17,amp17,phase17] = textread('A9C3node17.txt', '%f %f
%f','delimiter',' ');
H17 = abs(amp17);
dBH17 = 20.*log10(H17);

[f18,amp18,phase18] = textread('A9C3node18.txt', '%f %f
%f','delimiter',' ');
H18 = abs(amp18);
dBH18 = 20.*log10(H18);

L = length(f)
for i = 1:L;
node1(i) = 1;
end
for i = 1:L;
node2(i) = 2;
end

```

```

for i = 1:L;
node3(i) = 3;
end
for i = 1:L;
node4(i) = 4;
end
for i = 1:L;
node5(i) = 5;
end
for i = 1:L;
node6(i) = 6;
end
for i = 1:L;
node7(i) = 7;
end
for i = 1:L;
node8(i) = 8;
end
for i = 1:L;
node9(i) = 9;
end

for i = 1:L;
node10(i) = 10;
end
for i = 1:L;
node11(i) = 11;
end
for i = 1:L;
node12(i) = 12;
end
for i = 1:L;
node13(i) = 13;
end
for i = 1:L;
node14(i) = 14;
end
for i = 1:L;
node15(i) = 15;
end
for i = 1:L;
node16(i) = 16;
end
for i = 1:L;
node17(i) = 17;
end
for i = 1:L;
node18(i) = 18;
end
for i = 1:L;
node19(i) = 19;
end

plot3(node1, f, H, node2, f, H2, node3, f, H3, node4, f, H4, node5, f, H5, node6, f, H6,
node7, f, H7, node8, f, H8, node9, f, H9, 'linewidth', 2);
grid on

```

```

xlabel('node');ylabel('Frequency (Hz)');zlabel('displacement (a.u.)');
title('Frequency response along sensor node path');
figure

plot3(node10,f,H10,node11,f,H11,node12,f,H12,node13,f,H13,node14,f,H14,
node15,f,H15,node16,f,H16,node17,f,H17,node18,f,H18,'linewidth',2);
grid on
xlabel('node');ylabel('Frequency (Hz)');zlabel('displacement (a.u.)');
title('Frequency response along actuator node path');
figure

%%% SENSOR
x1 = linspace(1,SENnodes,SENnodes);
pks1 = findpeaks(H)
pks2 = findpeaks(H2)
pks3 = findpeaks(H3)
pks4 = findpeaks(H4)
pks5 = findpeaks(H5)
pks6 = findpeaks(H6)
pks7 = findpeaks(H7)
pks8 = findpeaks(H8)
pks9 = findpeaks(H9)

SENmodel = [pks1(1) pks2(1) pks3(1) pks4(1) pks5(1) pks6(1) pks7(1)
pks8(1) pks9(1)];
SENmode2 = [pks1(2) pks2(2) pks3(2) pks4(2) pks5(2) pks6(2) pks7(2)
pks8(2) pks9(2)];

%%% ACTUATOR
x2 = linspace(SENnodes+1,SENnodes+ACTnodes,ACTnodes);
pks10 = findpeaks(H10)
pks11 = findpeaks(H11)
pks12 = findpeaks(H12)
pks13 = findpeaks(H13)
pks14 = findpeaks(H14)
pks15 = findpeaks(H15)
pks16 = findpeaks(H16)
pks17 = findpeaks(H17)
pks18 = findpeaks(H18)

ACTmodel = [pks10(1) pks11(1) pks12(1) pks13(1) pks14(1) pks15(1)
pks16(1) pks17(1) pks18(1)];
ACTmode2 = [pks10(2) pks11(2) pks12(2) pks13(2) pks14(2) pks15(2)
pks16(2) pks17(2) pks18(2)];

% Plot relative displacements
plot(x1,SENmodel,'linewidth',3)
hold
plot(x1,ACTmodel,'x-')
plot(x1,SENmode2,'r','linewidth',3)
plot(x1,ACTmode2,'x-r')

xlabel('node');ylabel('displacement (a.u.)');title('Relative
displacement of sensor and actuator');

```

```

h = legend('mode 1: sensor', 'mode 1: actuator', 'mode 2: sensor', 'mode
2: actuator', 2);
set(h, 'Interpreter', 'none');

```

WIDTH AND THICKNESS CALCULATIONS (MATLAB)

```

%%% CODE TO DETERMINE WIDTH AND THICKNESS OF A %%%
%%% CANTILEVER BEAM WITH RESPECT TO DESIRED %%%
%%% RESONANCE FREQUENCY AND SPRING CONSTANT %%%

% Rameen Hadizadeh / Georgia Inst. of Tech.

clear

fo = 400e3;           % Desired natural frequency (Hz)
fot = fo/1000;
kf = 70;             % Desired spring constant (N/m)
E = 110e9;           % Material elastic modulus (Pa)
rho = 2200;          % Material density (Kg/m^3)

h2T014 = (((2*pi*fo)^2)*3*0.64*rho)/(2*E);

w13 = (kf*3/(2*E))/((sqrt(h2T014))^3);

Length = 60e-6:0.1e-6:150e-6;    % length range (m)
w = (w13./(Length.^3)).*(1e6);    % Determine width in relation to
length

thickness = (Length.^2).*sqrt(h2T014); % Determine thickness

[AX,H1,H2] = plotyy(Length*(1e6),w,Length*(1e6),thickness*(1e6))
set(get(AX(1), 'ylabel'), 'string', 'Width (um)')
set(get(AX(2), 'ylabel'), 'string', 'Thickness (um)')
xlabel('Length (microns)');
title(['Necessary parameters for actuator fo = ', num2str(fot), 'kHz, k =
', num2str(kf), 'N/m']);

```

FORCING / STATIC ANALYSIS (ANSYS)

```

finish
/clear

/title, Spring constant check (tip-load)

```

```

/prep7

ET,1,SHELL43          ! Define SHELL43 as element type 1

MP,EX,1,110e9
MP,DENS,1,2200
MP,NUXY,1,.3

w1 = 29.02e-6
l1 = 92e-6
t1 = 2.984e-6

K,1,0,0                ! Define keypoint 1 at
K,2,w1,0               ! Define keypoint 2 at
K,3,w1,l1              ! Define keypoint 3 at
K,4,0,l1,0            ! Define keypoint 4 at

LSTR,1,2
LSTR,2,3
LSTR,3,4
LSTR,4,1
AL,1,2,3,4
R,t1,t1,t1,t1

ASEL,S,AREA,,1
TYPE,1
ESIZE,,10
AMESH,ALL

/VIEW,,1,1,1
/ANGLE,1
/REPLOT
EPLOT
FINISH
/SOLU

ANTYPE,STATIC
nset,s,node,,27
F,ALL,FZ,-1

LSEL,S,LINE,,1
DL,ALL,,ALL

ALLSEL

SOLVE

```

```
FINISH

/POST1
/EFACET,1
PLNSOL, U,SUM, 0,1.0
```

MODAL ANALYSIS (ANSYS)

```
finish
/clear

/title, Dual Cantilever Modal Analysis
/prep7

ET,1,SOLID95                ! Define SOLID95 as element type 1

MP,EX,1,110e9
MP,DENS,1,2200
MP,NUXY,1,.3

t1 = 2.948e-6
w1 = 29.02e-6
l1 = 92e-6

t2 = 4e-6
w2 = 15.67e-6
l2 = 1.632e-6

t3 = 12
w3 = w2
l3 = l2 + 50e-6

o1 = l1 - l3
o2 = (w1-w2)/2

!!!!!!!!!!!!!! vOLUME 1 !!!!!!!!!!!!!!!

K,1,0,0,0
K,2,W1,0,0
K,3,W1,L1,0
K,4,0,L1,0
K,5,0,0,-T1
K,6,W1,0,-T1
```

K,7,W1,L1,-T1
K,8,0,L1,-T1

LSTR,1,2
LSTR,2,3
LSTR,3,4
LSTR,4,1
LSTR,5,6
LSTR,6,7
LSTR,7,8
LSTR,8,5
LSTR,1,5
LSTR,2,6
LSTR,3,7
LSTR,4,8

AL,1,2,3,4
AL,5,6,7,8
AL,9,1,10,5
AL,10,2,11,6
AL,11,3,7,12
AL,12,4,8,9

VA,1,2,3,4,5,6

!!!!!!!!!!!!!! vOLUME 2 !!!!!!!!!!!!!!!

K,9,O2,O1,T2
K,10,o2+W2,O1,T2
K,11,O2+W2,O1+L2,T2
K,12,O2,O1+L2,T2
K,13,O2,O1,0
K,14,O2+W2,O1,0
K,15,O2+W2,O1+L2,0
K,16,O2,O1+L2,0

LSTR,9,10
LSTR,10,11
LSTR,11,12
LSTR,12,9
LSTR,13,14
LSTR,14,15
LSTR,15,16
LSTR,16,13
LSTR,9,13
LSTR,10,14

LSTR,11,15
LSTR,12,16

AL,13,14,15,16
AL,17,18,19,20
AL,21,13,22,17
AL,22,14,23,18
AL,23,15,19,24
AL,24,16,21,20

VA,7,8,9,10,11,12

!!!!!!!!!! VOLUME 3 !!!!!!!!!!!!!!!

K,17,O2,O1,T2+T3
K,18,O2+W3,O1,T2+T3
K,19,O2+W3,O1+L3,T2+T3
K,20,O2,O1+L3,T2+T3
K,21,O2,O1,T2
K,22,O2+W3,O1,T2
K,23,O2+W3,O1+L3,T2
K,24,O2,O1+L3,T2

LSTR,17,18
LSTR,18,19
LSTR,19,20
LSTR,20,17
LSTR,21,22
LSTR,22,23
LSTR,23,24
LSTR,24,21
LSTR,17,21
LSTR,18,22
LSTR,19,23
LSTR,20,24

AL,25,26,27,28
AL,29,30,31,32
AL,33,25,34,29
AL,34,26,35,30
AL,35,27,36,31
AL,36,28,33,32

VA,13,14,15,16,17,18

!!!!!! Stitch volumes together to make one solid structure !!!!!!!

```

VADD,1,2,3

VSEL,ALL          ! Select volume
SMRT,8           ! smart-size (10 = coarse, 1 = fine)
MSHAPE,1,3D      ! Tetrahedral, 3D mesh
MSHKEY,0         ! Free mesh
VMESH,ALL        ! Mesh ALL

/VIEW,,1,0,0
/ANGLE,1
/REPLOT
EPLOT
FINISH
/SOLU

ANTYPE,MODAL      ! Choose modal analysis type
MODOPT,SUBSP,5   ! Choose the subspace mode-extraction method, extracting
5 modes

DA,3,ALL          ! Constrain all degrees of freedom (left - side)

ALLSEL
MXPAND,5
SOLVE
FINISH

/POST1
SET,LIST,2
SET,FIRST
PLDISP,0
ANMODE,10,.5E-1  ! Animate Mode # 1

FINISH

```

ELECTROSTATIC ANALYSIS (ANSYS)

```

finish
/clear

/title, Dual Cantilever Electrostatic Analysis using ANSYS Multiphysics
/prep7

```

```

ET,1,SOLID95      ! Structural Domain
ET,2,SOLID122     ! Electrostatic Domain

VDC = 200         !Applied voltage (Volt)

MP,PERX,2,1       ! Relative permittivity of air

agap=2.5e-6       !Air gap

t1 = 2.948e-6     ! Thickness of act
w1 = 29.02e-6     ! Width of act
l1 = 92e-6        ! Length of act

t2 = 4e-6         ! Act / sen gap
w2 = 15e-6        ! Width of sen
l2 = 1.632e-6     ! Thickness of sen

t3 = l2
w3 = w2
l3 = l2 + 50e-6   ! Length of sen

o1 = l1 - l3      ! y-pos of sen
o2 = (w1-w2)/2    ! centering sen

!!!!!!!!!!!!!! vOLUME 1 !!!!!!!!!!!!!!!
BLOCK, 0,w1,0,l1, 0,-t1      ! Create act

!!!!!!!!!!!!!! vOLUME 2 !!!!!!!!!!!!!!!
!BLOCK, o2,o2+w2,o1,o1+l2, -t1,t2+t3      ! Create spacer between sen/act

!!!!!!!!!!!!!! VOLUME 3 !!!!!!!!!!!!!!!
!BLOCK,o2,o2+w3,o1,o1+l3,t2,t2+t3      ! Create sen

!!!!!!!!!!!!!! AIR !!!!!!!!!!!!!!!
BLOCK,0,w1,0,l1-40e-6,-t1,-t1-agap! Create air gap

!!!!!!!!!! Stitch volumes together to make one solid structure !!!!!!!!!!!
VSEL,ALL
!VOVLAP,ALL          !Overlaps volumes
VGLUE,ALL

VSEL,S,LOC,Z,-t1,-t1-agap      ! Select volume for air
CM,AIR,VOLU                    !give a name to this volume (AIR)

```

```

VATT,2,,2                                !define air volume as element 2 with material
properties of 2

!!!!!! Mesh Structure

!VSEL,S,LOC,Z,-t1,t2+t3                    ! Select solid structure volumes
VSEL,S,LOC,Z,-t1,0
MSHAPE,1,3D                                ! Tetrahedral meshing
VMESH,ALL                                    ! Mesh ALL

CMSEL,S,AIR,VOLU                            ! Select air volume
MSHAPE,1,3D                                ! Mesh air gap with triangle shaped elements
VMESH,ALL

CMSEL,S,AIR,VOLU
NSLV,R,1                                    !Select nodes associated with volumes
NSEL,R,LOC,Z,-t1                            !Define top electrode as the top nodes of the air
volume
CM,COND1,NODE
D,ALL,VOLT,VDC                                ! Apply VDC voltage (DC)

ALLSEL

CMSEL,S,AIR,VOLU
NSLV,R,1                                    !Select nodes associated with volumes
NSEL,R,LOC,Z,-t1-agap                       !Define ground electrode as the bottom nodes of the
air volume
CM,COND2,NODE
D,ALL,VOLT,0                                ! Apply VDC voltage (GND)

ALLSEL

ET,1,0

PHYSICS,WRITE,ELECTROS    ! Write electrostatic physics file
PHYSICS,CLEAR

!!!!!!!!!!!!!!!!!!!!!!!!!!!!!!!!!!!!!!!!!!!!!!
!!!!!!!!!! MECHANICAL DOMAIN !!!!!!!!!!!!!!!!!!!!!
!!!!!!!!!!!!!!!!!!!!!!!!!!!!!!!!!!!!!!!!!!!!!!

ET,1,SOLID95                                ! Define SOLID95 as element type 1
ET,2,0

MP,EX,1,110e9

```

```

MP,DENS,1,2200
MP,NUXY,1,.24

ALLSEL
NSEL,S,LOC,Y,0      ! Beam is fixed at the end
!NSEL,R,LOC,Z,-t1,t2+t3
NSEL,R,LOC,Z,-t1,0
D,ALL,UX,0
D,ALL,UY,0
D,ALL,UZ,0

ALLSEL
FINISH
PHYSICS,WRITE,STRUCTURE  ! Write structural physics file

ESSOLV,'ELECTROS','STRUCTURE',3,0,'AIR',,,,10
FINISH

/PREP7
PHYSICS,READ,STRUCTURE  !Read structural physics file
FINISH
/POST1
SET,FIRST
PLNSOL, U,SUM, 0,1.0    ! Show displacements

/EOF !End of file

```

VISCOUS DAMPING (ANSYS)

```

FINISH
/CLEAR,NOSTART
/BATCH,LIST
/PREP7
/TITLE, DAMPING AND SQUEEZE FILM STIFFNESS CALCULATIONS FOR A
CANTILEVER
/COM  UMKS UNITS

ET, 1,136,1          ! 4-NODE OPTION, HIGH KNUDSEN NUMBER

D_EL=2.5E-6          ! GAP
PAMB=1E5             ! AMBIENT PRESSURE (PA)
VISC=1.78E-5         ! VISCOSITY KG/(M)(S)
VELO=2E-3            ! ARBITRARY VELOCITY (M/S)

```

```

PI=3.14159
MFP=68E-9           ! MEAN FREE PATH (M)
KNUD=MFP/D_EL      ! KNUDSEN NUMBER
PREF=1E5           ! REFERENCE PRESSURE (PA)
MP,VISC,1,VISC     ! DYNAMIC VISCOSITY GAP
R,1,D_EL,,,PAMB    ! REAL CONSTANTS - GAP
RMORE,PREF,MFP
WIDTH = 29.02E-6
LENGTH = 92E-6

```

!!!!!! BUILD CANTILEVER MODEL !!!!!!!

```

K,1,0,0
K,2,WIDTH,0
K,3,WIDTH, LENGTH
K,4,0,LENGTH
A,1,2,3,4

```

```

TYPE, 1
MAT, 1
SMRTSIZE,4
AMESH, ALL           ! MESH THE MEMBRANE

```

```
*DO,G,0,1E6,1000
```

```

FREQ= G             ! FREQUENCY (HZ.)
OMEGA=2*PI*FREQ    ! FREQUENCY (RAD/SEC)

```

```

NSEL,ALL
NSEL,R,LOC,Y,0     ! SELECT ALL NODES ON THE ETCH CHANNEL

```

```
D,ALL,PRES,0      ! FIX PRESSURE AT OUTER PLATE BOUNDARY
```

```
DLIST,ALL
```

```
ALLSEL
```

```

BFE,ALL,FLUE,,VELO ! APPLY ARBITRARY VELOCITY
FINISH

```

```

FINISH
/SOLU
ANTYP,HARM         ! FULL HARMONIC ANALYSIS
HARFRQ,FREQ
SOLVE

```

```

FINISH
/POST1

ESEL,S,TYPE,,1
SET,1,1
ETABLE,PRESR,PRES      ! EXTRACT "REAL" PRESSURE
ETABLE,EAREA,VOLU
SMULT,FORR,PRESR,EAREA ! COMPUTE "REAL" FORCE
SSUM
*GET,FRE,SSUM,,ITEM,FORR
SET,1,1,,1
ETABLE,PRESI,PRES      !EXTRACT "IMAGINARY" PRESSURE
SMULT,FORI,PRESI,EAREA !COMPUTE "IMAGINARY" PRESSURE
SSUM
*GET,FIM,SSUM,,ITEM,FORI

K=ABS(FIM*OMEGA/VELO)!COMPUTE EQUIVALENT STIFFNESS
CB=ABS(FRE/VELO)      ! COMPUTE EQUIVALENT DAMPING

/COM,      *****      EQUIVALENT      STIFFNESS
*****
*STAT,K
/COM,      *****      EQUIVALENT      DAMPING
*****
*STAT,CB

*CFOPEN,FREQKBCANT,TXT,,APPEND
*VWRITE,FREQ,K,CB
%G %G %G
*CFCLOSE

*ENDDO

PLNSOL,PRES

FINISH

```

HARMONIC ANALYSIS (ANSYS)

FINISH
/CLEAR

/TITLE, DUAL CANTILEVER HARMONIC ANALYSIS
/PREP7

ET,1,SOLID95 ! DEFINE SOLID95 AS ELEMENT TYPE 1

MP,EX,1,110E9 ! NITRIDE MODULUS
MP,DENS,1,2200 ! NITRIDE DENSITY
MP,NUXY,1,.3 ! POISSON'S RATIO

!! ACTUATOR DIMENSIONS !!

T1 = 3E-6
W1 = 54E-6
L1 = 92E-6

!! SPACER DIMENSIONS !!

T2 = 4E-6 ! GAP BETWEEN SEN AND ACT
W2 = 21E-6 ! SAME AS WIDTH OF SENSOR
L2 = 1.6E-6 ! SAME AS SENSOR THICKNESS

!! SENSOR DIMENSIONS !!

T3 = L2
W3 = W2
L3 = L2 + 50E-6 ! LENGTH OF SENSOR

!! CENTER SENSOR W.R.T. ACTUATOR !!
!! BE AWARE THAT SMALLEST KP DISTANCE !!
!! IS LIMITED TO ~1 MICRON !!

O1 = L1 - L3
O2 = (W1-W2)/2

FORCE = -1E-6

!!!!!!!!!!!!!! CREATE ACTUATOR CANTILEVER !!!!!!!!!!!!!!!

BLOCK,0,W1,0,L1,0,-T1

!!!!!!!!!!!!!! CREATE SPACER !!!!!!!

BLOCK,O2,O2+W2,O1,O1+L2,-T1,T2+T3

!!!!!!!!!!!!!! CREATE SENSOR !!!!!!!

BLOCK,O2,O2+W3,O1,O1+L3,T2,T2+T3

!!!!!!! STITCH VOLUMES TOGETHER TO MAKE ONE SOLID STRUCTURE
!!!!!!!

VSEL,ALL
VOVLAP,ALL
VGLUE,ALL

MSHAPE,1,3D
VMESH,ALL

FINISH
/SOLU

ANTYPE,3
NSEL,S,P
F,ALL,FZ,FORCE

DA,3,ALL ! CONSTRAIN ALL DEGREES OF FREEDOM (LEFT - SIDE)
ALLSEL

HARFRQ,0,1000000,
NSUBST,500,
KBC,1

SOLVE
FINISH

/POST26

! SENSOR PATH
NSOL,2,1717,U,Z, UZ_1
NSOL,3,1731,U,Z, UZ_2
NSOL,4,1789,U,Z, UZ_3
NSOL,5,1825,U,Z, UZ_4
NSOL,6,1816,U,Z, UZ_5
NSOL,7,1821,U,Z, UZ_6
NSOL,8,1819,U,Z, UZ_7
NSOL,9,1781,U,Z, UZ_8

NSOL,10,1706,U,Z, UZ_9

! ACTUATOR PATH

NSOL,2,3248,U,Z, UZ_10

NSOL,3,7326,U,Z, UZ_11

NSOL,4,7423,U,Z, UZ_12

NSOL,5,7427,U,Z, UZ_13

NSOL,6,7527,U,Z, UZ_14

NSOL,7,7598,U,Z, UZ_15

NSOL,8,7657,U,Z, UZ_16

NSOL,9,7649,U,Z, UZ_17

NSOL,10,7584,U,Z, UZ_18

STORE,MERGE

plvar,9,10

REFERENCES

- [1] G. Binnig, C. F. Quate, and C. Gerber, "Atomic force microscope," *Mar*, vol. 3, pp. 930–933, 1986.
- [2] T. Ando, T. Uchihashi, N. Kodera, D. Yamamoto, A. Miyagi, M. Taniguchi, and H. Yamashita, "High-speed AFM and nano-visualization of biomolecular processes," *Pflügers Archiv European Journal of Physiology*, vol. 456, pp. 211–225, 2008.
- [3] P. K. Hansma, G. Schitter, G. E. Fantner, and C. Prater, "APPLIED PHYSICS: High-Speed Atomic Force Microscopy." vol. 314, 2006, pp. 601–602.
- [4] S. R. Manalis, S. C. Minne, A. Atalar, and C. F. Quate, "High-speed atomic force microscopy using an integrated actuator and optical lever detection," *Review of Scientific Instruments*, vol. 67, p. 3294, 1996.
- [5] Wikipedia, "Atomic force microscope --- Wikipedia, The Free Encyclopedia," 2009.
- [6] Agilent, "AFM Tip-Sample Interaction," 2009.
- [7] G. Schitter, F. Allgower, and A. Stemmer, "A new control strategy for high-speed atomic force microscopy," *Nanotechnology*, vol. 15, pp. 108–114, 2004.
- [8] T. Sulchek, G. G. Yaralioglu, C. F. Quate, and S. C. Minne, "Characterization and optimization of scan speed for tapping-mode atomic force microscopy," *Review of Scientific Instruments*, vol. 73, p. 2928, 2002.
- [9] H. Yamashita, N. Kodera, A. Miyagi, T. Uchihashi, D. Yamamoto, and T. Ando, "Tip-sample distance control using photothermal actuation of a small cantilever for high-speed atomic force microscopy," *Review of Scientific Instruments*, vol. 78, p. 083702, 2007.
- [10] G. R. Jayanth, Y. Jeong, and C. H. Menq, "Direct tip-position control using magnetic actuation for achieving fast scanning in tapping mode atomic force microscopy," *Review of Scientific Instruments*, vol. 77, p. 053704, 2006.
- [11] A. G. Onaran, M. Balantekin, W. Lee, W. L. Hughes, B. A. Buchine, R. O. Guldiken, Z. Parlak, C. F. Quate, and F. L. Degertekin, "A new atomic force microscope probe with force sensing integrated readout and active tip," *Review of Scientific Instruments*, vol. 77, p. 023501, 2006.
- [12] S. C. Minne, G. Yaralioglu, S. R. Manalis, J. D. Adams, J. Zesch, A. Atalar, and C. F. Quate, "Automated parallel high-speed atomic force microscopy," *Applied Physics Letters*, vol. 72, p. 2340, 1998.
- [13] N. Kodera, M. Sakashita, and T. Ando, "Dynamic proportional-integral-differential controller for high-speed atomic force microscopy," *Review of Scientific Instruments*, vol. 77, p. 083704, 2006.
- [14] G. E. Fantner, G. Schitter, J. H. Kindt, T. Ivanov, K. Ivanova, R. Patel, N. Holten-Andersen, J. Adams, P. J. Thurner, and I. W. Rangelow, "Components for high speed atomic force microscopy," *Ultramicroscopy*, vol. 106, pp. 881–887, 2006.
- [15] R. P. Manginell, D. R. Adkins, M. W. Moorman, R. Hadizadeh, D. Copic, D. A. Porter, J. M. Anderson, V. M. Hietala, J. R. Bryan, and D. R. Wheeler, "Mass-

- Sensitive Microfabricated Chemical Preconcentrator," *Microelectromechanical Systems, Journal of*, vol. 17, pp. 1396-1407, 2008.
- [16] E. Siegel, "ScienceBlogs," 2009.
- [17] B. Van Gorp, A. G. Onaran, and F. L. Degertekin, "Integrated dual grating method for extended range interferometric displacement detection in probe microscopy," *Applied Physics Letters*, vol. 91, p. 083101, 2007.
- [18] Z. Parlak, R. Hadizadeh, M. Balantekin, and L. Degertekin, "Real-time Topography and Mechanical Property Mapping of Soft Materials by FIRAT Using Active Tip Control," MRS Conference Presentation, 2009.
- [19] E. Sensors, "Equivalent-circuit model of the squeezed gas film in a silicon accelerometer," *Sensors and Actuators A*, vol. 48, pp. 239-248, 1995.
- [20] F. L. Degertekin, A. G. Onaran, M. Balantekin, W. Lee, N. A. Hall, and C. F. Quate, "Sensor for direct measurement of interaction forces in probe microscopy," *Applied Physics Letters*, vol. 87, p. 213109, 2005.
- [21] Wikipedia, "Helium–neon laser --- Wikipedia, The Free Encyclopedia," 2009.
- [22] S. Huang, I. K. Lin, H. Tao, and X. Zhang, "Development of Double-Cantilever Infrared Focal Plane Arrays: Fabrication and Post-Process Curvature Modification," 2007, p. 16.
- [23] S. D. Senturia, *Microsystem design*: Kluwer Academic Publishers, 2001.
- [24] A. Hrennikoff, "Solution of problems in elasticity by the framework method," *Journal of Applied Mechanics*, vol. 8, pp. 169-175, 1941.
- [25] D. McHenry, "A LATTICE ANALOGY FOR THE SOLUTION OF STRESS PROBLEMS," *JOURNAL OF THE ICE*, vol. 21, pp. 59-82, 1943.
- [26] G. Hähner, "Normal spring constants of cantilever plates for different load distributions and static deflection with applications to atomic force microscopy," *Journal of Applied Physics*, vol. 104, p. 084902, 2008.
- [27] ANSYS, "Release 11.0 Documentation for ANSYS," v10.8.0.7 ed: ANSYS Academic Teaching Advanced.
- [28] J. Kokavecz and A. Mechler, "Spring constant of microcantilevers in fundamental and higher eigenmodes," *Physical Review B*, vol. 78, p. 17, 2008.
- [29] C. P. Green, H. Lioe, J. P. Cleveland, R. Proksch, P. Mulvaney, and J. E. Sader, "Normal and torsional spring constants of atomic force microscope cantilevers," *Review of Scientific Instruments*, vol. 75, p. 1988, 2004.
- [30] A. H. Nayfeh and M. I. Younis, "A new approach to the modeling and simulation of flexible microstructures under the effect of squeeze-film damping," *Journal of Micromechanics and Microengineering*, vol. 14, pp. 170-181, 2004.
- [31] H. B. Callen and T. A. Welton, "Irreversibility and generalized noise," *Physica Phys Rev*, vol. 83, p. 34, 1939.
- [32] T. B. Gabrielson, U. Center, and P. A. Warminster, "Mechanical-thermal noise in micromachined acoustic and vibrationsensors," *IEEE transactions on Electron Devices*, vol. 40, pp. 903-909, 1993.
- [33] S. Pamidighantam, R. Puers, K. Baert, and H. A. C. Tilmans, "Pull-in voltage analysis of electrostatically actuated beam structures with fixed-fixed and fixed-free end conditions," *Journal of Micromechanics and Microengineering*, vol. 12, pp. 458-464, 2002.

- [34] S. Chowdhury, M. Ahmadi, and W. C. Miller, "A closed-form model for the pull-in voltage of electrostatically actuated cantilever beams," *Journal of Micromechanics and Microengineering*, vol. 15, pp. 756-763, 2005.
- [35] L. Meirovitch and R. G. Parker, "Fundamentals of vibrations," *Applied Mechanics Reviews*, vol. 54, p. B100, 2001.
- [36] W. C. Hurty, "Vibrations of structural systems by component-mode synthesis," *Journal of the Engineering Mechanics Division, ASCE*, vol. 86, pp. 51-69, 1960.
- [37] J. H. Ginsberg and W. E. Seemann, "Mechanical and Structural Vibration: Theory and Applications," *Applied Mechanics Reviews*, vol. 54, p. B60, 2001.
- [38] S. M. Kim and B. F. McCullough, "Dynamic response of plate on viscous Winkler foundation to moving loads of varying amplitude," *Engineering Structures*, vol. 25, pp. 1179-1188, 2003.
- [39] M. H. Huang, "Dynamic response of plates on elastic foundation to moving loads," *Journal of Engineering Mechanics*, vol. 128, p. 1016, 2002.
- [40] C. Chang, Y. F. Wang, Y. Kanamori, J. J. Shih, Y. Kawai, C. K. Lee, K. C. Wu, and M. Esashi, "Etching submicrometer trenches by using the Bosch process and its application to the fabrication of antireflection structures," *Journal of Micromechanics and Microengineering*, vol. 15, pp. 580-585, 2005.